

© 2019

Jill Irene Tracey

ALL RIGHTS RESERVED

PHOTONIC AND PLASMONIC PROPERTIES OF SILVER
NANOPARTICLE/CONJUGATED POLYMER ULTRA-THIN-FILM COMPOSITES

by

JILL IRENE TRACEY

A dissertation submitted to the

School of Graduate Studies

Rutgers, The State University of New Jersey

In partial fulfillment of the requirements

For the degree of

Doctor of Philosophy

Graduate Program in Department of Chemistry and Chemical Biology

Written under the direction of

Deirdre M. O'Carroll

And approved by

New Brunswick, New Jersey

October, 2019

ABSTRACT OF THE DISSERTATION

Photonic and Plasmonic Properties of Silver Nanoparticle/Conjugated Polymer Ultra-

Thin-Film Composites

By JILL IRENE TRACEY

Dissertation Director:

Deirdre M. O'Carroll

Plasmonics is a rapidly growing field of optics that utilizes plasmon resonances, which arise from collective oscillations of the free electrons in metallic nanostructures. Plasmonic nanomaterials have been incorporated into optoelectronic devices, spectroscopic methods, and nanophotonic applications to enhance the emission or absorption of light, with the aim of improving efficiency. By utilizing plasmons instead of light, traditional optical devices, such as lasers, can become nanoscale in physical size; however, demonstrations of plasmon-enhanced light emission at blue wavelengths are not common. The main reasons are the increase in interband electronic absorption (i.e., loss) that occurs in plasmonic materials at short wavelengths and the challenge of finding materials or materials combinations that can overcome these losses.

Traditional optics rely on light, which is diffraction limited, meaning there is a limit to how small of a volume the light can be confined due to the bending of light in or around small objects. By utilizing plasmonics, light can be manipulated below this diffraction limit, allowing for thinner films and devices. There are practical reasons for desiring thinner films (e.g. lower costs for production); but there are also interesting

phenomena that occur in thin films that do not necessarily translate to bulk films. For example, due to differences in the refractive index of the layers (e.g. the film and air) light tends to be reflected and transmitted differently in thin-films (due to pronounced interference) compared to how light interacts with bulk films. Working with dimensions below the diffraction limit of light allows for the observation of new phenomena which have previously been unexplored such as local interactions between nanoparticles and light-emitting materials.

In this thesis, two topics of plasmonics are investigated, metal-molecule interactions, and metal-nanoparticle synthesis. To investigate metal-molecule interactions, the combination of plasmonic silver nanoparticles with light-emitting conjugated polymer materials is studied in two different systems. The use of solution-processable conjugated polymers allows for easy fabrication of thin-films; providing controllability of the thickness of the light-emitting material used below the diffraction limit of light. This enables local interactions between silver nanoparticles and the light-emitting thin-films to be studied in ultra-thin layers in ensemble measurements as well as at the single particle level.

In the first part of the thesis, thin-film composites of silver nanoparticles and an organic conjugated polymer (poly(9,9-di-n-octylfluorenyl-2,7-diyl); PFO) are investigated for their ability to behave as spasers (surface plasmon amplification by stimulated emission of radiation). This combination of materials is chosen so that there is good spectral overlap of the localized surface plasmon resonance of the silver nanoparticles and the high-gain emission peak of PFO. The composite films demonstrate stimulated emission of surface plasmons when ultra-thin-films of PFO are employed,

ranging from 30 nm - 70 nm in thickness. Additionally, the quality factor of the spaser is enhanced in some instances, which is attributed to occurrences of interparticle coupling. These spasers emit at a wavelengths between 444.8 nm and 449.4 nm, which is the first demonstration of blue-emitting spasers.

Next, ultra-thin-film composites of silver nanoparticles and a different organic conjugated polymer, (poly(9,9-di-n-octylfluorenyl-2,7-diyl)-alt-(benzo[2,1,3] thiadiazol-4,8-dily); (F8BT)), are investigated. The F8BT film thickness is between ~ 3.75 nm – 5 nm. In this particular composite, there is good spectral overlap of the localized surface plasmon resonance of the silver nanoparticle and the absorption band of F8BT. The occurrence of plasmon-exciton coupling and the extent of enhancement of the polymer's emission is investigated in this system. It is demonstrated that enhanced emission occurs at the single nanoparticle level. Additionally, absorption induced scattering, which is a form of plasmon-exciton coupling, is clearly identified in this system. The study of optical and photonic interactions between silver nanoparticles and conjugated polymer thin-films enable advancements in demonstrations and potential applications of plasmonic materials at shorter wavelengths and at smaller size scales.

In the metal-molecule investigations spherical silver nanoparticles are used, due to their blue localized surface plasmon resonance wavelength, which overlaps well with the conjugated polymers studied. However, utilizing nanorod-shaped nanoparticles, that have two localized surface plasmon resonance wavelengths (one corresponding to the width and one corresponding to the length) would allow for tunability of the molecules utilized in metal-molecule interactions and, potentially, stronger plasmon-exciton coupling. However, nanorod shaped silver nanoparticles are not commercially available;

therefore, they need to be synthesized in the laboratory. In the last part of this thesis, the polyol synthesis method for anisotropic silver nanoparticles is investigated, in order to better understand the challenges associated with their synthesis, which is one reason that silver is not utilized as often for plasmonic applications. Parameters such as polyol solvent molecular weight, reaction time, reaction temperature, and ratio of reagents are investigated extensively. The synthesis of silver nanoparticles is found to be very sensitive to the molecular weight of the polyol solvent, and the size and shape of the silver nanoparticles are restricted to low aspect ratios for higher molecular weight polyols.

Acknowledgements

I would like to first acknowledge my family, for instilling in me the importance of an education, and for supporting and encouraging me in everything that I pursue.

I would also like to acknowledge my colleagues who have provided immeasurable assistance throughout my Ph.D. study. My group members Cindy Kumah, Hemanth Maddali, Kelsey Gwynne, Nasir Javed, Krystal House, Binxing Yu, Christopher Petoukhoff, Catrice Carter, Zeqing Shen, and Ankur Dalsania for their assistance with lab equipment, feedback, discussions and collaborations. I would like to specifically acknowledge Zhongkai Cheng, who assisted with the silver nanoparticle synthesis research when I had the pleasure of mentoring him as an undergraduate student. Zhongkai later joined our research group as a graduate student, and assisted me with the plasmon-exciton work with fabrication of dewetted silver nanoparticle surfaces. Sarah Goodman, whose senior thesis project on core-shell spasers was the inspiration for my investigations into spasers, and Seerat Aziz, another undergraduate I had the privilege to mentor. Without Seerat's dedication we would not have been able to analyze as many variables in the polyol synthesis as we did. Priyanka Dilip, Jessica Kuleshov, Kian Vilhauer, and Christopher Yoo, all of whom were students in the NJ-GSET program for their assistance with performing a life cycle analysis on the silver nanoparticle synthesis.

I would like to acknowledge the RiSE at Rutgers Program, which is an undergraduate summer research experience. Specifically, I would like to thank Dean Evelyn Erenrich for her support, encouragement, and kindness, as well as Prof. Bozena Michniak and Krizia M. Karry, who were my mentors that summer during the program. I was selected for this program in 2013, and it truly changed the direction I would take in

life. Attending the RiSE REU program encouraged me to pursue further education. I truly believe that without being given the opportunity to experience the research at a major university, I would not have pursued studying for a Ph.D.

I would also like to acknowledge Prof. Gene Hall and Prof. Geeta Govindarajoo, two professors who I had the privilege to be a teaching assistant for. I learned so much from both of them, including classroom management, leadership, pedagogy, organization, and laboratory techniques. I am extremely grateful for the time and effort that they put into their courses, and the mentorship that they have provided me.

I would like to acknowledge my thesis committee members, Prof. Laura Fabris, Prof. Tewodros (Teddy) Asefa, and Prof. Stefan Strauf, for their time and willingness to serve on my committee. I am grateful for all of the constructive suggestions and comments Prof. Fabris and Prof. Asefa provided during my thesis proposal defense and yearly-update meetings. I would like to thank Prof. Strauf for his willingness to take the time to come to Rutgers from Stevens Institute for my dissertation defense.

Last but not least, I am tremendously indebted to my thesis advisor, and mentor, Prof. Deirdre M. O'Carroll for all of her support, encouragement, and assistance throughout my time at Rutgers. Her constant encouragement has led me to undertake projects which I never thought would be possible, and to step out of my comfort zone. I am grateful for her encouragement to present at conferences which led to insights and breakthroughs in my research projects. I am very appreciative of the opportunities she provided me to mentor undergraduate students, and her encouragement to pursue extracurricular opportunities, such as when I spent a summer teaching in Mississippi with the Freedom Summer Collegiate program. Through her diligently demonstrating how to

be a rigorous researcher and gently teaching how to be a mentor, I have become a better scientist and a better person

Chapter 2 of this dissertation was based upon a first author publication written by J.I. Tracey (publication 1 from the List of Publications). Chapter 3 is based upon unpublished work led by the author (publication 3 from the List of Publications). A manuscript written by the author based upon Chapter 3 will be submitted for publication imminently. Chapter 4 is based upon a first author manuscript (publication 2 from the List of Publications), written by the author that has been submitted for publication.

Table of Contents

ABSTRACT OF THE DISSERTATION.....	ii
Acknowledgments.....	vi
List of Tables.....	xiii
List of Figures.....	xiv
List of Abbreviations.....	xxii
List of Publications.....	xxiii
List of Presentations.....	xxiv
Chapter 1. Background and Scope of Investigation.....	1
1.1 Plasmonics: Utilization of Surface Plasmons.....	3
<i>1.1.1 Gain to Overcome Loss.....</i>	<i>6</i>
<i>1.1.2 Metals That Support Plasmonic Resonances.....</i>	<i>8</i>
<i>1.1.2.1 Plasmonic Properties of Silver.....</i>	<i>9</i>
1.2 Metal-Molecule Interactions.....	11
<i>1.2.1 Plasmon-Exciton Coupling.....</i>	<i>11</i>
<i>1.2.2 Organic Semiconducting Conjugated Polymers.....</i>	<i>12</i>
1.3 Types of Nanoscale Plasmonic Lasers.....	12
<i>1.3.1 Metal-Film Plasmonic Nanolasers.....</i>	<i>17</i>
<i>1.3.2 Metal-Nanoparticle Random Lasers.....</i>	<i>17</i>
<i>1.3.3 Metal-Nanoparticle Lasing-Spasers.....</i>	<i>18</i>
1.4 Properties of Nanoscale Plasmonic Lasers.....	19
<i>1.4.1 Threshold.....</i>	<i>19</i>
<i>1.4.2 Spectral Region.....</i>	<i>20</i>

1.5 Synthesis of Silver Nanoparticles	20
1.6 Thesis Overview and Scope of this Thesis	22
Chapter 2. Short-Wavelength Lasing-Spasing and Random Spasing with Deeply-Subwavelength Thin-Film Gain Media	24
2.1 Abstract	25
2.2 Introduction	26
2.3 Results and Discussion	28
2.4 Conclusions	43
2.5 Methods	44
<i>2.5.1 Materials</i>	44
<i>2.5.2 Methods and Instrumentation</i>	45
<i>2.5.3 Trend Line Fitting</i>	48
Chapter 3. Investigations into Plasmon-Exciton Coupling in Silver Nanoparticle/Conjugated Polymer Thin-Films	50
3.1 Abstract	51
3.2 Introduction	51
3.3 Results and Discussion	53
<i>3.3.1 Dense Silver Nanoparticle Films</i>	53
<i>3.3.2 Single Nanoparticle Studies</i>	57
3.4 Conclusions	64
3.5 Methods	65
<i>3.5.1 Materials</i>	65
<i>3.5.2 Methods and Instrumentation</i>	66

3.5.3 Spectral Corrections.....	68
Chapter 4. The Role of Polyol Molecular Weight in the One-Pot Polyol Synthesis of Silver Nanoparticles.....	69
4.1 Abstract.....	70
4.2 Introduction	70
4.3 Results and Discussion.....	73
4.3.1 Effect of Solvent.....	75
4.3.2 Solvent: Ethylene Glycol.....	80
4.3.3 Solvent: Poly(Ethylene Glycol) 300.....	83
4.3.4 Mixed Solvents Ethylene Glycol and Poly(Ethylene Glycol) 200..	90
4.4 Conclusions.....	92
4.5 Materials and Methods.....	94
4.5.1 Materials.....	94
4.5.2 Methods.....	95
4.5.3 Modifications to the Synthesis Procedure.....	96
4.5.3.1 PEG 300 Heating in Stages Procedure.....	96
4.5.3.2 PEG 300 Increased Molar Ratio of PVP:AgNO ₃ Procedure.....	97
4.5.3.3 PEG 300 with FeCl ₃ Source Procedure.....	98
4.5.3.4 50:50 EG:PEG 200 Ratio Procedure.....	99
Chapter 5. Summary, Conclusions, and Future Directions.....	101
5.1 Summary and Conclusions.....	102
5.2 Future Directions.....	106

5.2.1	<i>Coherence and Polarization/Angle Dependence of Spasers</i>	106
5.2.2	<i>Polyol Synthesis</i>	107
5.2.3	<i>Life Cycle Assessment</i>	108
5.2.4	<i>Alternative Exciton Sources</i>	108
5.2.4	<i>Single Particle Spasers</i>	109
Appendix		110
A.1 Appendix to Chapter 2		110
A.1.1	<i>Dependence of Stimulated Emission Spectra on the Region of the Sample Probed and on Emission Area Collected</i>	112
A.2 Appendix to Chapter 3		116
A.3 Appendix to Chapter 4		126
A.3.1	<i>90:10 EG:PEG 200 Ratio Procedure</i>	127
A.4 Appendix to Chapter 5		129
A.4.1	<i>Life Cycle Assessment of Polyol and Sodium Borohydride Methods</i>	129
A.4.2	<i>Single Particle Spasers</i>	132
Bibliography		134

List of Tables

p. 6.....Table 1.1 Estimated gain required for various plasmonic nanoparticles for stimulated emission of surface plasmons as reported by various groups (references included in brackets).

p. 7.....Table 1.2 Examples of gain materials of interest for lasing-spasers, random lasers, or plasmonic nanolasers along with maximum gain coefficients and processing details.

p. 13-16.....Table 1.3 Summary of Current Demonstrations of Spasers, Plasmonic Nanolasers, and Random Lasers

p. 74.....Table 4.1. Summary of the reaction conditions for the various Ag nanostructure trials.

p. 79.....Table 4.2. Summary of the yield of syntheses using different solvents.

p. 90.....Table 4.3. Summary of the yield of syntheses using PEG 300 without heat.

p. 131.....Table A4.1.1. Reagents and their role for each method analyzed.

List of Figure Captions

p. 5.....Figure 1.1. Theoretical predictions of the extinction spectra for various AgNPs and experimental extinction spectra for various sizes of AgNPs. (a) Theoretical predictions of the LSPR for varying AR of AgNPs in different refractive indices of the environment. (top) AgNPs in a refractive index, n , of 1 (air). (bottom) AgNPs in n of 1.7 (polymer). (b) Theoretical and measured extinction spectra for the LSPR for spherical AgNPs. (top) Theoretical LSPR predicted for spherical AgNPs with different n of the environment. (bottom) Experimental LSPR for spherical nanoparticles on poly(acrylic acid) (PAA) coated glass, of varying NP diameter.

p. 10.....Figure 1.2. Measured PL spectra compared to theoretical predictions for the SPR of AgNPs. (top) The emission of a PFO thin-film (black line) and F8BT thin-film (red line) each were spin coated on a glass substrate. (bottom) The calculated extinction spectra for AgNPs of AR = 1 (spherical NP; black line), and AR = 1.5 (anisotropic NR; red line), each calculation is with a refractive index, n , of 1.7, corresponding to a polymer.

p. 30.....Figure 2.1. Configuration of the samples for lasing-spasers and spectra of constituent materials. (a) Schematic of glass/optical adhesive/PFO/AgNPs/PAA/glass samples showing excitation and PL emission directions. A 355 nm pulsed laser excites the sample from the AgNPs/PAA/glass side of the sample. PL emission is collected from the PFO side of the sample. (b) Normalized, UV-visible extinction spectra and normalized PL emission spectrum for component materials of the lasing-spasers: extinction of PFO/60 nm AgNPs/PAA (black); extinction of PFO (red); PFO PL emission spectrum (blue). (c) UV-visible extinction spectra for different NP constituents: extinction of 40 nm AgNPs/PAA (pink); extinction of 60 nm AgNPs/PAA (green); extinction of 60 nm AuNPs/PAA (purple).

p. 32.....Figure 2.2. Microscopy images with schematics to represent the sample that was imaged. (a) Representative SEM image of an AgNPs/PAA/silicon sample with AgNP density of 24 ± 3 NPs/ μm^2 . Inset in (a) is a DF optical image of the AgNP/PAA/silicon sample. (b) DF optical image of a PFO/AgNPs/PAA/glass sample. (c) PL image of a PFO/AgNPs/PAA/glass sample. The AgNP density is estimated for (b, c) to be ~ 25 NPs/ μm^2 . (d) Representative SEM image of a 60 nm AuNPs/PAA/silicon sample with AuNP density of 18 ± 2 NPs/ μm^2 . Inset in (d) is a DF optical image of the 60 nm AuNP/PAA/silicon sample. (e) DF optical image of a PFO/60 nm AuNPs/PAA/glass sample. Inset in (b, e) is a DF image of PFO/glass. (f) PL image of a PFO/60 nm AuNPs/PAA/glass sample. To remove some of the background, in (c and f) a PL image of the PFO/glass sample was subtracted from the PFO/NPs/PAA/glass samples using Image J. Insets of (c and f) are magnified regions of the PL images from (c and f) to show detail. The AuNP density is estimated for (e, f) to be ~ 20 NPs/ μm^2 . t_{PFO} for (b, c, e, f) and the associated insets was 70 ± 8 nm. Scale bars for the SEM images are 500 nm. All other scale bars are 20 μm .

p. 33.....Figure 2.3. PL emission spectra of PFO/AuNPs, PFO/AgNPs, and neat PFO samples. (a) Averaged excitation-energy-density-dependent PL emission spectra from five different regions of one PFO/AuNPs samples with density of AuNPs of ~ 20 NPs/ μm^2 . (b) Averaged excitation-energy-density-dependent PL emission spectra from four different regions of one PFO/AgNPs sample with density of AgNPs of ~ 25 NPs/ μm^2 ; inset in (b) averaged excitation-energy-density-dependent PL emission spectra from four different regions of one neat PFO film (i.e., no NPs). For all of these samples $t_{PFO} = 70 \pm 8$ nm.

p. 36.....Figure 2.4. PL emission spectra of PFO/AgNP and neat PFO samples with varying t_{PFO} as a function of E_{ex} . Main panel: Excitation power-dependent PL emission spectra for PFO films of varying thicknesses with an AgNP density of 24 ± 3 NPs/ μm^2 (i.e., glass/optical adhesive/PFO/AgNPs/PAA/glass). Inset: Excitation power-dependent PL emission spectra for neat PFO films of varying thicknesses (i.e., glass/epoxy/PFO/glass). (a) 70 nm PFO, (b) 58 nm PFO, (c) 47 nm PFO, (d) 40 nm PFO, (e) 30 nm, (f) 25 nm PFO. Repetition rate was from 104-205 Hz. Each spectrum was averaged from three different regions of one sample.

p. 38.....Figure 2.5. Peak 0-1/0-0 emission intensity ratio as a function of E_{ex} and t_{PFO} and $\Delta\lambda$ as a function of E_{ex} and t_{PFO} . (a) Plot of the ratio of the 0-1 emission peak to the 0-0 emission peak of PFO (i.e., 0-1/0-0 emission intensity ration) for PFO/AgNPs (red circles) and neat PFO (black inverted triangles) samples verses E_{ex} for various t_{PFO} . A piecewise linear function with two linear segments was fit to the data (solid red and black lines). (b) Plot of $\Delta\lambda$ (quantified using the spectral FWHM) of emission spectra from PFO/AgNP (red circles) and neat PFO (black inverted triangles) samples verses E_{ex} for various t_{PFO} . A piecewise linear function with three linear segments was fit to the data (solid red and black lines). For both (a and b) the panels are of samples with nominal t_{PFO} of 25 nm, 30 nm, 40 nm, 47 nm, 58 nm, and 70 nm from top to bottom, respectively. AgNP density was ~ 25 NPs/ μm^2 for all samples. Repetition rate was from 104-205 Hz.

p. 39.....Figure 2.6. Trend of λ_{em} versus t_{PFO} and E_{th} versus t_{PFO} . Top panel: 0-1 peak λ_{em} , below E_{th} (black squares), and above E_{th} (red inverted triangles) for PFO/AgNPs samples versus t_{PFO} . Middle panel: 0-0 peak λ_{em} for PFO/AgNPs samples versus t_{PFO} . For both, the λ_{em} was averaged for at least ten different spectra, at different regions of the sample, leading to potentially different AgNP local densities that cause the larger error in the data, at a range of excitation energies, for each t_{PFO} . Bottom panel: E_{ex} at which there was an onset of stimulated emission (i.e., E_{th}) for PFO/AgNPs samples versus t_{PFO} . E_{th} was averaged from three or more different regions from a sample with the specified t_{PFO} . A linear trend line was fit to the data for each panel.

p. 41.....Figure 2.7. Examples of spectrally-narrow, multimode, stimulated emission. (a) and (b): Excitation-energy-density-dependent PL emission spectra from one region of one PFO/AgNPs sample with $t_{PFO} \cong 47$ nm showing (a) multimode stimulated emission and pronounced spectral narrowing, and (b) broader single-mode stimulated emission. (c) Multimode stimulated emission from one region of one PFO/AgNPs sample with $t_{PFO} \cong 30$ nm. The density of AgNPs was ~ 25 NPs/ μm^2 for each sample.

p. 54.....Figure 3.1 (a) Normalized UV-visible extinction spectra and normalized PL emission spectrum for component materials: extinction of F8BT (black); extinction of 60 nm AgNPs (red); F8BT PL emission (blue); extinction of AgDW sample (pink). (b) Schematic of DF microscopy setup, indicating the configuration of the sample. (c-f) DF microscope images of Ag nanostructures on glass; (c) uncoated AgNPs; (d) uncoated AgDW; (e) the same AgNPs shown in (c) coated with F8BT; (f) AgDW coated with F8BT (not the same particles shown in (d)). Scale bars are 50 μm for all DF images. (g) SEM image of F8BT coated 60 nm AgNPs. (h) SEM image of uncoated AgDW sample. Scale bars for the SEM images are 500 nm.

p. 56.....Figure 3.2. DF scattering spectra from AgDW samples and controls. (a) DF scattering spectra of four different regions of uncoated AgDW samples. (b) DF scattering spectra of three different regions of planar F8BT samples. (c) DF scattering spectra for four different regions of F8BT coated AgDW samples. (d) DF scattering spectra of F8BT coated AgDWs divided by the spectra of F8BT from a planar F8BT sample (dashed lines), compared to the F8BT extinction spectra (red).

p. 59.....Figure 3.3. DF scattering spectra obtained from single AgNPs and single AgNPs coated with ultra-thin F8BT films. The AgNPs were supported by a glass substrate. (a,b) Averaged DF scattering spectra of five different single AgNPs; (a) before coating with F8BT; (b) after coating with F8BT. (c,d) DF image spectra of two of the AgNPs from (a and b); (c) uncoated AgNPs; (d) F8BT coated AgNPs. (e, f) DF image spectra of the AgNPs with the spectrum of a nearby region where no AgNP was present subtracted from the entire image spectra; (e) uncoated AgNPs; (f) F8BT coated AgNPs.

p. 62.....Figure 3.4. DF division spectra. First, each spectrum in the image spectra was divided by a spectrum of a nearby region of the sample, where no AgNP was present. Six spectra from the maximum emission from the AgNP were then averaged. (a,c,e) are the division spectra for the uncoated AgNPs from various regions of the sample. (b,d,f) are the division spectra for the same AgNPs after being coated with an ultra-thin F8BT film. Inset is a schematic demonstrating the enhancement that occurs due to the plasmon-exciton coupling; uncoated AgNPs only scatter at their LSPR, but when coupled, the emission wavelength shifts, as well as is enhanced, with a more intense, blue-green emission detected.

p. 64.....Figure 3.5. Averaged DF scattering spectra from F8BT coated AgNPs divided by the spectra of F8BT from a nearby region, compared to the F8BT extinction spectra (red line) and compared to the refractive index of F8BT (green line). (a) Spectra obtained from region A of the sample, AgNP number 1. (b) Spectra obtained from region B of the sample, AgNP number 2. (c-d) Spectra obtained from region C of the sample, 2 different AgNPs.

p. 77.....Figure 4.1. SEM images and photographs of the reaction product for each reaction with chemical structures of the solvent underneath. (a and e) Reaction using EG as the solvent. (b and f) Reaction using PEG 200 as the solvent. (c and g) Reaction using PEG 300 as the solvent. (d and h) Reaction using PEG 600 as the solvent. Insets of (a, b, c, and d) are magnified images of the reaction product. (i) UV-visible extinction spectra for the reaction products shown in (e-h); black line is EG, red line is PEG 200, blue line is PEG 300, and pink line is PEG 600. Scale bars: (a) is 10 μm ; (a inset and c) are 1 μm ; (b and d) are 500 nm; and (b inset, c inset, and d inset) are 200 nm.

p. 82.....Figure 4.2. SEM images and reaction photographs of the reaction products for EG syntheses with one variable changed at a time with chemical structure of the solvent underneath. (a and e) EG synthesis that was purified immediately after the reagents were added. (b and f) EG synthesis without a source of chloride ions added. (c and g) EG synthesis with a PVP weight percent increased by a factor of three. (d and h) EG synthesis with a PVP weight percent increased by a factor of six. Insets of (a-d) are magnified images of the reaction products. Scale bars: (a, b, and c inset) are 1 μm ; (c) is 3 μm ; and (d, a inset, b inset, c inset, and d inset) is 500 nm.

p. 85.....Figure 4.3. SEM images and photographs of the reaction products for PEG 300 syntheses with multiple variables altered between syntheses. (a and e) Heated in stages from 50 $^{\circ}\text{C}$ to 100 $^{\circ}\text{C}$ (0.1087 g PVP in 5 mL PEG 300, 0.0096 g AgNO_3 in 50 μL H_2O) reaction time 8 hr. (b and f) $\sim 3:1$ PVP: AgNO_3 ratio (0.3169 g PVP in 1 mL PEG 300, 0.1024 g AgNO_3 in 1 mL H_2O) heated at 90 $^{\circ}\text{C}$ for 7 h. (c and g) $\sim 6:1$ PVP: AgNO_3 ratio (0.6170 g PVP in 1 mL PEG 300, 0.1021 g AgNO_3 in 1 mL H_2O) heated at 90 $^{\circ}\text{C}$ for 7 h. (d and h) With chloride ions (6×10^{-4} M $\text{FeCl}_3 \cdot 6 \text{H}_2\text{O}$, 0.16 g of AgNO_3 and 0.07 g of PVP dissolved in 10 mL of PEG 300) heated at 150 $^{\circ}\text{C}$ for 2 h. Insets of (a-d) are magnified images of the reaction products. (i) UV-visible extinction spectra for the purified products shown in (a-d), with chemical structure of the solvent used; the black line is from the synthesis that was heated in stages, the red line is from a synthesis with the PVP weight percent of 0.41 M (3x increase), and the blue line is the PVP weight percent of 0.79 M (6x increase). Scale bars: (a, a inset, c inset, and d inset) is 100 nm; (b inset, c, and d) is 200 nm; and (b) is 500 nm.

p. 88.....Figure 4.4. SEM images and photographs of the reaction products for PEG 300 syntheses carried out at room temperature, at certain times in the reaction; (a and d) after 5 minutes; (b and e) after 10 minutes; (c and f) after 20 minutes. Insets of (a, b, and c) are magnified images of the reaction products. Scale bars for (a) is 500 nm; (b, c, and a inset) are 200 nm; and (b inset and c inset) are 100 nm. The chemical structure of the solvent is included underneath the reaction photographs.

p. 91.....Figure 4.5. SEM images and photographs for the reaction product; (a, b) EG only reaction; (c, d) 50:50 EG:PEG 200 ratio reaction, with an inset of a magnified region. Scale bars for all SEM images are 1 μm .

p. 94.....Figure 4.6. Schematic diagram summarizing synthesis setup, variables, and the corresponding silver nanoparticle products. Silver nitrate and polyvinylpyrrolidone were first dissolved in the polyol solvent, either EG, PEG 200, PEG 300, or PEG 600, and added dropwise to the flask from a burette, that contained the same polyol solvent as well as a source of chloride ions, in the form of iron chloride. The reaction was stirred the entire time. By varying the solvent the reaction product can be varied as shown by the arrows leading to the predominant reaction products for each solvent.

p. 110.....Figure A1.1. Optical images of AgNP density as well as coverage of PFO polymer film. (a-c) DF image of AgNPs with varying PFO film thicknesses of 50 nm, 47 nm and 30 nm, respectively. Insets are of neat PFO films with the corresponding thicknesses. (d-f) PL images, illuminated by a continuous-wave 405 nm laser diode, of AgNPs with varying PFO film thicknesses of 50 nm, 47 nm and 30 nm, respectively. Insets are of neat PFO films with the corresponding thickness. Scale bars are 10 μm .

p. 110.....Figure A1.2. PL spectrum of glass/optical adhesive/glass compared to glass/optical adhesive/AgNPs/PAA/glass spectrum, as well as glass/optical adhesive/PFO/glass spectrum.

p. 111.....Figure A1.3. Trend of λ_{em} (0-2) versus t_{PFO} . 0-2 peak λ_{em} for PFO/AgNPs samples versus t_{PFO} , the λ_{em} was averaged for at least ten different spectra, at different regions of the sample, leading to potentially different AgNP local densities which cause the larger error in the data, and at a range of excitation energies, for each t_{PFO} . A linear trendline was fit to the data. Repetition rate ranged from 104-205 Hz.

p. 112.....Figure A1.4. Variations observed in PL emission spectra for samples of varying PFO thickness and with an AgNP density of 24 ± 3 NPs/ μm^2 (i.e., glass/epoxy/PFO/AgNPs/PAA/glass). (a) 58 nm PFO (b) 50 nm PFO (c) 40 nm PFO (d) 30 nm PFO.

p. 114.....Figure A1.5. Emission spot dependence of PL spectra. (a) Defocused emission spot on imaging spectrometer, slit in the center of the emission spot, sample probed near the center. (b) Defocused emission spot on imaging spectrometer, slit in the center of the emission spot, sample probed near the edge. (c) Defocused emission spot on imaging spectrometer, slit in the edge of the emission spot, sample probed near the center. (d) Finely-focused emission spot on imaging spectrometer, slit in the center of the emission spot, sample probed near the center. Note that for all PL spectra, the actual laser excitation spot size and, correspondingly, the expected PL emission spot size at the sample was fixed at ~ 0.28 mm in diameter.

p. 115.....Figure A1.6. Diagram of PL spectroscopy setup.

p. 116.....Figure A2.1. Images taken of region A of the AgNP sample before and after coating with an ultra-thin layer of F8BT. (a-b) DF microscope images of AgNPs before coating (a) and after coating (b) with F8BT. (c-f) Real-space spectrometer images of AgNPs before coating (c, d) and after coating (e, f) with F8BT. (d-e) are when the spectrometer slit was closed, in order to isolate individual AgNPs. The designations of the AgNP positions are indicated between images d and e. (g-h) Spectrometer image spectra obtained for the AgNPs before coating (g) and after coating (h) with F8BT.

p. 117.....Figure A2.2. Images taken of region B of the AgNP sample before and after coating with an ultra-thin layer of F8BT. (a-b) DF microscope images of AgNPs before coating (a) and after coating (b) with F8BT. (c-f) Real-space spectrometer images of AgNPs before coating (c, d) and after coating (e, f) with F8BT. (d-e) are when the spectrometer slit was closed, in order to isolate individual AgNPs. The designations of the AgNP positions are indicated between images d and e. (g-h) Spectrometer image spectra obtained for the AgNPs before coating (g) and after coating (h) with F8BT.

p. 118.....Figure A2.3. Images taken of region C of the AgNP sample before and after coating with an ultra-thin layer of F8BT. (a-b) DF microscope images of AgNPs before coating (a) and after coating (b) with F8BT. (c-f) Real-space spectrometer images of AgNPs before coating (c, d) and after coating (e, f) with F8BT. (d-e) are when the spectrometer slit was closed, in order to isolate individual AgNPs. The designations of the AgNP positions are indicated between images d and e. (g-h) Spectrometer image spectra obtained for the AgNPs before coating (g) and after coating (h) with F8BT.

p. 119.....Figure A2.4. DF scattering spectra obtained from single AgNPs and single AgNPs coated with ultra-thin F8BT films corresponding to region A of the sample. (a) DF image spectra of the uncoated AgNPs. (b) DF image spectra of the F8BT coated AgNPs corresponding to particles from (a). (c) DF image spectra of the uncoated AgNPs. (d) DF image spectra of the F8BT coated AgNPs corresponding to particles from (c).

p. 120.....Figure A2.5. DF scattering spectra obtained from single AgNPs and single AgNPs coated with ultra-thin F8BT films corresponding to region B of the sample. (a) averaged DF scattering spectra of single AgNPs before coating. (b) Averaged DF scattering spectra of the same single AgNPs after coating with F8BT. (c) DF image spectra of the uncoated AgNPs. (d) DF image spectra of the F8BT coated AgNPs corresponding to particles from (c). (e) DF image spectra of the uncoated AgNPs (f) DF image spectra of the F8BT coated AgNPs corresponding to particles from (e).

p. 121.....Figure A2.6. DF scattering spectra obtained from single AgNPs and single AgNPs coated with ultra-thin F8BT films corresponding to region C of the sample. (a) averaged DF scattering spectra of single AgNPs before coating. (b) Averaged DF scattering spectra of the same single AgNPs after coating with F8BT. (c) DF image spectra of the uncoated AgNPs. (d) DF image spectra of the F8BT coated AgNPs corresponding to particles from (c). (e) DF image spectra of the uncoated AgNPs (f) DF image spectra of the F8BT coated AgNPs corresponding to particles from (e).

p. 122.....Figure A2.7. DF scattering spectra obtained from single AgNPs and single AgNPs coated with ultra-thin F8BT films corresponding to region A of the sample. (a, c) DF image spectra of the uncoated AgNPs, with the spectrum of a nearby area without a NP subtracted from all the spectra. (b, d) DF image spectra of the F8BT coated AgNPs, with the spectrum of a nearby area without a NP subtracted from all the spectra.

p. 123.....Figure A2.8. DF scattering spectra obtained from single AgNPs and single AgNPs coated with ultra-thin F8BT films corresponding to region B of the sample. (a, c) DF image spectra of the uncoated AgNPs, with the spectrum of a nearby area without a NP subtracted from all the spectra. (b, d) DF image spectra of the F8BT coated AgNPs, with the spectrum of a nearby area without a NP subtracted from all the spectra.

p. 124.....Figure A2.9. DF scattering spectra obtained from single AgNPs and single AgNPs coated with ultra-thin F8BT films corresponding to region C of the sample. (a) DF image spectra of the uncoated AgNPs, with the spectrum of a nearby area without a NP subtracted from all the spectra. (b) DF image spectra of the F8BT coated AgNPs, with the spectrum of a nearby area without a NP subtracted from all the spectra.

p. 125.....Figure A2.10. Averaged DF scattering spectra from F8BT coated AgNPs divided by the spectra of F8BT from a nearby region, compared to the F8BT extinction spectra (red line) and compared to the refractive index of F8BT (green line). (a-c) Spectra obtained from region A of the sample, AgNP number 2-4. (d) Spectra obtained from region B of the sample, AgNP number 1.

p. 126.....Figure A3.1. UV visible extinction spectra for the purified product shown in Figure 2a-d (in the main text). Black line is the sample purified immediately after the reagents were added, red line is the PVP weight percent increased by a factor of 6, blue line is the synthesis without an FeCl₃ source, and the pink line is the PVP weight percent increased by a factor of 3.

p. 126.....Figure A3.2. UV visible extinction spectra for the purified products shown in Figure 4a-c (in the main text). The black line is the sample after 5 min, the red line is the sample after 10 min, and the blue line is the sample after 20 min.

p. 128.....Figure A3.3. SEM and photographs of the reaction products for the EG control reaction as well as the 90:10 EG:PEG 200 reaction. (a, b, c) EG control reaction product; (d, e, f) 90:10 EG:PEG 200 reaction product; (b, e) early in the reaction, while heating. (c, f) reaction product after heating. Scale bars are 1 μm.

p. 129.....Figure A4.1.1 Schematic of the polyol process analyzed for a life cycle assessment. Green circles are reagents input into the reaction. Yellow stars are energy inputs. Pink box represents reagents produced/unused.

p. 129.....Figure A4.1.2. Schematic of the sodium borohydride process analyzed for a life cycle assessment. Green circles are reagents input into the reaction. Yellow stars are energy inputs. Pink box represents reagents produced/unused.

p. 132.....Figure A4.1.3. Graphs of the data from the preliminary life cycle assessment comparing polyol and sodium borohydride methods for silver nanoparticle synthesis. (a) Quantification of the environmental impact of the synthesis based on solubility of the synthesis reagents. (b) Quantification of human health impacts for each synthesis. (c) Quantification of the production cost of each synthesis. (d) Quantification of the energy required for each synthesis.

p. 133.....Figure A4.2.1. Schematic, spectrometer image, and PL spectra for few AgNP/PFO samples. (a) schematic of the AgNP/PFO films. (b) Spectrometer image, with the slit closed showing that three individual AgNPs were isolated. (c) PL spectra obtained from the three AgNPs for a range of neutral density filters, which effectively vary the power of the laser exciting the sample.

List of Abbreviations

(in alphabetical order)

Ag – silver
AIS – absorption induced scattering
Al – aluminum
AR – aspect ratio
Au – gold
Cu – copper
DF – dark field
 E_{ex} – excitation energy density per pulse
EG – ethylene glycol
 E_{th} – threshold for spasing
F8BT – poly(9,9-di-n-octylfluorenyl-2,7-diyl)-alt-(benzo[2,1,3]thiadiazol-4,8-diyl)
FVB – full vertical binning
FWHM – full width at half maximum
GaN – gallium nitride
LSPR – localized surface plasmon resonance
MNP – metal-nanoparticle
 n – refractive index
NP – nanoparticle
NR – nanorod
NW – nanowires
PAA – poly(acrylic acid)
PEG – poly(ethylene glycol)
PEG 200 – poly(ethylene glycol) with a molecular weight of 200 g/mol
PEG 300 – poly(ethylene glycol) with a molecular weight of 300 g/mol
PEG 600 – poly(ethylene glycol) with a molecular weight of 600 g/mol
PFO – poly(9,9-di-n-octylfluorenyl-2,7-diyl)
PL – photoluminescence
PVP – poly(vinyl pyrrolidone)
RL – random laser
SEM – scanning electron microscope
SPP – surface plasmon polariton
 t_{PFO} – PFO film thickness
ZnO – zinc oxide
 $\Delta\lambda$ – emission spectral linewidth
 λ_{em} – wavelength of emission

List of Publications

- 1 **J.I. Tracey**, D.M. O'Carroll. Short-Wavelength Lasing-Spasing and Random Spasing with Deeply Subwavelength Thin-Film Gain Media. *Advanced Functional Materials*, **28**, 2018.
- 2 **J.I. Tracey**, S. Aziz, D. M. O'Carroll. The Role of Polyol Molecular Weight in the One-Pot Polyol Synthesis of Silver Nanoparticles. *Submitted*.
- 3 **J.I. Tracey**, Z. Cheng, D. M. O'Carroll. Investigations into Plasmon-Exciton Coupling in Silver Nanoparticle/Conjugated Polymer Films. Manuscript in preparation.
- 4 B. Yu, Z. Cheng, **J.I. Tracey**, M. Vacha, D.M. O'Carroll. Plasmonic Coupling in Sphere-On-Plane Systems Mediated by Semiconducting Polymer Spacer Layers. *Physical Chemistry Chemical Physics*. **20**, 2018
- 5 Z. Shen, Z. Cheng, **J.I. Tracey**, C. Kumah, and D.M. O'Carroll. Modification of Luminescence from Organic, Room-Temperature, Dual-Emission Molecules by Plasmonic Surfaces. Manuscript under revision following peer review.

List of Presentations

- June 19, 2019, Modifying Luminescence from Materials using Metal-Molecule Interactions. Z. Shen, **J.I. Tracey**, W. Liu, Y. Fang, J. Li, D.M. O'Carroll. Poster Presentation. Center for Functional Nanomaterials, Brookhaven National Laboratories Department of Energy Triennial Review 2019.
- November 29, 2018, Investigations of Random Lasing Contributions to Lasing-Spasers. **J.I. Tracey**, D.M. O'Carroll. Oral Presentation. Materials Research Society (MRS) Fall National Meeting 2018.
- November 30, 2017, Silver Nanoparticles/Semiconducting Polymer Hybrid Spasers. **J.I. Tracey**, D.M. O'Carroll. Poster Presentation. MRS Fall National Meeting 2017.
- November 30, 2017, Comparative Life Cycle Assessment of the Polyol and Sodium Borohydride Methods for Silver Nanoparticle Synthesis. **J.I. Tracey**, P. Dilip, J. Kuleshov, K. Vilhauer, C. Yoo, D.M. O'Carroll. Poster Presentation. MRS Fall National Meeting 2017.
- November 29, 2017, Progress in the One-Pot, Polyol Synthesis Method of Uniform Silver Nanorods for Plasmonic Nanostructure Applications. **J.I. Tracey**, S. Aziz D.M. O'Carroll. Poster Presentation. MRS Fall National Meeting 2017.
- November 10, 2017. Investigations into the One-Pot Polyol Synthesis Method: A Quest to Form Uniform Silver Nanorods for Plasmonic Nanostructure Applications. **J.I. Tracey**, D.M. O'Carroll. Poster Presentation. Science Technology Mathematics and Technology Community Outreach Symposium at Rutgers (STEM cosR).
- August 24, 2017, Utilizing Novel Configurations of Silver Nanoparticles and PFO Polymer Films to Achieve Array Spasing. **J.I. Tracey**, D.M. O'Carroll. Oral Presentation. American Chemical Society (ACS) Fall National Meeting 2017.
- August 21, 2017, Synthesis of Tunable Anisotropic Silver Nanorods for Polymeric Light Emitting Devices. **J.I. Tracey**, S. Aziz, D.M. O'Carroll. Poster Presentation. ACS Fall National Meeting 2017.
- July 21, 2017. Assessment of Silver Nanorod Synthesis P. Dilip, J. Kuleshov, K. Vilhauer, C. Yoo, **J.I. Tracey**, D.M. O'Carroll. GSET Oral Presentation. NJ Governor's School of Engineering and Technology (NJ GSET) Symposium
- June 5, 2017. Achieving Array Spasing from Novel Configurations: Silver Nanoparticles and PFO Polymer Films. **J.I. Tracey**, D.M. O'Carroll. Oral Presentation. ACS Middle Atlantic Regional Meeting 2017.
- March 31, 2017. Novel Configurations Utilized to Achieve Array Spasing; Silver Nanoparticles and Poly(9,9-di-n-octylfluorenyl-2,7-diyl) Polymer Films. **J.I. Tracey**, D. M. O'Carroll. Poster Presentation. Eugene Krug Memorial Poster Session.
- December 3, 2015. Green Synthesis of Silver Nanorods Utilizing the Polyol Method for Solution-Processable Optoelectronics. Oral Presentation. **J.I. Tracey**, D.M. O'Carroll. MRS Fall National Meeting 2015.

Chapter 1. Background and Scope of Investigation

Plasmonic nanoparticles (NPs) have numerous applications in optoelectronics, sensing, spectroscopy, and more. They have been employed to enhance the efficiency of light-emitting diodes [1-3]. Plasmonic NPs have been incorporated into solar cell devices to enhance light harvesting [4-6]. Sensitive molecular sensing applications using Surface Enhanced Raman Spectroscopy also rely on plasmonic NPs to enhance the Raman scattering signal of molecular species [7-9]. There are also emerging applications in photonics through the use of plasmon-exciton coupling which forms new hybridized electromagnetic states between the plasmon and exciton [7-11]. Another interesting application is for miniaturization of lasers, which can be broken down into three subcategories: metal NP lasing-spasers [12-15], metal-film plasmonic nanolasers [16-21], and metal-nanoparticle random lasers [22-30]. In this thesis we closely examine two emerging plasmonic phenomena, lasing-spasers and plasmon-exciton coupling. In addition, we investigate the synthesis of anisotropic silver (Ag) NPs.

In this chapter, plasmonics is broadly discussed, beginning with an introduction to the field and a discussion of Mie theory. Next various plasmonic NPs are discussed, including the gain required by each type to overcome the optical losses they experience as reported by various authors [12, 13, 31, 32], and a brief description of several gain materials that are commonly used to overcome these losses [33-36]. This chapter then focuses on the plasmonic properties of Ag and its advantages and disadvantages over other plasmonic materials. Metal-molecule interactions are the next topic covered in this chapter, followed by a detailed description of current demonstrations of plasmonic nanolasers and plasmonic random lasers. Next, descriptions of different methods that have been used to synthesize AgNPs are discussed, with the goal of finding a reliable

procedure to synthesize anisotropic AgNPs. Finally, the overview and scope of this thesis is discussed at the end of this chapter.

1.1 Plasmonics: Utilization of Surface Plasmons

Surface plasmons are collective electron oscillations at a metal-dielectric interface due to an applied electromagnetic field. They can exist between two materials where the real part of the dielectric function changes sign across the interface [9, 37, 38]. This occurs in noble metals, such as gold (Au) and Ag, which are the most commonly used; however aluminum (Al) and copper (Cu) can also be used as plasmonic materials due to their abundance of free electrons, which leads to a negative real part of the dielectric function at optical wavelengths [9, 37, 38]. Localized surface plasmon resonances (LSPRs) are a result of the collective oscillations of the conduction band electrons when light is incident on a conductive nanostructure [9]. They are the localized form of surface plasmons.

Utilization of surface plasmons is key in applications such as Surface Enhanced Raman Spectroscopy [7-9], optical antennas [39, 40], plasmon enhanced light harvesting in solar cells [4-6], and spasers [12-14, 41-43]. Mie theory is a well-established theory that can describe the LSPR of a spherical NP of diameter less than the incident wavelength [12, 31, 44, 45]. However, Mie theory does not fully explain the plasmonic response of more complex shapes, such as nanorods (NR), for which more than one LSPR peak in the extinction spectrum arises from the anisotropy of the collective electron oscillations [44]. Equation 1.1 is an extension of Mie theory, as reported by van der Zande *et al.* [45], which allows for the LSPR of anisotropic NPs to be calculated by

adding a geometrical factor to correspond with each axis of the particle. Figure 1.1a shows predictions of absorption spectra that show where the LSPR band(s) would occur for AgNPs of various dimensions, based off of Equation 1.1 (reported by van der Zande *et al.*) [45],

$$\frac{\gamma}{N_p V} = \frac{2\pi\epsilon_a^{3/2}}{3\lambda} \sum_{j=A}^C \frac{\left(\frac{1}{P_j}\right)\epsilon_2}{\left[\epsilon_1 + \left(\frac{1-P_j}{P_j}\right)\epsilon_a\right]^2 + \epsilon_2^2} \quad (1.1)$$

where N_p is the number concentration of particles, V is the single particle volume, λ is the wavelength of light in vacuum, ϵ_1 is the real part ($n^2 - k^2$) and ϵ_2 is the imaginary part ($2nk$) of the complex dielectric constant of the particles (n is the real component and k is the imaginary component of the refractive index), ϵ_a is the dielectric constant of the medium, P_j is a geometrical factor corresponding to each axes of the particle [45].

These predictions show that NRs exhibit both transverse and longitudinal LSPRs, and that the longitudinal LSPR is tunable by changing the ratio of length to width, which is the aspect ratio (AR) of the NR. The environment that the NP is in plays a large role in the tuneability of the LSPR wavelength; for example, when a AgNP is surrounded by a conjugated polymer (which changes the refractive index surrounding the AgNP), changes to the AgNP AR result in greater shifts in the LSPR wavelength compared to a AgNP surrounded by air. Both of these factors, AR and refractive index of the environment, allows tunability of the LSPR wavelength. Figure 1.1b shows that not only the surrounding media, but the diameter of the AgNPs affects the LSPR wavelength. The

theoretical predictions are of point dipoles - thus the diameter does not affect the LSPR of the theoretical spectra - only the dielectric constant of the surrounding medium has an effect. The measured extinction spectra have two differences; first, they are broader than the theoretical, due to deviations from being a perfect dipole (slight variations in the AgNP shape, not perfectly spherical, slight variations in diameter size, retardation effects). Second the diameter of the nanoparticle does indeed play a role in the LSPR observed.

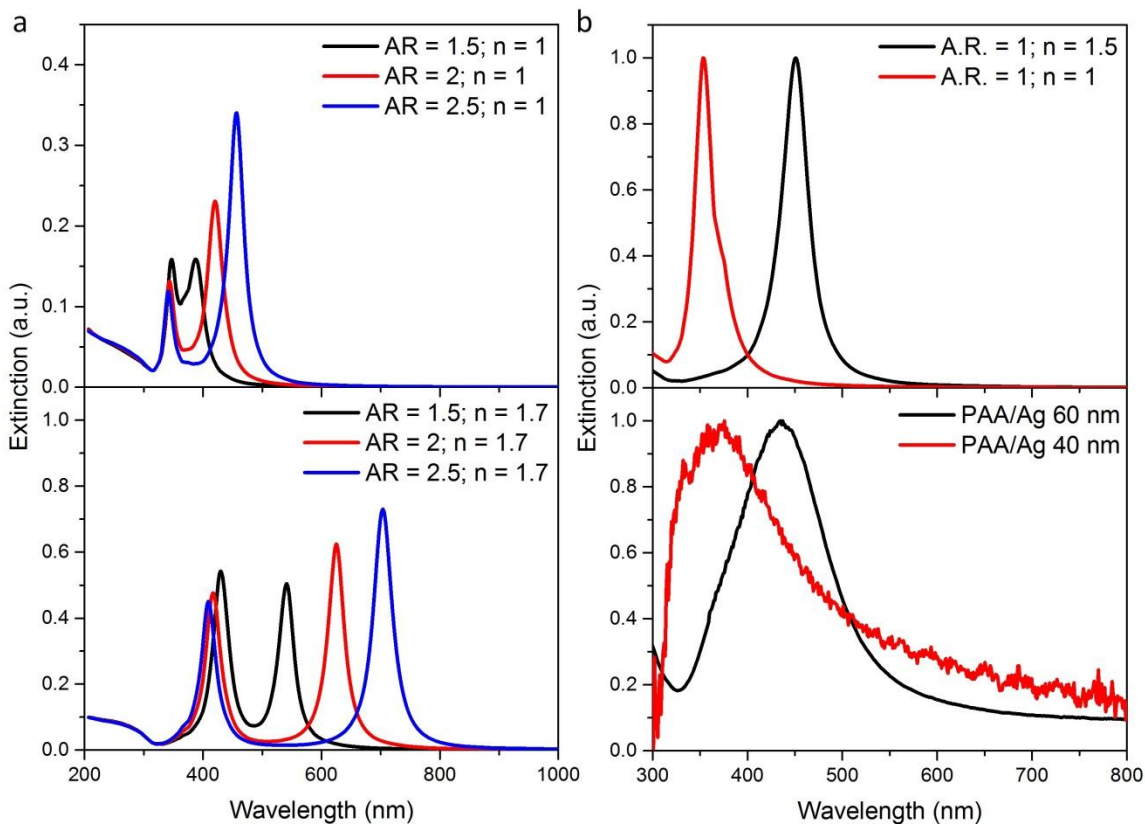


Figure 1.1. Theoretical predictions of the extinction spectra for various AgNPs and experimental extinction spectra for various sizes of AgNPs. (a) Theoretical predictions of the LSPR for varying AR of AgNPs in different refractive indices of the environment. (top) AgNPs in a refractive index, n , of 1 (air). (bottom) AgNPs in n of 1.7 (polymer). (b) Theoretical and measured extinction spectra for the LSPR for spherical AgNPs. (top) Theoretical LSPR predicted for spherical AgNPs with different n of the environment. (bottom) Experimental LSPR for spherical nanoparticles on poly(acrylic acid) (PAA) coated glass, of varying NP diameter.

1.1.1 Gain to Overcome Loss

Plasmonic materials exhibit optical losses that occur largely due to interband electronic absorption transitions in the metal [12, 13, 31, 32]. To suppress these losses, one approach has been to interface plasmonic materials with high gain materials such as laser dyes [12, 13, 22-24, 28, 29, 33], quantum dots [34, 35], or conjugated polymers [25-27, 36]. Several groups have derived equations, from Mie theory as well as from the Drude model, to estimate the gain required for plasmonic structures composed of AuNPs and AgNPs [12, 31, 32]. Table 1.1 summarizes the estimations of gain required as reported by Noginov *et al.*, Lawandy, and Arnold *et al.* [12, 31, 32]. Table 1.1 also includes the amount of gain required as reported by Meng *et al.*, although they do not show their derivation. There is some discrepancy in the exact amount of gain required, as well as whether the shape of the NP contributes to the amount of gain required, likely due to variations in the calculations and derivations employed in different publications.

Table 1.1 Estimated gain required for various plasmonic nanoparticles for stimulated emission of surface plasmons as reported by various groups (references in brackets).¹

Plasmonic Nanoparticle Type	Gain Required to Overcome Loss at Visible Wavelengths
Gold nanospheres	2,250 cm ⁻¹ [31]
	4,000 cm ⁻¹ [12]
	5,000 cm ⁻¹ [32]
Silver nanospheres	1,500 cm ⁻¹ [31]
	600 cm ⁻¹ [32]
Gold nanorod*	~225 cm ⁻¹ [31]
	< 1,200 cm ⁻¹ [13]
Silver nanorod*	~150 cm ⁻¹ [31]

**There have been conflicting reports in the literature about whether the shape of the nanostructure actually contributes to the gain required or whether it is the material the nanostructure is composed of that dictates the gain required. Due to the discrepancy we have included both estimates.*

¹ The estimated gain required is as reported by various authors. There is some discrepancy between the estimates of gain required by each author, which could be due to differences in the authors calculations for gain required or differences in their systems.

The gain calculated should vary with the size of the NP, since the extinction varies with size, due to how the NP absorbs and scatters light, as shown in Figure 1.1b. This variation in size might explain some of the discrepancy for the values reported in Table 1.1. From the estimates of gain required (as reported in various published studies [12, 13, 31, 32]) shown in Table 1.1, it is apparent that Ag requires less gain when compared to the same shaped NP of Au, meaning that the surface plasmons are easier to excite. Therefore, Ag would be a more ideal material for plasmonic applications, based off of gain required. Table 1.2 summarizes the maximum gain coefficients of various materials of interest for plasmonic applications (such as spasers, random lasers, or plasmonic nanolasers).

Table 1.2 Examples of gain materials of interest for lasing-spasers, random lasers, or plasmonic nanolasers along with maximum gain coefficients and processing details.

Gain Material	Gain Coeff.	Processing	Reference
Laser Dyes	$\sim 5,000 \text{ cm}^{-1}$	Doped into a host at low conc.	[33]
Inorganic quantum dots	160 cm^{-1} in host; $68,000 \text{ cm}^{-1}$ self assembled	Ligand stabilized; sometimes doped into a host	[34, 35]
Inorganic semiconductor nanowires	up to $10,000 \text{ cm}^{-1}$	No host required	[33]
Conjugated polymers	up to $12,000 \text{ cm}^{-1}$	No host required	[36]

Organic conjugated polymer semiconductor gain media, have one of the highest gain coefficients due to their large cross section for stimulated emission, since conjugated polymers allow $\pi-\pi^*$ electronic transitions [46]. Furthermore, in addition to their high gain, organic semiconducting conjugated polymers have high chromophore densities, synthetic tuneability, strong room-temperature excitonic emission, biocompatibility, and

more facile processing compared to inorganic semiconductors [46]. Conjugated polymers are comprised of earth-abundant constituent elements, exhibit low toxicity, and are fully solution processable. However, conjugated polymers are derived from petroleum based feedstocks, which make their environmental friendliness debatable. All of these factors make organic conjugated polymers good candidates for the gain medium in plasmonic applications. However, organic conjugated polymers are the least utilized, partly due to their wide absorption and emission spectra, compared to the narrow emission of laser dyes or quantum dots. Additionally, organic conjugated polymers can easily photo-degrade, which hinders their functionality as a gain material [47].

1.1.2 Metals That Support Plasmonic Resonances

The majority of plasmonic NP applications use Au as the material for plasmonic NPs, due to its facile bottom-up synthesis, excellent chemical stability, and reproducibility [16, 38, 48-51]. However, the optical properties of Au are a disadvantage at shorter wavelengths, since Au experiences interband transitions below ~ 500 nm, meaning that LSPRs in the blue region of the visible spectrum are inaccessible [9, 37, 38, 51].

Other plasmonic materials, such as Al, Ag, and Cu are also utilized, but to a lesser extent than Au [9, 15, 17-19]. Al is advantageous in that it requires the lowest amount of gain at UV wavelengths, however, it is only useful for applications in the UV region, due to interband electronic transitions that occur at visible wavelengths [9]. Additionally, the fabrication of Al nanostructures is difficult, due to rapid oxidation, typically only top-down methods, such as using ion beam fabrication techniques are used. The lack of

bottom-up synthesis methods limits Al's solution-based processing applicability [9, 37, 38]. Cu has a strong plasmonic resonance in the far visible and near IR range, but, similar to Au, it is not useful at the short wavelength region of the visible spectrum due to interband transitions below ~ 600 nm [9]. Additionally the surface of Cu oxidizes rapidly, which limits its usefulness for plasmonic applications, all of which are reasons that it is seldom utilized for plasmonic purposes [9].

1.1.2.1 Plasmonic Properties of Silver

Ag has advantageous optical properties as a plasmonic material; such as lower parasitic absorption losses and shorter-wavelength LSPRs (which can be tuned to span the entire visible spectrum) [9, 31]. This arises due to its higher conductivity than Au, Al, and Cu and its absence of interband electronic absorption transitions at visible wavelengths [9, 37, 38, 51]. However, there is a lack of well-developed or reproducible NR synthesis methods for Ag as, chemically, it is less stable than Au. From the gain coefficients reported by various authors [12, 13, 31, 32] and summarized in Table 1.1 it is shown that Ag requires less gain to compensate for optical absorption compared to Au [31], and according to some sources, NRs require lower gain than their spherical counterparts [13, 31], both of which suggest that lower excitation pumping energy should be required to trigger LSPR based stimulated emission using Ag. Therefore, Ag nanospheres and NRs would be better candidates for low loss plasmonic NP applications [31].

Ag nanospheres have a LSPR that is tunable across blue wavelengths. This access to blue wavelengths is important because some of the highest gain semiconducting

conjugated polymers (PFO, F8BT) emit at blue and green wavelengths due to the absence of excited state absorption [36, 46]. Figure 1.2 shows measured photoluminescence (PL) spectra for these polymers compared to the calculated extinction spectra for AgNRs of varying ARs. This is used to theoretically predict which ARs of AgNRs result in plasmonic mode wavelengths that are within the polymer's emission band range. From the spectra it is apparent that PFO's active wavelength range overlaps with the LSPR of AgNPs of AR = 1, and F8BT's active wavelength range overlaps with the LSPR of AgNPs of AR = 1.5.

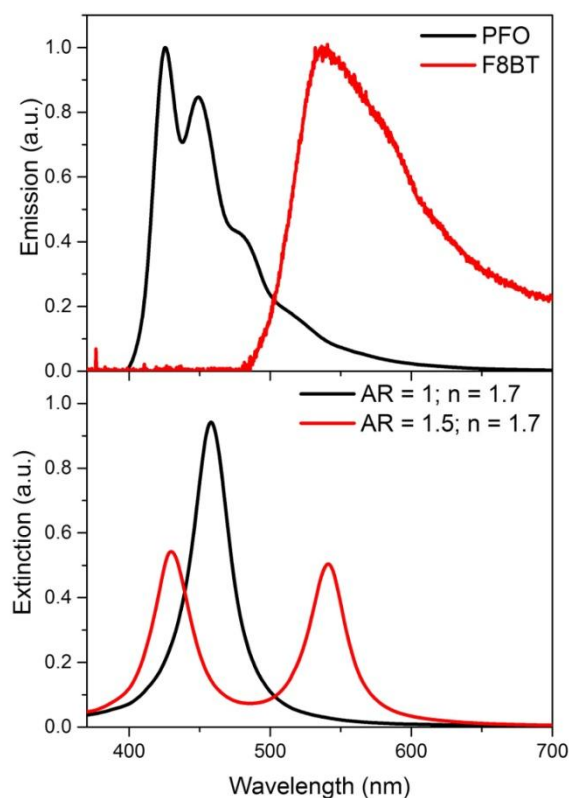


Figure 1.2. Measured PL spectra compared to theoretical predictions for the SPR of AgNPs. (top) The emission of a PFO thin-film (black line) and F8BT thin-film (red line) each were spin coated on a glass substrate. (bottom) The calculated extinction spectra for AgNPs of AR = 1 (spherical NP; black line), and AR = 1.5 (anisotropic NR; red line), each calculation is with a refractive index, n , of 1.7, corresponding to a polymer.

1.2 Metal-Molecule Interactions

1.2.1 Plasmon-Exciton Coupling

Excitons are excited electrons that are bound to a hole, by Columbic forces, and are created by optical or electrical excitation. Excitons can occur in insulators and semiconductors. Organic laser dyes, quantum dots, and J-aggregates are some of the many sources of excitons that have been studied to date for plasmonic applications [7, 8, 10, 11, 52]. Plasmons and excitons have been shown to hybridize, forming plasmon-exciton polaritons, or “plexcitons”. This is of interest because it results in some tunability of the emission, which is important for potential applications such as quantum optics devices [8]. The strength of the hybridization can vary between weakly coupled systems, to strongly coupled systems [7, 8, 10, 11]. Factors that affect the coupling strength include spectral linewidths of the exciton and plasmon resonances, quality of the cavity (ability to confine light), oscillator strength of the exciton, and the number of interacting molecules [7, 8, 10, 11]. The weak coupling regime is useful, in that the plasmons enhance the emission of the excitons [8, 10]. Increasing the strength of the coupling results in hybrid states, which can result in differences (splitting) in the emission wavelengths [8]. Coupling can be observed in many manners. The most commonly reported is spectral splitting in the absorption spectra, but extinction and scattering spectral splitting has also been reported [7, 8, 10, 11]. Spectral splitting has been demonstrated experimentally and theoretically in intermediate and strong coupling regimes [7, 8, 10, 11].

1.2.2 Organic Semiconducting Conjugated Polymers

Organic semiconducting conjugated polymers have not been traditionally employed in plasmon-exciton coupling systems due to their broader spectral linewidths, resulting in less likelihood of strong coupling. However, organic semiconducting conjugated polymers have large chromophore densities, which could potentially overcome the losses experienced by the broader spectral linewidth, and result in strong coupling with surface plasmons.

1.3 Types of Nanoscale Plasmonic Lasers

Miniaturization of lasers (light amplification by stimulated emission of radiation) is important for many emerging technologies, such as biomedical, imaging, spectroscopic, sensing, and communications [12-14, 16-20, 22-30]. Plasmonics is one solution to the problem of the diffraction limit of light (that light cannot be confined to a space less than about half its wavelength, therefore limiting the size of the laser) [9, 41, 42]. By amplifying surface plasmons, instead of light, the size of the laser can be much smaller than the diffraction limit. There have been many reports of plasmonic nanoscale lasers to date. These can be broken down into three subgroups: metal-nanoparticle lasing-spasers [12-15], metal-nanoparticle random lasers [16-21], and metal-film plasmonic nanolasers [22-30]. Table 1.3 summarizes some of the most important examples of nanoscale lasers reported in the literature. We will further discuss these examples, as well as their characteristic properties in this section, as well as in the next chapter.

Table 1.3 Summary of Current Demonstrations of Spasers, Plasmonic Nanolasers, and Random Lasers

Ref.	Materials	Gain thickness	Metal structure Size	λ_{em} (nm)	Excitation laser, λ_{ex} , pulse width/duration, spot size	Rep. rate	Threshold (reported)	Threshold (mJ/cm ²)	Other
<i>Metal-Nanoparticle Lasing-Spasers</i>									
[12]	Au core, organic dye Oregon green 488 in SiO ₂	44 nm shell	14 nm	525	Spasing: 488 nm, 5 ns pulses, focused to 2.4 mm spot. Fluorescence lifetime imaging: 466 nm, <90 ps pulses, 0.24 μ m diameter spot.	40 MHz	9.8 x 10 ⁵ W/cm ²	24.5	Core-shells in solution
[13]	Au@MSiO ₂ NR, organic laser dyes	200 nm Rh6G	20 x 40 nm; 10 nm MSiO ₂ shell	562 - 627	Frequency-doubled Nd:YAG laser, 532 nm, 25 ps pulses, 1.6 mm focused spot on the sample.	1 Hz	1 - 8 μ J	0.039 - 0.313	1.6 x 10 ⁷ /mm ² density of rods; detection spectral resolution 0.07 nm
[14]	Au core, uranine dye doped silica shell	6 nm radius - 25 nm radius shell	10 nm	529	488 nm 7 ns pulse optical parametric oscillator		1.9 - 26 mJ/cm ²	1.9 - 26	Demonstrate images of single spasers, no spectra of single spasers.
[15]	Ag core, coumarin 6 dye doped in a nylon-6 shell			500 - 560	440 nm laser, <100 ps pulse widths, no spot diameter reported	20 MHz	0.1 μ W - 500 μ W	-	No spectral narrowing observed Ensemble measurements
<i>Metal-Film Plasmonic Nanolasers</i>									
[16]	InGaN/GaN NR coupled to a SOG colloidal gold triangle plate	530 nm width, 680 nm length bundle InGaN/GaN	50 nm thick plate several μ m wide	533	Frequency-doubled mode-locked Ti:sapphire laser, 400 nm, 150 fs pulses, optical microscope with 100X objective and 1 μ m collection area.	90 MHz	300 kW/cm ²	3.33	Vertical nanorod array; low temp. experiments at 7K

Table 1.3 continued. Summary of Current Demonstrations of Spasers, Plasmonic Nanolasers, and Random Lasers

Ref.	Materials	Gain thickness	Metal structure Size	λ_{em} (nm)	Excitation laser, λ_{ex} , pulse width/duration, spot size	Rep. rate	Threshold (reported)	Threshold (mJ/cm ²)	Other
<i>Metal-Film Plasmonic Nanolasers</i>									
[17]	CdS NW on a Ag film with MgF ₂ gap layer	~ 200 nm diameter wire	2 - 100 nm gap	489	Frequency-doubled mode-locked Ti-sapphire laser, 405 nm, 100 fs pulses	80 MHz	100 MW/cm ²	1250	-
[18]	Ag film and single NR consisting of GaN shell and green emitting InGaN core	60 nm diameter 170 nm long wire	80 nm	510, 522	Continuous-wave semiconductor diode laser, 405 nm				Atomically smooth Ag; Liquid N ₂ temps
[19]	Triangular GaN NWs on an Al film separated with thin gap layer of SiO ₂	15 μ m long, 180 nm edge length	100 nm Al film, 8 nm gap	370	355 nm, 10 ns pulses (quasi continuous wave), focused to 25 μ m spot (entire NW was pumped).	100 kHz	3.5 MW/cm ²	3500	Thin-film resonator triangular waveguide
[20]	ZnO NWs on Au layers on GaN/Al ₂ O ₃ substrates	200 nm x 4.7 μ m long	-	370 - 373	Frequency-doubled Ti:sapphire laser, 355 nm, 150 fs pulses		2.6 mJ/cm ²	2.6	Inter-rod distance 500 nm Temp. at 10K
[21]	Au bowties with IR-140 dye in polyurethane	-	Bowties-Au NP dimers with gap of ~10 nm	850-910	Ti:sapphire regenerative amplifier, 800 nm, 45 fs-laser pulses with a 4 x 4 mm beam spot size	1 kHz	0.4 mJ/cm ²	0.4	Two different periodicities of the Au bowtie arrays

Table A3.1 continued. Summary of Current Demonstrations of Spasers, Plasmonic Nanolasers, and Random Lasers.

Ref.	Materials	Gain thickness	Metal structure	λ_{em} (nm)	Excitation laser, λ_{ex} , pulse width/duration, spot size	Rep. rate	Threshold (reported)	Threshold (mJ/cm ²)	Other
<i>Metal-Nanoparticle Random Lasers</i>									
[22]	Polymer films (PVA) containing Rh6G laser dye and AuNPs	400 μ m	10 - 150 nm	580	Frequency-doubled Nd:YAG laser, 532 nm, 10 ns pulses	5 Hz	1-20 mJ	0.2 - 4	-
[23]	PMMA films with Rh6G and AgNPs films deposited on Al-coated silicon	40 μ m	12 nm	565	Second harmonic Nd:YAG laser, 532 nm, 6 ns pulses, defocused beam, 0.1 cm ² area illuminated	10 Hz	2 mJ/cm ²	2	substrate provides reinjection of leaking photons.
[24]	PVP-passivated Ag aggregates suspended in ethanol and Rh6G dye	-	-	558	Frequency-doubled, Q-switched Nd:YAG, 532 nm, 10 ns pulses, 1 mm cuvette	10 Hz	-	-	1 mm cuvette
[25]	Multilayer structure, AgNPs doped into each layer: MDMO-PPV, F8BT, and PFO	150 nm films, >600 nm total multi-layer	70 nm	636 565 467	400 nm, 200 fs pulses	1 kHz	R: 13 μ J/cm ² G: 92 μ J/cm ² B: 104 μ J/cm ²	R: 0.013 G: 0.092 B: 0.104	PVA spacer films (~60 nm) thin to avoid waveguide modes.

Table A3.1 continued. Summary of Current Demonstrations of Spasers, Plasmonic Nanolasers, and Random Lasers.

Ref.	Materials	Gain thickness	Metal structure	λ_{em} (nm)	Excitation laser, λ_{ex} , pulse width/duration, spot size	Rep. rate	Threshold (reported)	Threshold (mJ/cm ²)	Other
<i>Metal-Nanoparticle Random Lasers</i>									
[26]	F8BT embedded with AgNPs (no substrate)	200 nm	200 nm	567	400 nm, 200 fs pulses, 3 mm laser spot	1 kHz	2 μ J/cm ²	0.002	-
[27]	Au core-silica shell NPs doped in a film of F8BT/MEH-PPV	300 nm	53 nm	-	532 nm, 300 ps pulses	10 Hz	0.35 μ J/cm ² x10 ²	-	-
[28]	PVA, AgNO ₃ , and Rh6G spin coated on glass substrate then annealed to precipitate AgNPs.	~2.6 μ m	2 nm	567	Second harmonic, mode-locked Nd:YAG laser, 532 nm, 25 ps pulses, stripe width of 17 μ m, stripe length varied from 0.1 - 6.0 mm	10 Hz	1.12 μ J	-	-
[29]	PVP/RhB dye attached to Au NRs AuNPs and Au@Ag NRs	-	60 x 12 nm rod, 40 nm NPs	587 591 611	532 nm		3.2 mJ 0.4 mJ 5 mJ	-	-
[30]	TiO ₂ NPs R6G dye in methanol	-	0.25 μ m rutile structure	570	Second harmonic Q-switched Nd:YAG laser, 532 nm, 5-10 ns pulses, 0.25-0.8 mm spot diameter				

1.3.1 Metal-Film Plasmonic Nanolasers

Metal-film plasmonic nanolasers use propagating surface plasmon polariton (SPP) modes as the source of surface plasmons [16, 18-20, 43, 53, 54]. They are typically nanostructured, by using either nanowires (NW) or NRs on a film of metal, with some spacer layer separating the structures. These are much larger structures, often micrometer in length, with one dimension on the nanoscale. Metal-film plasmonic nanolasers have been demonstrated for a wide range of emission wavelengths (λ_{em}), from 370 nm to 373 nm and from 489 nm to 533 nm [16-20]. This emission in the UV region, as well as the green region of the light spectrum is due to the implementation of different constituents, Al, gallium nitride (GaN), and zinc oxide (ZnO), as well as Au and Ag [16-20]. The threshold of these reported metal-film plasmonic nanolasers ranges widely from 2.6 mJ/cm² – 3500 mJ/cm² [16, 17, 19, 20].

1.3.2 Metal-Nanoparticle Random Lasers

With metal NP random lasers, there is more uncertainty in the exact mechanism of plasmon amplification. It is believed that they arise from photonic modes that occur from random closed loop arrangements of the NPs, meaning that more than one NP is required for random lasing [16, 18-20, 43, 53, 54]. Interparticle coupling and even localized surface plasmons might also contribute to the operation of metal NP random lasers. Additionally, the thickness of the gain medium (typically using thick films), and direction of light collection (collecting emission from the edge of the films) have great importance for metal NP random lasers, in order to fully take advantage of photonic waveguiding modes. Demonstrations of metal NP random lasers showed λ_{em} ranging

from 467 nm to 636 nm using AgNPs, AuNPs, and a variety of different gain media [22-26, 28-30]. The threshold for random lasing varied between $0.002 \text{ mJ/cm}^2 - 4 \text{ mJ/cm}^2$ [22, 23, 25, 26].

1.3.3 Metal-Nanoparticle Lasing-Spasers

Spasers were first proposed by Bergman and Stockman to be coherent surface plasmon sources with dimensions below the diffraction limit of light [9, 12, 13, 38, 41, 55, 56]. Metal NP lasing-spasers use LSPRs as the source of surface plasmons [16, 18-20, 43, 53, 54]. The first experimental demonstration of metal NP lasing-spasers was by Noginov *et al.* and utilized spherical metal-dielectric core-shell hybrid structures dispersed in solution [12]. The second experimental demonstration was by Meng *et al.* and used planar, random arrays of metal NRs coated with laser-dye-infiltrated mesoporous silica on silica glass substrates [13]. Both of these demonstrations employed ensemble measurements, i.e., many metal NPs were probed at once. A third demonstration was reported by Galanzha *et al.* using Au cores with silica uranine dye doped shells [14]. This demonstration was also solution based, and exhibited an emission wavelength of 529 nm, but was different in that they demonstrated in-vivo applications of spasers for biological sensing [14]. Galanzha *et al.* show images of single spasers illuminated, but do not show spectra from a single particle [14]. In theory only one nanoparticle is needed for spasing, but this has not been extensively studied in the reported demonstrations. Additionally, these metal NP lasing-spasers used AuNPs as the source of SPs, resulting in λ_{em} ranging from 525 nm to 627 nm. There has been one report by Stampekoskie *et al.* of metal NP lasing-spasers using AgNPs and

polymerization to trap dye molecules near the surface of the AgNPs; however, this report focused on spaser fabrication rather than demonstration [15]. Despite the use of AgNPs, Stampelcoskie *et al.* reported λ_{em} of ~ 500 nm to 560 nm, which was not notably shorter than metal NP lasing-spasers using AuNPs [15]. There is a need for lasing-spasers that emit in the blue region of the visible light spectrum.

1.4 Properties of Nanoscale Plasmonic Lasers

1.4.1 Threshold

The threshold of a laser is the excitation energy at which the onset of stimulated emission occurs [12-14, 16, 17, 19, 20, 22, 23, 25-30]. This is usually quantified by an emission intensity vs. excitation energy plot, and signified by a linear to superlinear trend line [12-14, 16, 17, 19-23, 25, 26]. The reported thresholds for nanoscale lasers vary wildly, between 0.01 mJ/cm^2 and 3500 mJ/cm^2 [12, 13, 16-20, 22-30]. There is also no correlation between the type of nanoscale laser and the threshold (i.e. no one type has lower thresholds than the others; all types vary). Achieving a low threshold is important since it can result in more energy efficient nanoscale lasers, and potentially could lead towards electrically pumped nanoscale lasers (instead of the current optically-pumped nanoscale lasers) [13, 16, 18, 20, 22, 23, 25, 26]. Some report using extreme measures to lower the threshold of their nanoscale lasers, such as cooling to low temperatures [16, 18, 20]. Although this does result in lower thresholds (average of $\sim 2 \text{ mJ/cm}^2$ to 3 mJ/cm^2) there have been lower thresholds reported at room temperature [13, 22, 23, 25, 26]. The ability for the nanoscale laser to function at room temperature is important for incorporating the nanoscale lasers in devices (such as biomedical devices, imaging,

communication) since cooling the nanoscale lasers to ultra-low temperatures is, typically, not practical, such as for in-vivo biological spectroscopy [14].

1.4.2 Spectral Region

The spectral emission region of nanoscale lasers is important, again, for the potential applications of nanoscale lasers. Each application may require different emission wavelengths, so the ability to access all of the wavelengths across the UV, visible, near infrared, and infrared spectra is vital. The current demonstrations of nanoscale laser largely contain emission in the 500 nm - 600 nm range [12, 13, 16-18, 22-26, 28, 29]. There have been some examples in the near infrared, as well as UV region, but blue emitting nanoscale plasmonic lasers have not been widely demonstrated [19-21].

1.5 Synthesis of Silver Nanoparticles

As mentioned above, AgNPs are of great interest for plasmonic applications, but the synthesis of AgNPs is not as reliable as other plasmonic materials due to the self-nucleation of the Ag precursor in the synthesis [57], as well as instability of the nanoparticles [58-61]. NR synthesis, with tunable aspect ratio, is of particular interest for plasmonic applications, since the NR's transverse and longitudinal modes exhibit two different LSPRs [44, 45]. These dual resonances can then be utilized to overlap with different polymers, or blends, so that multiple emission wavelengths are accessible. Additionally, AgNRs are not readily available for purchase; therefore, they must be synthesized in the laboratory. There are many reported synthesis methods for the solution-based or "bottom-up" fabrication of AgNPs, including seed-mediated methods

[57, 61-65], strong reducing agent methods [66-69], microwave assisted [70, 71], irradiation [72], and polyol methods [57, 73-83], to name a few. Microwave assisted methods are typically used as a green synthesis method, since the energy requirements for heating the solution are less than traditional methods, however microwave assisted methods tend to form inhomogeneous AgNPs [70, 71, 82]. Seed-mediated methods tend to be the most reproducible, since the growth of the AgNPs depends largely on the seeds, but there are limitations to the tunability of the shape and size of the AgNPs that can be formed [57, 61-65]. The strong reducing agent method typically produces small spherical AgNPs, which can be useful as seed particles [66-69]. The use of a strong reducing agent is a drawback of this method too, since the increased reducing power greatly limits the growth of anisotropic AgNPs, and also because sodium borohydride (the typical strong reducing agent used) is an extremely hazardous reagent [66-69].

The most common limitation of these reported methods is that each is suitable for formation of a specific size or shape of AgNP; to tune these properties of the AgNPs, typically, a different method, or a significant change to the method, is required. For example, the seed-mediated method is reported to be highly reproducible and suitable for sphere and rod shaped AgNPs; however, there is not an easy way to tune the length of the AgNRs, while, for formation of AgNWs, the polyol method is more appropriate [57, 61-65, 73-81, 84]. It has been claimed that the polyol method can enable tuning of the size and shape of the AgNPs by changing certain variables (such as temperature, or amount of capping agent) [57, 73-81, 84]. The polyol method is also touted as a greener, more environmentally-friendly method, since it incorporates more green chemistry principles (less harmful reagents, inherently safer chemistry, fewer reagents) than other methods

[57, 73-81, 84-86]. The issue with the polyol method is that the reported procedures vary drastically between authors [57, 61-65, 73-81, 84]. Additionally there are conflicting reports about the roles that each reagent plays, for example some authors report that a chloride ion source is required for anisotropic NP growth, while others do not [57, 61-65, 73-81, 84]. For these reasons, we chose to focus on the polyol method, and to investigate whether smaller, less significant changes would result in tunability of the length of the anisotropic AgNPs, as well as to try to rectify some of the conflicting reports.

1.6 Thesis Overview and Scope of This Thesis

The objective of this thesis is to investigate photonic and plasmonic interactions between plasmonic nanoparticles and conjugated polymers. These interactions are broken down into two subgroups, lasing-spasers, and plasmon-exciton coupling. The combination of silver nanoparticles and conjugated polymers is chosen as it is expected to lead to clear observations of the two aforementioned interactions due to the low loss plasmons supported by silver, and the strongly-bound excitons in the conjugated polymers. In Chapter 2 we investigate lasing-spasers using silver nanoparticles and PFO as a gain medium, demonstrating that surface plasmon amplification is possible with this arrangement. Chapter 3 examines the relationship between plasmons and excitons, by utilizing two different configurations of silver nanoparticles and ultra-thin polymeric layers. In Chapter 4, a different approach is taken to investigate photonic and plasmonic interactions between plasmonic nanoparticles and conjugated polymers. As shown in Figure 1.2, silver nanorods of aspect ratio 1.5 could result in dual wavelength regimes of plasmon/conjugated polymer interactions - the two LSPR of the nanorod overlap with

both the emission of one polymer and the absorption of another. This could result in dual regimes of absorption enhancement and emission alignment, potentially leading to stronger interactions, lower thresholds, and stronger coupling. Therefore, the synthesis of anisotropic silver nanoparticles should be investigated. Chapter 4 investigates the role that the molecular weight of the polyol solvent plays in the polyol method for silver nanoparticle synthesis. Increasing the polymerization, and thus the molecular weight, results in shorter nanoparticles, although just changing the molecular weight does not always result in high yields of the desired anisotropic silver nanoparticles. Finally, in Chapter 5 the main findings and conclusions of the thesis are summarized and future directions of plasmonic nanoparticle/conjugated polymer interactions are discussed; specifically, plasmon-exciton coupling utilizing different exciton sources, single particle spaser investigations, and improvements to the polyol silver nanoparticle synthesis.

Chapter 2. Short-Wavelength Lasing-Spasing and Random Spasing with Deeply-Subwavelength Thin-Film Gain Media*

*Chapter was previously published: Short-Wavelength Lasing-Spasing and Random Spasing with Deeply Subwavelength Thin-Film Gain Media. **J.I. Tracey**, D.M. O'Carroll. *Advanced Functional Materials*, **28**, 2018.

2.1 Abstract

Lasing-spasers are physically-small metal/dielectric structures that emit light via stimulated emission of surface plasmons. To date, there have been two notable demonstrations of visible-wavelength, metal-nanoparticle-based lasing-spaser ensembles, both of which have used gold nanoparticles and laser dyes as the surface plasmon resonators and gain media, respectively. Similar, but distinct, studies have demonstrated plasmonic random lasing arising from multiple scattering and trapping of emission within thin-film gain media due to plasmonic nanoparticles. Plasmonic random lasers typically implement plasmonic nanoparticles within films of organic gain materials, and random lasing is detected in the plane of the film. Here, we report the use of silver nanoparticles and deeply-subwavelength, thin-film, organic semiconducting conjugated polymers for room-temperature lasing-spasers and random spasers. In contrast to other thin-film-based spaser and plasmonic random laser studies that have used gain films ranging from ~ 200 nm to ~ 500 nm in thickness and monitor emission guided to the sample edge, in this study the thickness of the thin-film gain medium ranges from ~ 70 nm to 30 nm and emission is collected normal to the film. This eliminates effects that could arise from optical trapping of scattered emission within the gain medium that is typically associated with plasmonic random lasing. In particular, the use of the conjugated polymer gain medium allows higher chromophore densities compared to dye-doped organic layers, enabling spasing to be demonstrated with deeply-subwavelength thickness thin-films. Samples implementing gold nanoparticles and organic semiconducting conjugated polymers do not exhibit stimulated emission, demonstrating that it is the spectral overlap between the nanoparticle's surface plasmon resonance and the gain medium's emission which is necessary for lasing-spasers. Generally, thinner conjugated polymer films result

in higher lasing-spaser thresholds and shorter emission wavelengths due to reduced physical overlap of the gain material with the local electric near-fields of the silver nanoparticle. While the majority of lasing-spasers exhibit spectrally-narrow, single-mode emission with quality factors of ~ 90 , in some cases multiple, spectrally-narrow emission peaks are detected, with quality factors approaching ~ 250 , and are attributed to random spasing due to instances of plasmonic coupling in small clusters of silver nanoparticles.

2.2 Introduction

Spasers were proposed by Stockman and Bergman to be coherent surface plasmon sources with dimensions below the diffraction limit of light [9, 12, 13, 38, 41, 42, 55, 56]. Theoretical simulations of spasers have been reported [12, 18, 87], as have experimental demonstrations of both metal-nanoparticle (MNP)- and metal-film-based lasing-spasers and plasmonic nanolasers [16, 18-20, 43, 53, 54]. MNP-lasing-spasers use localized surface plasmon resonances (LSPRs) as the source of surface plasmons, while metal-film-lasing-spasers and plasmonic nanolasers use propagating surface plasmon polariton (SPP) modes as the source of surface plasmons [16, 18-20, 43, 53, 54]. The first experimental demonstration of MNP-lasing-spasers was by Noginov *et al.* and utilized spherical metal-dielectric core-shell hybrid structures dispersed in solution [12]. The second experimental demonstration was by Meng *et al.* and used planar, random arrays of metal nanorods (NRs) coated with laser-dye-infiltrated mesoporous silica on silica glass substrates [13]. Both of these demonstrations employed ensemble measurements, i.e., many MNPs were probed at once. Additionally, these MNP-lasing-spasers used gold nanoparticles (AuNPs) as the source of surface plasmons, resulting in emission wavelength, λ_{em} , ranging from 525 nm to 627 nm. There has been one report by

Stamplecoskie *et al.* of MNP-lasing-spasers using silver nanoparticles (AgNPs) and polymerization to trap dye molecules near the surface of the AgNPs; however, this report focused on spaser fabrication rather than demonstration [15]. Despite the use of AgNPs, Stamplecoskie *et al.* reported λ_{em} of ~ 500 nm to 560 nm, which was not notably shorter than MNP-lasing-spasers using AuNPs [15]. To date there are no experimental demonstrations of blue-emitting MNP-lasing-spasers or the application of other gain media besides laser dyes for MNP-lasing-spasers.

Random lasers (RLs) that use MNPs (MNP-RLs) as the scattering media have been treated as a separate field from spasers (despite having similar constituent materials in some cases), since RLs require strong light scattering, and not necessarily surface plasmons for stimulated emission [25-28, 30, 88]. Demonstrations of MNP-RLs showed λ_{em} ranging from 467 nm to 636 nm using AgNPs, AuNPs, and a variety of different gain media [25-28, 30]. For both MNP-lasing-spasers and MNP-RLs, there is a lack of demonstrations in the blue and UV regions of the visible spectrum because of the preference for AuNPs over AgNPs (see Introduction, Table 1.3, for a summary of lasing-spasers, plasmonic nanolasers, and RLs). AgNPs have LSPR wavelengths that are tunable across the visible spectrum [9]. In contrast, accessing blue wavelengths is not possible with AuNPs due to interband electronic absorption at wavelengths below ~ 500 nm [9]; one reason that it is desirable to implement other metal resonators. The access to wavelengths across the visible spectrum is important because it allows for implementation of gain media with high gain coefficients, such as blue and green emitting polyfluorene-based organic semiconducting conjugated polymers (with gain coefficients of up to $12,000 \text{ cm}^{-1}$) [26] such as poly(9,9-di-n-octylfluorenyl-2,7-diyl),

(PFO). In addition to their high gain, conjugated polymers have high chromophore densities, synthetic tuneability, strong room-temperature excitonic emission, biocompatibility, and more facile processing compared to inorganic semiconductors and laser dyes, making them appealing candidates for implementation as the active gain medium [27]. Another reason that it is desirable to implement other constituents (both AgNPs and conjugated polymers) is that the efficiency of the spasers can be theoretically improved (see Introduction Table 1.1, and Introduction Table 1.2 for comparisons).

Here, we demonstrate stimulated emission from AgNPs with PFO coatings with thickness ranging from ~ 30 nm to 70 nm, representing the thinnest-gain-layer, MNP-lasing-spasers reported to date (see Figure 2.1a for sample configuration). The study yields insight into the dependence of lasing-spasing on gain layer thickness and on spectral and spatial overlap of the NP surface plasmon resonance with the PFO gain material. We also identify two regimes of lasing-spasing that are proposed to arise from interactions between the gain material and either individual AgNPs or small AgNP clusters.

2.3 Results and Discussion

From the theory of spasers' functionality, good spectral overlap is needed between the gain medium's emission and the LSPR of the MNP to compensate for the MNP optical losses [12, 13, 42]. Figure 2.1b shows the extinction spectra for PFO and PFO/60 nm AgNPs/poly(acrylic acid), (PAA), samples as well as the photoluminescence (PL) emission spectrum of PFO. Figure 2.1c shows the LSPR of different NPs that could be implemented for spasers, including AgNPs of different diameters (40 ± 4 nm and 60 ± 4 nm, nominally 40 and 60 nm), and 60 ± 4 nm (nominally 60 nm) gold nanoparticles

(AuNPs) to show the spectral overlap between the 0-1 singlet exciton emission peak of PFO and the LSPR of the NPs. The broad band of the LSPR emission of the NPs is due, in part, to the variations in size of the NPs; however this slight variation does not affect the NPs functionality of acting as a spaser. It is, however, the larger change in size, or change in material, that results in a lack of spectral overlap between the LSPR of the NP and the 0-1 singlet exciton emission peak of PFO, and, thus, a lack of spasing. From Figure 2.1b it is evident that there is good spectral overlap between the LSPR of 60 nm AgNPs and the 0-1 singlet exciton emission peak of PFO; however in Figure 2.1c it is shown that simply changing the material, or significantly changing the size of the NP greatly shifts the LSPR of the NP. In this study, PFO is employed as the gain medium and is expected to exhibit a maximum gain coefficient at a wavelength near the 0-1 singlet exciton emission peak wavelength at ~ 450 nm [27, 36]. Therefore, the size of the AgNPs (60 nm) was chosen such that their LSPR wavelength overlapped well with the 0-1 singlet exciton emission peak of PFO. As a control, samples were also fabricated using 60 nm AuNPs to elucidate information about the source of the stimulated emission (from spectral overlap between the LSPR of the NPs and the polymer emission).

Figure 2.2a shows a representative scanning electron microscope (SEM) image showing 60 nm AgNPs on a PAA-coated silicon substrate at a density of ~ 25 NPs/ μm^2 . Controlling the density of AgNPs is important so that interparticle interactions are minimized. An interparticle distance that is a factor of ~ 2 greater than the NP size should minimize significant interparticle electromagnetic coupling; corresponding to a maximum density for uncoupled 60-nm-AgNPs of ~ 31 NPs/ μm^2 (average inter-particle spacing of 120 nm) [89]. At ~ 25 NPs/ μm^2 , the AgNPs in this study had, on average, an interparticle

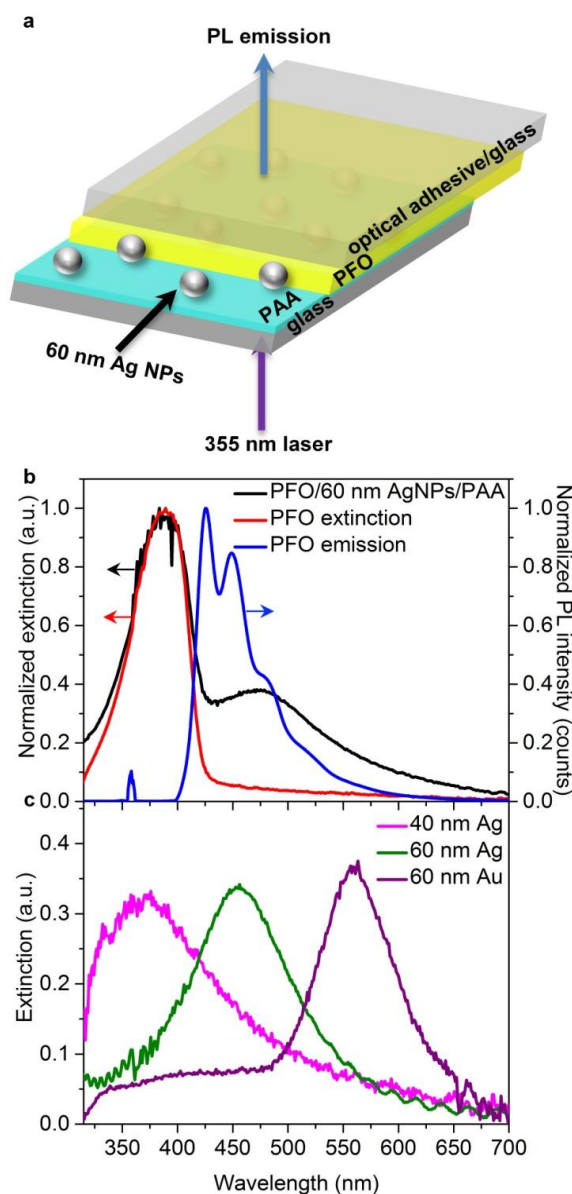


Figure 2.1. Configuration of the samples for lasing-spasers and spectra of constituent materials. (a) Schematic of glass/optical adhesive/PFO/AgNPs/PAA/glass samples showing excitation and PL emission directions. A 355 nm pulsed laser excites the sample from the AgNPs/PAA/glass side of the sample. PL emission is collected from the PFO side of the sample. (b) Normalized, UV-visible extinction spectra and normalized PL emission spectrum for component materials of the lasing-spasers: extinction of PFO/60 nm AgNPs/PAA (black); extinction of PFO (red); PFO PL emission spectrum (blue). (c) UV-visible extinction spectra for different NP constituents: extinction of 40 nm AgNPs/PAA (pink); extinction of 60 nm AgNPs/PAA (green); extinction of 60 nm AuNPs/PAA (purple).

distance for which significant interparticle electromagnetic coupling was not expected; however, a small fraction of AgNPs had interparticle distances less than 100 nm (Figure 2.2a). Dark-field (DF) optical microscopy images of AgNPs on PAA-coated silicon exhibited intense blue backscattering from the LSPR of the individual spherical AgNPs (Figure 2.2a, inset). Figure 2.2b shows a representative DF image for a sample of PFO/AgNPs/PAA/glass (AgNP density of $\sim 25 \text{ NPs}/\mu\text{m}^2$ and PFO film thickness, t_{PFO} , of 70 nm) and indicates AgNP scattering persists when coated with PFO. Neat PFO films did not show significant scattering (Figure 2.2b, inset), indicating that the PFO film did not contribute significantly to the scattering. Figure 2.2c shows a representative PL image of a PFO/AgNPs/PAA/glass sample demonstrating that the PL from PFO is most intense in the vicinity of the AgNPs. In contrast, PL from the neat PFO film is comparatively uniform (Figure 2.2c, inset), and does not display the prominent PL intensity features seen when AgNPs are present (see Appendix 1, Figure A1.1 for DF and PL images of samples with varying t_{PFO}). Figure 2.2d-f show the corresponding microscope images to Figure 2.2a-c, but implementing 60 nm AuNPs instead of 60 nm AgNPs. From the SEM image (Figure 2.2d) the AuNP density is $\sim 18 \pm 2 \text{ NP}/\mu\text{m}^2$ (nominally $20 \text{ NP}/\mu\text{m}^2$), which is comparable to the density of the AgNP samples. The DF (Figure 2.2e) and PL (Figure 2.2f) images for the AuNPs were also similar to the AgNP samples, exhibiting AuNP scattering when coated with PFO. These images demonstrate that the system using AuNPs appears similar to the AgNPs sample, and would act well as a control to determine the cause of the stimulated emission observed.

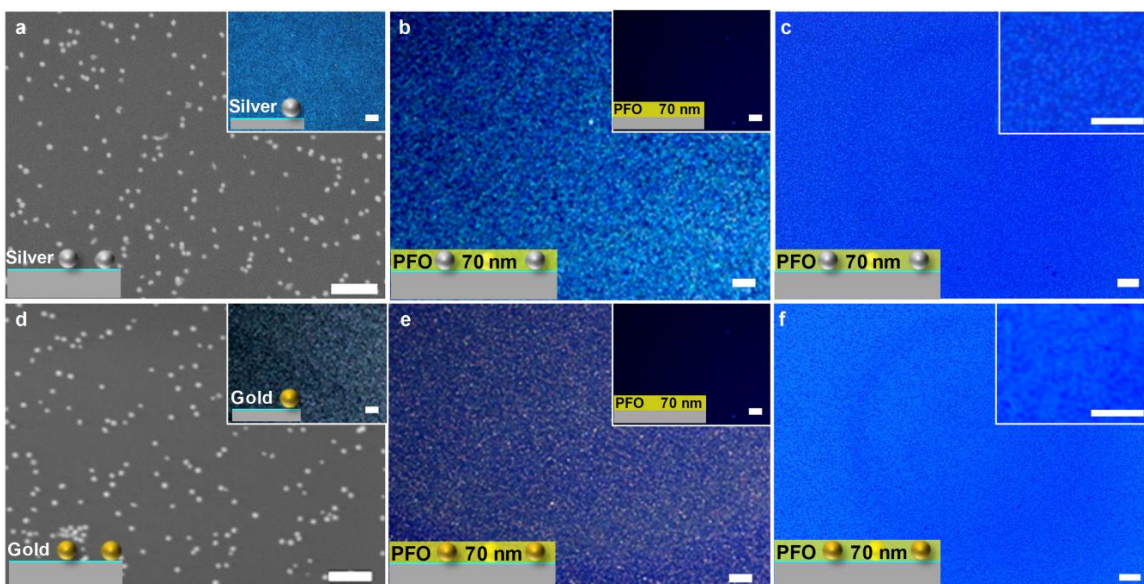


Figure 2.2. Microscopy images with schematics to represent the sample that was imaged. (a) Representative SEM image of an AgNPs/PAA/silicon sample with AgNP density of 24 ± 3 NPs/ μm^2 . Inset in (a) is a DF optical image of the AgNP/PAA/silicon sample. (b) DF optical image of a PFO/AgNPs/PAA/glass sample. (c) PL image of a PFO/AgNPs/PAA/glass sample. The AgNP density is estimated for (b, c) to be ~ 25 NPs/ μm^2 . (d) Representative SEM image of a 60 nm AuNPs/PAA/silicon sample with AuNP density of 18 ± 2 NPs/ μm^2 . Inset in (d) is a DF optical image of the 60 nm AuNP/PAA/silicon sample. (e) DF optical image of a PFO/60 nm AuNPs/PAA/glass sample. Inset in (b, e) is a DF image of PFO/glass. (f) PL image of a PFO/60 nm AuNPs/PAA/glass sample. To remove some of the background, in (c and f) a PL image of the PFO/glass sample was subtracted from the PFO/NPs/PAA/glass samples using Image J. Insets of (c and f) are magnified regions of the PL images from (c and f) to show detail. The AuNP density is estimated for (e, f) to be ~ 20 NPs/ μm^2 . t_{PFO} for (b, c, e, f) and the associated insets was 70 ± 8 nm. Scale bars for the SEM images are 500 nm. All other scale bars are 20 μm .

To further verify that the source of stimulated emission observed is due to the spectral overlap between the LSPR of the NP and the 0-1 singlet exciton emission peak of the polymer, samples were fabricated utilizing 60 nm AuNPs, with similar NP density to the AgNP samples. Figure 2.3 shows the PL spectra obtained from 60 nm AuNP/PFO samples (Figure 2.3a) as well as 60 nm AgNP/PFO samples (including neat PFO samples to verify stimulated emission does not occur in the polymer by itself) (Figure 2.3b).

When using AuNPs, that do not exhibit spectral overlap with the 0-1 singlet exciton emission peak of PFO, stimulated emission, and thus, spasing was not observed, but AgNPs did exhibit stimulated emission, and thus, spasing. The AuNPs, lacking spectral overlap with the polymer, but still possessing plasmonic ability, elucidates that it is indeed the spectral overlap between the LSPR of the NP and the 0-1 singlet exciton emission peak of the polymer that causes the stimulated emission, and not just plasmonic ability. A dielectric NP, which could only exhibit random lasing, could not have been

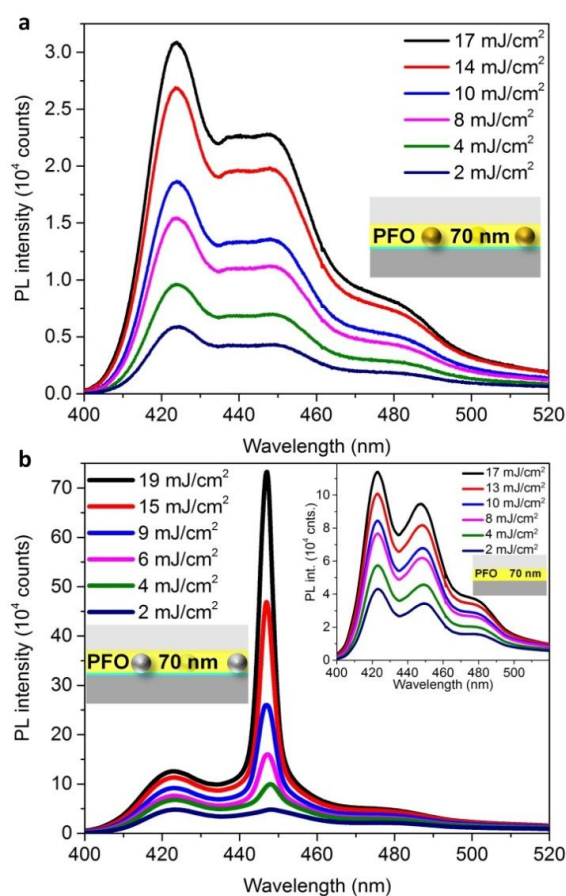


Figure 2.3. PL emission spectra of PFO/AuNPs, PFO/AgNPs, and neat PFO samples. (a) Averaged excitation-energy-density-dependent PL emission spectra from five different regions of one PFO/AuNPs samples with density of AuNPs of ~ 20 NPs/ μm^2 . (b) Averaged excitation-energy-density-dependent PL emission spectra from four different regions of one PFO/AgNPs sample with density of AgNPs of ~ 25 NPs/ μm^2 ; inset in (b) averaged excitation-energy-density-dependent PL emission spectra from four different regions of one neat PFO film (i.e., no NPs). For all of these samples $t_{\text{PFO}} = 70 \pm 8$ nm.

utilized without drastically altering the experimental setup, due to the differences in absorption and scattering by the dielectric NP and would not exhibit resonant extinction that would strongly overlap with the PFO emission 0-1 peak.

To control the spatial overlap between the AgNPs and the gain medium, samples with varying t_{PFO} were fabricated. For simplicity, the samples consisting of glass/optical adhesive/PFO/AgNPs/PAA/glass and glass/optical adhesive/PFO/glass are referred to as PFO/AgNPs and neat PFO, respectively, unless otherwise noted. Figure 2.4 shows PL emission spectra as a function of increasing excitation energy density per pulse, E_{ex} , for PFO/AgNP sample with varying t_{PFO} , with an AgNP density of ~ 25 NPs/ μm^2 ; insets are of neat PFO with the corresponding thickness to the main panel. Spectral narrowing, indicative of stimulated emission, was observed at E_{ex} above ~ 3 mJ/cm² and the emission intensity and spectral narrowing became more pronounced with increasing E_{ex} . The neat PFO thin-films did not exhibit stimulated emission regardless of t_{PFO} and E_{ex} . Since stimulated emission was not present in any of the controls (neat PFO, and neat AgNPs/PAA; see Appendix Figure A1.2), the stimulated emission is attributed to the interaction between the PFO gain medium and the AgNPs, which is characteristic of a lasing-spaser. The intensity of the stimulated emission observed varies from sample to sample. This is less to do with the thickness of the polymer film, but more the manner in which the spectra were collected. Since these spectra are large area measurements, sampling multiple nanoparticles at once, and since the nanoparticle layer is not perfectly uniform (some areas are more dense than others), some regions sampled contained more NPs which likely increased the intensity of the stimulated emission.

The PFO/AgNPs samples with t_{PFO} of 70 nm to 30 nm exhibited stimulated emission with λ_{em} ranging from 444.9 nm to 449.4 nm, which is close to the peak wavelength of the expected gain spectrum of PFO [36, 90] and the LSPR wavelength of the AgNPs. The samples with $t_{PFO} = 25$ nm did not show stimulated emission at high E_{ex} ; instead they exhibited the characteristic spontaneous emission of PFO with 0-0 and 0-1 singlet exciton emission peaks occurring at wavelengths of ~ 425 nm and ~ 450 nm, respectively. The absence of stimulated emission at $t_{PFO} = 25$ nm is attributed to the lack of spatial overlap of the localized electric near-fields of the dipolar LSPR of the AgNP and the gain medium. Physically, the polymer surrounds not even half of the NP, when using 60 nm AgNPs and 25 nm PFO, it is this lack of physical interaction that prevents the interaction between the LSPR of the AgNPs from stimulating the emission of the polymer. The maximum t_{PFO} in this study was limited to ~ 70 nm because, above that thickness, spectral narrowing occurred without AgNPs, attributed to amplified spontaneous emission from a photonic mode. Emission was probed well away from the sample edge to ensure possible contributions from substrate waveguiding or scattering at the sample edge were omitted. Additionally, the absence of a photonic waveguide mode and of a planar PFO/glass interface directly above the AgNPs suppresses trapping of scattered light from the AgNPs which could otherwise promote RL [25, 30]. This further supports the attribution of the observed stimulated emission in the PFO/AgNP samples to lasing-spasing.

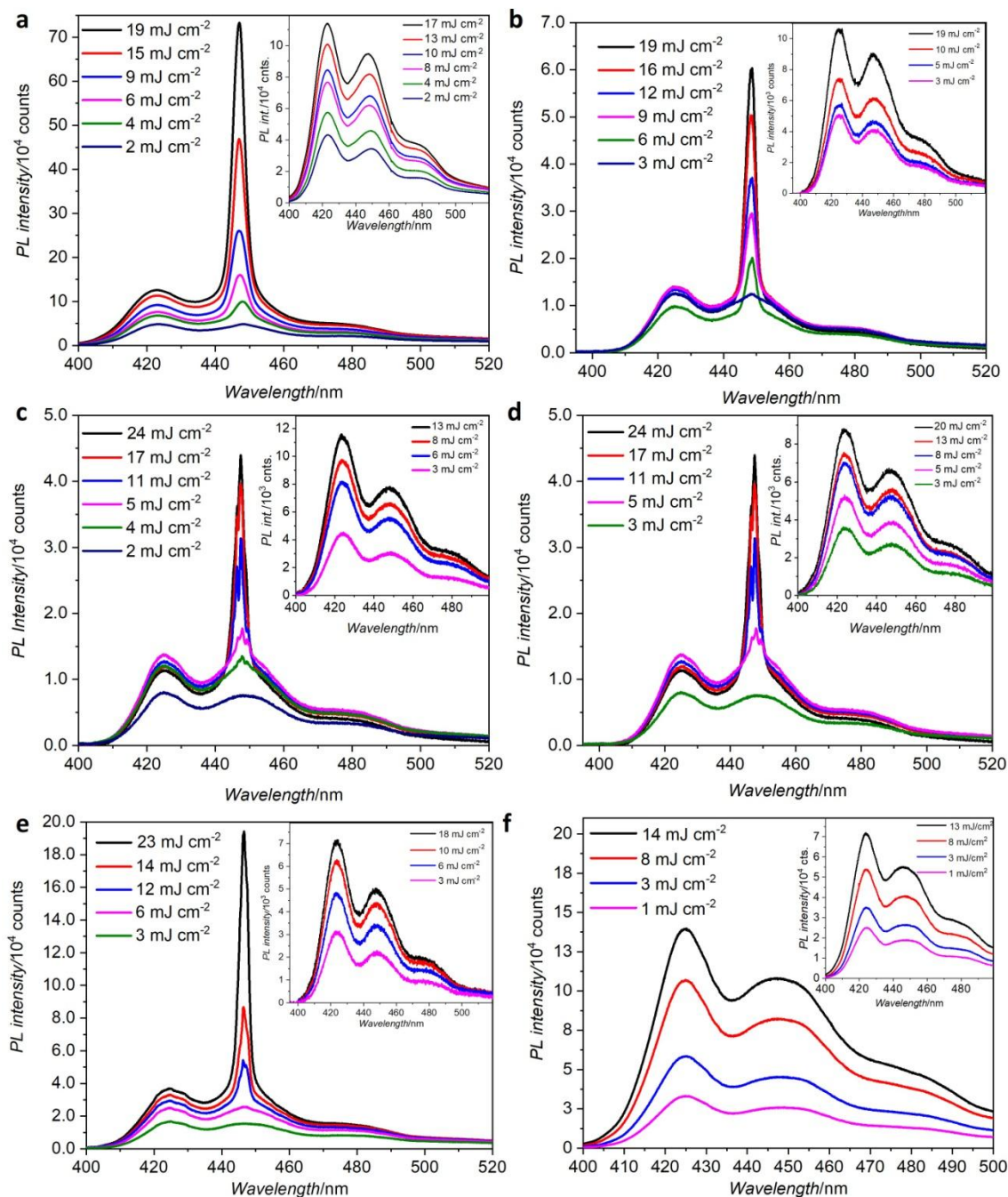


Figure 2.4. PL emission spectra of PFO/AgNP and neat PFO samples with varying t_{PFO} as a function of E_{ex} . Main panel: Excitation power-dependent PL emission spectra for PFO films of varying thicknesses with an AgNP density of 24 ± 3 NPs/ μm^2 (i.e., glass/optical adhesive/PFO/AgNPs/PAA/glass). Inset: Excitation power-dependent PL emission spectra for neat PFO films of varying thicknesses (i.e., glass/epoxy/PFO/glass). (a) 70 nm PFO, (b) 58 nm PFO, (c) 47 nm PFO, (d) 40 nm PFO, (e) 30 nm, (f) 25 nm PFO. Repetition rate was from 104-205 Hz. Each spectrum was averaged from three different regions of one sample.

To determine the threshold for lasing-spasing, the emission intensity and spectral linewidth were analyzed as a function of E_{ex} for samples with and without AgNPs for various t_{PFO} . To enable the various samples to be compared, the 0-1 singlet exciton emission peak intensity of PFO was normalized by the 0-0 PFO emission peak intensity where stimulated emission is not observed. A non-linear trend in emission intensity occurred with increasing E_{ex} for all of the PFO/AgNPs samples tested with $t_{PFO} > 25$ nm and AgNP density of ~ 25 NPs/ μm^2 , due to the onset of spasing. Figure 2.5a shows the spasing threshold plot for six polymer layer thicknesses; 25, 30, 40, 47, 58, 70 nm. The spasing threshold, E_{th} , ranged from ~ 2 mJ/cm² to 8 mJ/cm² (Figure 2.5a). Figure 2.5b shows a plot of E_{th} , averaged for at least three regions on each sample, versus t_{PFO} . As t_{PFO} increased the average E_{th} decreased. For $t_{PFO} = 25$ nm, stimulated emission was not observed, and the 0-1/0-0 emission intensity ratio remained almost constant as a function of E_{ex} .

Additionally, the neat PFO samples did not exhibit non-linear emission intensity behavior, instead exhibiting constant 0-1/0-0 emission ratios as a function of E_{ex} for all t_{PFO} shown. Therefore, it was evident that stimulated emission only occurred when AgNPs were present and when there was sufficient physical overlap between the LSPR of the AgNPs and the PFO gain material. This further confirmed that the observed stimulated emission originated from PFO-AgNP exciton-plasmon coupling as expected for lasing-spasers. The full-width-at-half-maximum (FWHM) for the 0-1 singlet exciton emission peak of PFO was plotted versus E_{ex} for each t_{PFO} to analyze the emission spectral linewidth, $\Delta\lambda$ (Figure 2.5b). It was evident that, near E_{th} , the spectra narrowed

significantly from 48 ± 2 nm to 11 ± 6 nm and spectral narrowing continued down to ~ 5 nm as the E_{ex} increased further.

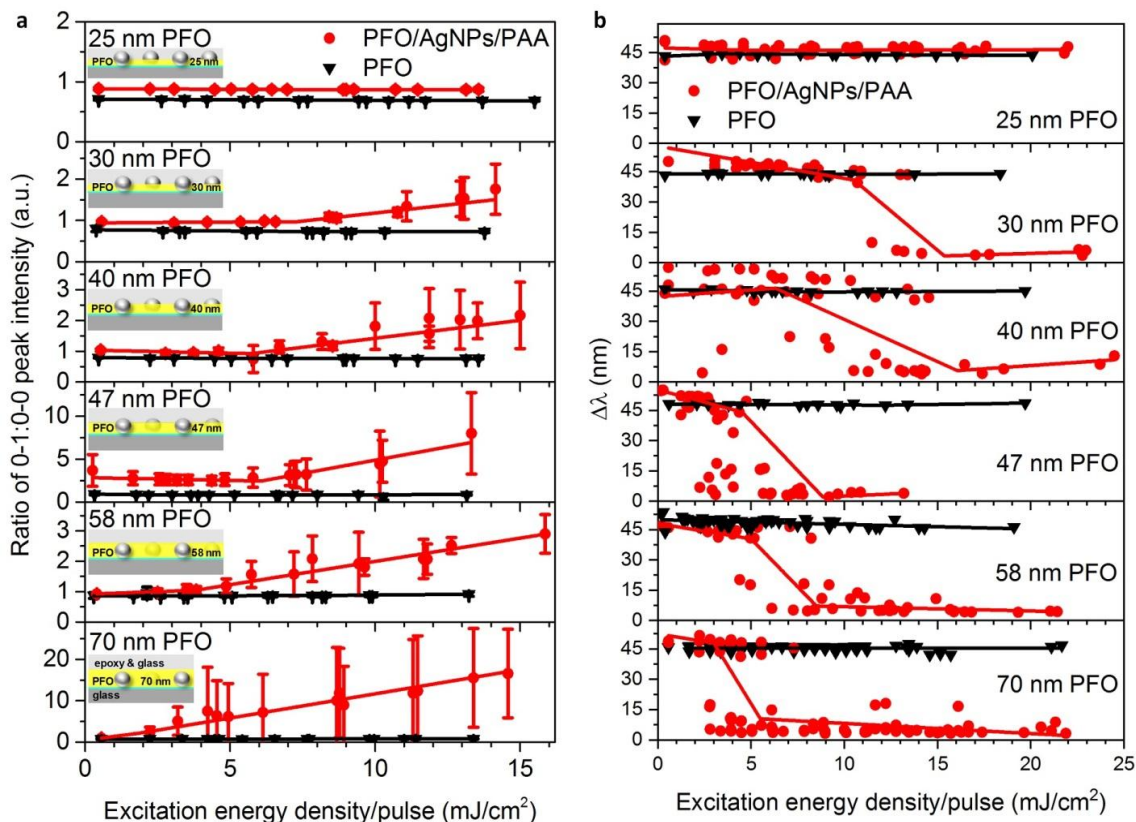


Figure 2.5. Peak 0-1/0-0 emission intensity ratio as a function of E_{ex} and t_{PFO} and $\Delta\lambda$ as a function of E_{ex} and t_{PFO} . (a) Plot of the ratio of the 0-1 emission peak to the 0-0 emission peak of PFO (i.e., 0-1/0-0 emission intensity ratio) for PFO/AgNPs (red circles) and neat PFO (black inverted triangles) samples versus E_{ex} for various t_{PFO} . A piecewise linear function with two linear segments was fit to the data (solid red and black lines). (b) Plot of $\Delta\lambda$ (quantified using the spectral FWHM) of emission spectra from PFO/AgNP (red circles) and neat PFO (black inverted triangles) samples versus E_{ex} for various t_{PFO} . A piecewise linear function with three linear segments was fit to the data (solid red and black lines). For both (a and b) the panels are of samples with nominal t_{PFO} of 25 nm, 30 nm, 40 nm, 47 nm, 58 nm, and 70 nm from top to bottom, respectively. AgNP density was ~ 25 NPs/ μm^2 for all samples. Repetition rate was from 104-205 Hz.

Figure 2.6 shows the λ_{em} for the 0-0 and 0-1 peak of PFO (see Appendix Figure A1.3 for the 0-2 peak compared to t_{PFO}). It is apparent that the λ_{em} of the 0-1 peak

blueshifts above threshold, for all thicknesses, and, generally, λ_{em} decreased with t_{PFO} , likely due to the shift of the LSPR to shorter wavelengths with decreasing effective refractive index of the AgNP environment. Figure 2.6 also shows the E_{th} compared to the t_{PFO} . The E_{th} generally decreases as t_{PFO} increases.

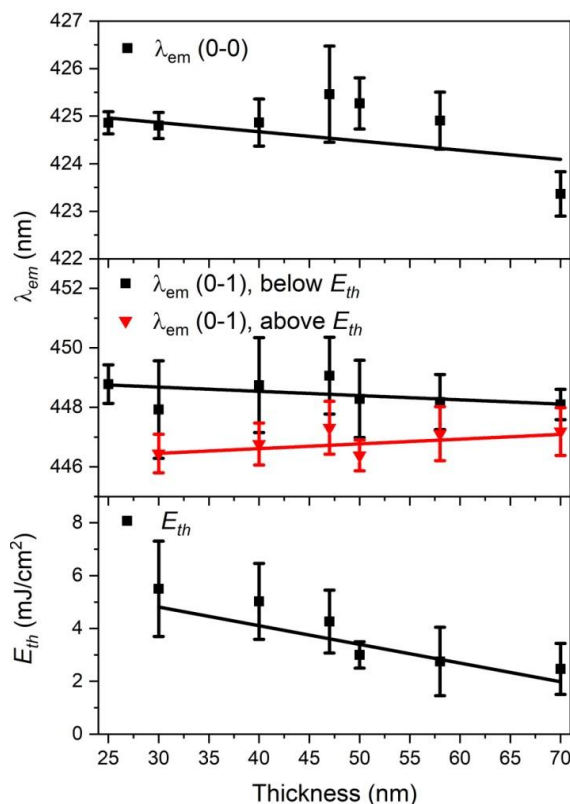


Figure 2.6. Trend of λ_{em} versus t_{PFO} and E_{th} versus t_{PFO} . Top panel: 0-1 peak λ_{em} , below E_{th} (black squares), and above E_{th} (red inverted triangles) for PFO/AgNPs samples versus t_{PFO} . Middle panel: 0-0 peak λ_{em} for PFO/AgNPs samples versus t_{PFO} . For both, the λ_{em} was averaged for at least ten different spectra, at different regions of the sample, leading to potentially different AgNP local densities that cause the larger error in the data, at a range of excitation energies, for each t_{PFO} . Bottom panel: E_{ex} at which there was an onset of stimulated emission (i.e., E_{th}) for PFO/AgNPs samples versus t_{PFO} . E_{th} was averaged from three or more different regions from a sample with the specified t_{PFO} . A linear trend line was fit to the data for each panel.

While the majority of emission spectra from the PFO/AgNPs samples exhibited single mode stimulated emission behavior above E_{th} with $\Delta\lambda \cong 5$ nm (see, for example, Figure 2.7a), in some cases multimode stimulated emission behavior was observed with smaller $\Delta\lambda$. Figure 2.7b shows multimode stimulated emission with pronounced spectral narrowing ($\Delta\lambda \cong 2$ nm) from a sample with $t_{PFO} = 47$ nm. The spectral resolution of the spectrometer is 1.5 nm, meaning that this pronounced spectral narrowing is likely instrument limited. Additionally, a third emission behavior was observed in some cases (Figure 2.7c), which was a combination of the first two; one broader stimulated emission peak ($\Delta\lambda \cong 5$ nm) superimposed with narrower multimode stimulated emission peaks (see examples with other t_{PFO} in Appendix Figure A1.4). The majority of the samples that exhibited single-mode emission, had a quality factor, Q , of ~ 90 , where $Q \cong \lambda_{em}/\Delta\lambda$. However, the spectra demonstrating multimode emission resulted in Q approaching ~ 250 , suggesting better electric field confinement in the gain material. This enhancement in Q is potentially due to spasing arising from instances of plasmonic coupling between AgNPs (rather than discrete AgNP LSPRs) that generates stronger and more localized surface plasmons that are then amplified by the PFO gain medium [91, 92].

Each of these behaviors, single-mode, and multimode stimulated emission, were observed for each t_{PFO} that also exhibited stimulated emission (i.e. 30 nm – 70 nm), indicating that it was not a PFO-film-thickness-dependent phenomenon. Furthermore, the same sample could exhibit one or the other of the emission behaviors depending on experimental collection conditions. When only the center of the defocused emission area was collected, single mode behavior was detected, whereas multimode behavior was detected when the edge of the emission area was collected. When the emission area was

finely focused, allowing for almost all of the beam spot to be collected, discrete multimode behavior was observed (see Appendix Section 1.1 for further discussion, and

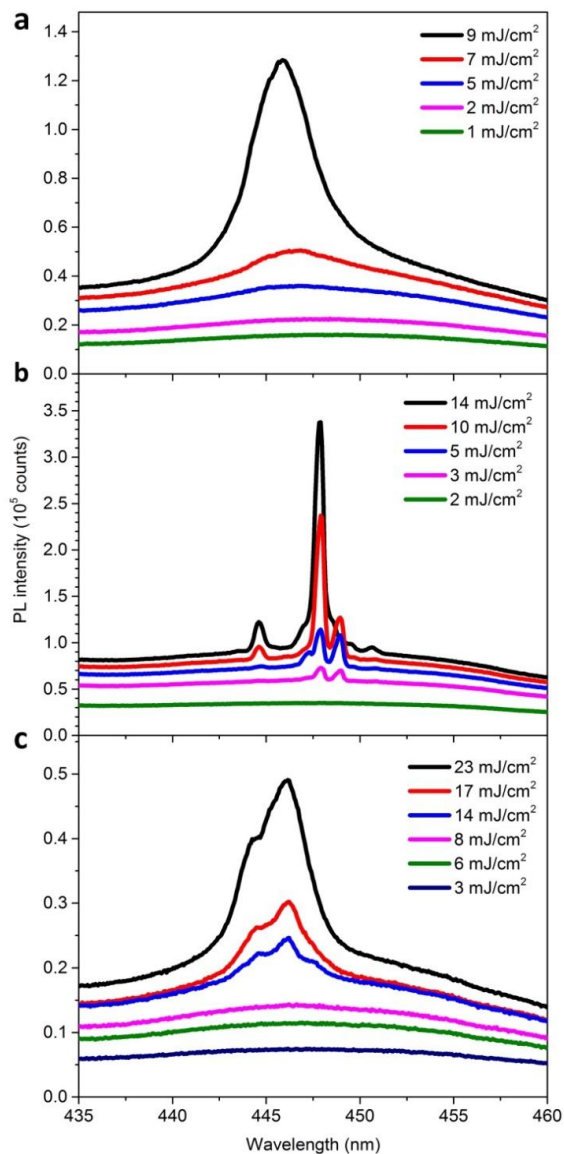


Figure 2.7. Examples of spectrally-narrow, multimode, stimulated emission. (a) and (b): Excitation-energy-density-dependent PL emission spectra from one region of one PFO/AgNPs sample with $t_{PFO} \cong 47$ nm showing (a) multimode stimulated emission and pronounced spectral narrowing, and (b) broader single-mode stimulated emission. (c) Multimode stimulated emission from one region of one PFO/AgNPs sample with $t_{PFO} \cong 30$ nm. The density of AgNPs was ~ 25 $\text{NPs}/\mu\text{m}^2$ for each sample.

Appendix Figure A1.5). Frolov *et al.* and Yu *et al.* each describe instances of collection spot dependence in RLs. When spectra are collected from the center of the emission spot there is the potential for many closed-loop emission paths, which can result in merged RL modes, and thus broader peaks [91, 92]. When spectra are collected from the edge of the emission spot, there are potentially fewer closed-loop paths for RL, thus fewer modes are collected, leading to more clearly-resolved multimode spectra [91, 92]. Due to our observations and the reports by Frolov *et al.* and Yu *et al.* supporting collection area dependence of stimulated emission spectra [91, 92], we propose that the observed multimode emission behavior depends on the collection area, and occurs when a few localized arrangements of AgNPs with interparticle plasmonic coupling modes are sampled. In fact, spasing arising from interparticle plasmonic coupling is consistent with that described for a “random spaser”, as proposed by Wang *et al.* in their recent review article [93].

For a more complete explanation for this behavior it is useful to compare MNP-lasing-spasers and MNP-RLs; as they have many similarities. Single mode emission spectra have been reported in both cases [9, 12, 13, 18, 25-28, 30, 38, 55, 56, 87, 88, 91-93]; however, in some MNP-RLs multimode emission is also observed [25-28, 30, 88, 91-93]. Both use relatively dense ensembles of MNPs; however, the emission mechanisms are attributed to scattering from multiple MNPs in RLs and to the LSPRs of individual NPs in MNP-lasing-spasers [9, 12, 13, 18, 25-28, 30, 38, 49, 55, 56, 88, 91-93]. A distinction between MNP-RLs and MNP-lasing-spasers was made by Meng *et al.*, where they showed that the stimulated emission red-shifted with increasing dielectric constant of the surrounding gain medium, which is indicative of LSPR behavior [13].

MNP-RLs also tend to employ larger gain layer thicknesses due to the reliance on scattering and waveguiding, with the thinnest gain media being 150 nm to 200 nm [26, 91]. In the samples studied here, although there are local regions where the AgNP density is close enough for NP interactions, the gain medium is too thin to support effective photonic waveguiding, with NPs further disrupting potential waveguiding effects [25-28, 30, 88]. Furthermore, RL emission is typically collected from the edge of a sample to take full advantage of the waveguiding modes [25-28, 30, 88]; whereas emission from our samples was collected away from the sample edge and normal to the sample plane (Figure 2.1a), and the PFO thickness was kept below 60 nm to avoid photonic waveguiding modes. Based on the observed collection spot dependence and comparison with RLs, we are led to conclude that traditional MNP-RL emission is not present in the samples studied in this work; though it is apparent that MNP-RL and MNP-lasing-spasers are closely interlinked. Instead, the observed multimode stimulated emission is attributed to lasing-spasing from plasmonic coupling modes in small clusters of AgNPs [94, 95]. When a smaller emission area is collected, lasing-spasing from only a few AgNP clusters may be detected and, distinct, narrow, multimode stimulated emission can be resolved [94, 95].

2.4 Conclusions

In summary, spectral narrowing, spectral collapse, and non-linear emission peak intensity verses excitation energy density has been demonstrated for AgNP/PFO film samples with deeply subwavelength PFO thickness ranging between 30 nm to 70 nm and with AgNP densities of ~ 25 NPs/ μm^2 . These samples have demonstrated spasing

wavelengths between 444.8 nm and 449.4 nm. These characteristics are attributed to lasing-spasing since none of these characteristics were observed for PFO films without AgNPs and with thicknesses below 70 nm. Additionally, PFO film with thickness of 25 nm did not demonstrate these characteristics, indicating that the physical interaction between the gain medium and nanoparticle plays a key role in the functionality of the lasing-spasers. Further supporting this claim, a trend was observed that the threshold for stimulated emission decreased with increased thickness of the gain medium. The stimulated emission was dependent on the spectral overlap between the NPs localized surface plasmon resonance and the 0-1 singlet exciton emission peak of the polymer, as stimulated emission was not observed when there was no spectral overlap (i.e. when AuNPs were implemented instead of AgNPs). Instances of multimode lasing-spasing were also observed and were attributed to stimulated emission from plasmonic coupling modes occurring in AgNP clusters, similar to that expected for random spasers. These results demonstrate functioning short-wavelength emission nanoparticle-based lasing-spasers and random spasers for the first time from a configuration that had not been previously demonstrated: AgNPs and deeply-subwavelength thin-film conjugated polymers.

2.5 Methods

2.5.1 Materials

All reagents were used as received without further purification. Dried, polyvinyl pyrrolidone (PVP)-coated AgNPs (60 nm diameter) were purchased from Nanocomposix Inc. Ethanol (190 proof) was purchased from Decon Labs. PAA, PFO,

chloroform, hydrogen peroxide (30 weight %, containing inhibitor), and sulfuric acid were purchased from Sigma Aldrich, Inc. Ammonium hydroxide and glass cover slides (18 mm x 18 mm; Fisherbrand) were purchased from Fisher Scientific. Optical adhesive (NOA 63) was purchased from Norland Products, Inc.

2.5.2 Methods and Instrumentation

In a typical procedure used to fabricate the samples, first, a PFO solution was prepared by dissolving the amount of PFO needed to give the desired concentration in chloroform (4 mg/mL for about 45-nm-thick PFO films). The sealed PFO solution was then heated in a water bath for 15 min. at 45 °C with magnetic stirring set at 1000 rpm. Then, the PFO solution was sonicated for 15 minutes. Finally, the PFO solution was filtered using a 20 nm syringe filter. Meanwhile, a PAA solution was prepared by dissolving about 5 mg of PAA in 10 mL of ethanol. Also, a AgNP solution was prepared by dispersing the desired amount of dried AgNPs (typically ~ 1.5 mg) in 200 μ L of ethanol by shaking gently, and, if necessary, sonicating for no more than 30 seconds at a time.

PAA was used as an adhesion layer to increase the AgNP density on the glass or silicon substrate. AgNPs were used as the resonant cavity for the lasing-spasers. PFO was used as the gain medium. Each layer was spin coated on glass cover slides that were cleaned using the method reported by Stockton *et al.* [96], which involved immersion in a piranha bath, MilliQ water rinses, immersion in an ammonium hydroxide/hydrogen peroxide solution, additional MilliQ water rinses, and, finally, an ethanol rinse. Spin coating was performed utilizing a Laurell Technology Corporation

WS 400 BZ-6NPP/LITE spin coater, with the following spin coating conditions: 40 seconds spin time, 40 μ L drop size, 9 acceleration, dynamic spin coating. The spin speed varied depending on which layer was being coated: 6,000 rpm for each of the PAA and PFO layers, and 900 rpm for the AgNP layers. There was a waiting period between each layer deposition of \sim 1 min. to ensure that the prior layer had sufficiently dried. After all layers were deposited, optical adhesive was used to secure a glass superstrate (glass cover slide) to the sample in order to passivate the sample. The optical adhesive was cured for \sim 30 min. under UV light (Entela handheld UV lamp).

UV visible extinction spectroscopy was performed utilizing an Ocean Optics FHSA-TTL sample holder and SiPhotonics CCD array UV visible spectrometer. Samples were prepared with many different t_{PFO} , specifically, 70 nm, 58 nm, 50 nm, 47 nm, 40 nm, 30 nm, and 25 nm. For each sample a blank was prepared (glass/optical adhesive/glass) as well as two controls - glass/optical adhesive/AgNPs/PAA/glass and glass/optical adhesive/PFO/glass. The blank was subtracted from the extinction spectra to remove the absorption from the glass and optical adhesive from the extinction spectroscopy measurements. Also the blank was subtracted from the PL spectra to remove the autofluorescence from glass from the PL emission spectra (which can occur when borosilicate glass is illuminated with UV light). The controls were used to verify that stimulated emission did not occur from the AgNPs by themselves or from the neat PFO film by itself.

SEM and DF optical microscopy imaging were used to estimate the AgNP density of the samples. SEM was performed using a Zeiss Sigma Field Emission SEM. DF imaging was performed using a Nikon optical microscope (Optiphot 66) with Carl

Zeiss Inc. Xe lamp and Pixelink camera. PL imaging was performed using a Nikon optical microscope (Optiphot 66) with a 405 nm continuous-wave laser diode, a 425 nm long pass filter, and a Pixelink camera. From the average of many of the SEM images (at least 10 images for each sample) the AgNP density was estimated at between 21 NPs/ μm^2 and 26 NPs/ μm^2 on silicon substrates. While it is expected that, on average, the AgNP density across each sample is between this range; some local variations in AgNP density on each sample is expected. Additionally the SEM images (and density calculations) were performed on silicon substrates. The samples for PL analysis were prepared on glass substrates, so the AgNP density on glass is estimated at ~ 25 NPs/ μm^2 . There is a correlation between the DF images of samples on glass and on silicon substrates, but it is uncertain, the exact AgNP density that was subjected to the excitation laser beam area during the PL measurements.

The excitation-energy-dependent PL spectra were acquired using transmission-mode PL spectroscopy using a 355 nm wavelength, nanosecond pulsed laser (Advanced Optical Technology Ltd., AOT-YVO-25QSP/MOPA ACE) with an externally controlled repetition rate ranging from 100 Hz to 215 Hz (BK Precision 3011B function generator). PL spectra were collected using an Andor Technology Shamrock SR303i-A imaging spectrometer. The laser beam diameter focused on the sample was 0.54 mm. The laser power at the sample was varied using a set of neutral density filters placed just after the laser output port. The lasing power was monitored with an Ophir Vega power meter placed after the neutral density filters, using a beam sampler. A metal plate was placed after the beam sampler to limit the laser exposure of the sample between acquisition of each spectrum. A 400 nm long pass filter was placed

before the spectrometer to limit the 355 nm laser beam from being analyzed by the spectrometer. The spectra were collected with grating 2 (600 lines/mm) in full vertical binning (FVB) mode over a wavelength range of 383-526 nm. The acquisition conditions ranged from 0.1 to 0.4 seconds of exposure, with 40 accumulations for each spectrum to attain acceptable noise. All measurements were carried out at room temperature (see Appendix Figure A1.6 for a diagram the PL set up). Background PL from glass was removed from each PL spectrum (See Appendix Figure 1.2). The repetition rate for the measurements varied between 100 – 200 Hz, in order to achieve similar powers, as measured by the Ophir Vega power meter, between all measurements on different days. The repetition rate did not seem to affect the onset of stimulated emission, nor the emission patterns (multimode behavior, emission peak wavelength, etc).

2.5.3 Trend Line Fitting

To fit the trend lines for Figure 2.4, a nonlinear, piecewise linear fit was used in OriginPro. For the peak intensity ratio versus E_{ex} plots, a nonlinear curve fit, specifically, the piecewise linear two (PWL2) fit (Equation 2.1), was used as programmed, for all plots, both the neat PFO, and the PFO/AgNPs samples. For the $\Delta\lambda$ versus E_{ex} plots, a nonlinear curve fit, specifically, the piecewise linear three (PWL3) fit (Equation 2.2), was used as programmed, for all plots, both the neat PFO, and the PFO/AgNPs samples. In some cases (t_{PFO} of 40 nm and 58 nm) the $\Delta\lambda$ plots needed to be forced to intersect at certain points to ensure a PWL3 fit was achieved (if it was not

forced, a PWL2 fit resulted, or a single linear trend line.) The trend lines in Figure 5 were fitted using a linear fit.

PWL2:

$$\begin{aligned}
 y &= a_1 + k_1x & x < x_i \\
 y &= y_i + k_2(x - x_i) & x \geq x_i \\
 y_i &= a_1 + k_1x_i
 \end{aligned} \tag{2.1}$$

PWL3:

$$\begin{aligned}
 y &= a_1 + k_1x & x < x_{i_1} \\
 y &= y_{i_1} + k_2(x - x_{i_1}) & x_{i_1} \leq x \leq x_{i_2} \\
 y &= y_{i_3} + k_3(x - x_{i_2}) & x \geq x_{i_2} \\
 y_{i_1} &= a_1 + k_1x_{i_1} \\
 y_{i_2} &= y_{i_1} + k_2(x_{i_2} - x_{i_1})
 \end{aligned} \tag{2.2}$$

**Chapter 3. Investigations into Plasmon-Exciton Coupling in
Silver Nanoparticle/Conjugated Polymer Thin-Films**

3.1 Abstract

Surface plasmons have been utilized to enhance the absorption and emission of excitons, by incorporating plasmonic nanomaterials into luminescent thin films. When plasmons and excitons hybridize, they form plasmon-exciton hybrid states, which are important for applications such as quantum optics devices and spasers. The strength of hybridization can vary between weakly coupled systems, to strongly coupled systems, although there have been very few demonstrations of hybridization at the single nanoparticle level or of strongly-coupled plasmon-exciton states. Here, we investigate plasmon-exciton coupling by choosing a conjugated polymer with a strong excitonic absorption band that overlaps with the surface plasmon resonance of spherical silver nanoparticle. We demonstrate that single silver nanoparticles can couple in the intermediate coupling regime with the excitons in thin-films of the conjugated polymer.

3.2 Introduction

As described in detail in Chapter 1.1, surface plasmons are collective electron oscillations that can exist between two materials where the real part of the dielectric function changes sign across the interface. Localized surface plasmon resonances (LSPRs) are a result of the collective oscillations of the conduction band electrons when light is incident on a nanostructured conductive medium [9]. The properties of surface plasmons have been discussed in Chapter 1.1. Excitons are excited electrons that are bound to a hole (electron vacancy) by Columbic forces in materials with relatively low dielectric constant (low electron-hole screening) [7, 8, 10, 11, 52]. Excitons can occur in insulators and semiconductors. Organic laser dyes, quantum dots, and J-aggregates are some of the many materials that have been used to date to study excitons at room

temperature [7, 8, 10, 11, 52]. Excitons and plasmons are known to hybridize, forming plasmon-exciton modes [7, 8, 10, 11, 52]. The strength of the hybridization can vary between weakly coupled systems, to strongly coupled systems. Factors that affect the coupling strength include: (1) spectral linewidths and spectral overlap of the exciton and plasmon resonances; (2) quality of the cavity (ability to confine light); (3) and number of interacting molecules; and (4) oscillator strength of the excitonic material. Coupling can be observed in many manners. The most commonly reported is spectral splitting of scattering spectra, following a Rabi splitting pattern, which is observed experimentally in strong coupling regimes, and theoretically in intermediate and strong coupling regimes [7, 8, 10, 11]. However, other indications of coupling include enhancement of absorption (observed in weak coupling regimes) and enhancement of emission, which is observed experimentally in weak, intermediate, and strong coupling regimes [7, 8, 10, 11]. Where in the spectrum the enhancement occurs largely determines the extent and type of coupling. For example, when enhancement is observed near the absorption edge wavelength of an excitonic material it is termed Absorption-Induced Scattering (AIS), which is an intermediate regime of plasmon-exciton coupling [52].

Organic semiconducting conjugated polymers have not been traditionally employed in plasmon-exciton coupling systems due to their broader spectral linewidths, resulting in less likelihood of strong coupling. However, organic semiconducting conjugated polymers have large chromophore densities, strongly-bound excitons and large oscillator strengths, which can potentially overcome the losses experienced by the broader spectral linewidth, and result in intermediate or strong coupling with surface plasmons [46]. In order for the most likely occurrence for plasmon-exciton coupling to be

observed, the plasmon's resonance should occur at a similar wavelength to the exciton's absorption or emission.

3.3 Results and Discussion

To investigate plasmon-exciton coupling in conjugated polymer/silver nanoparticle films, we choose a conjugated polymer with a strong excitonic absorption band that overlaps with the surface plasmon resonance of silver nanoparticles. Initially, a dense nanoparticle film was fabricated, since, in the previous chapter's study, the LSPR of silver nanoparticles (AgNPs) was not always easily detectable in ensemble measurements, due to the low density of AgNPs. For single nanoparticle studies, we also prepared discrete spherical AgNP films with low nanoparticle density. These will be discussed in more detail in Section 3.3.2.

3.3.1 Dense Silver Nanoparticle Films

To fabricate a densely packed AgNP film, a dewetting method was used (see Section 3.5, Methods, for fabrication method; silver dewetted nanoparticle (AgDW) samples were fabricated by Zhongkai Cheng). The method resulted in hemispherical silver nanoparticles with a density of approximately 387 particles/ μm^2 . Figure 3.1 shows the characterization of the samples. In Figure 3.1a the LSPR of both the AgDW and AgNP samples are shown compared to the absorption and photoluminescence (PL) emission of poly(9,9-di-n-octylfluorenyl-2,7-diy;)-alt-(benzo[2,1,3] thiadiazol-4,8-dily) (F8BT). The LSPR of the AgDW sample is very broad, likely due to the variations in size and shape of the nanoparticles formed with the dewetting method (the average particle

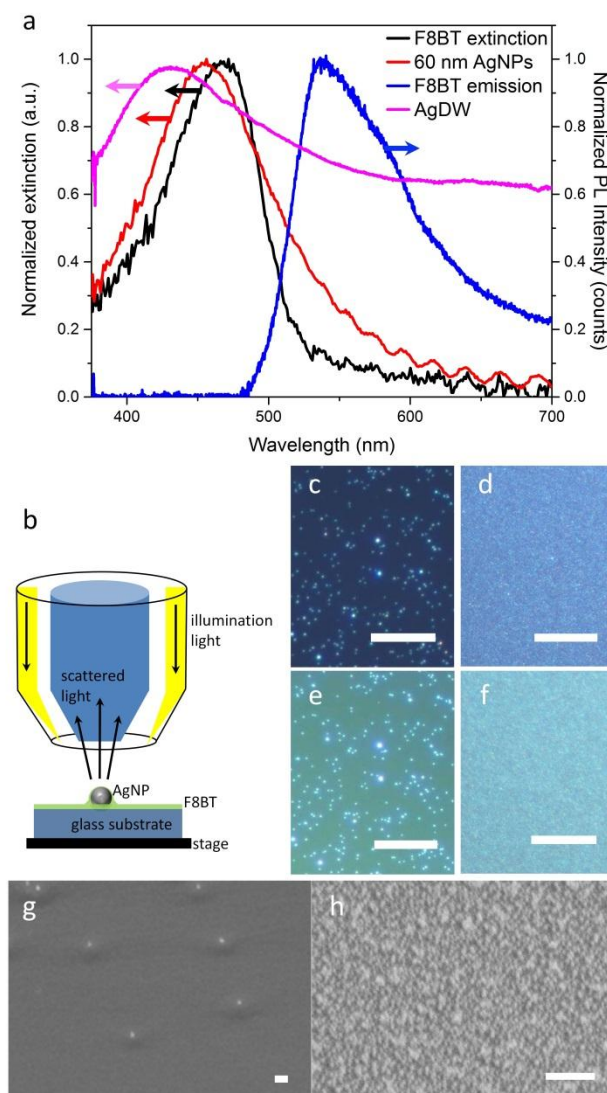


Figure 3.1 (a) Normalized UV-visible extinction spectra and normalized PL emission spectrum for component materials: extinction of F8BT (black); extinction of 60 nm AgNPs (red); F8BT PL emission (blue); extinction of AgDW sample (pink). (b) Schematic of DF microscopy setup, indicating the configuration of the sample. (c-f) DF microscope images of Ag nanostructures on glass; (c) uncoated AgNPs; (d) uncoated AgDW; (e) the same AgNPs shown in (c) coated with F8BT; (f) AgDW coated with F8BT (not the same particles shown in (d)). Scale bars are 50 μm for all DF images. (g) SEM image of F8BT coated 60 nm AgNPs. (h) SEM image of uncoated AgDW sample. Scale bars for the SEM images are 500 nm.

size was 64 ± 25 nm and the average interparticle distance was 45 ± 23 nm for the AgDW samples). Even though there is a broad LSPR for the AgDW sample, there is partial spectral overlap with the absorption of F8BT, meaning that plasmon-exciton coupling

might be possible in this system. Figure 3.1b shows a schematic of the DF microscope setup that was used to analyze the plasmon-exciton interactions.

Figure 3.1c-h are dark-field (DF) and scanning electron microscope (SEM) images of the AgNP and AgDW samples. Figure 3.1d is a DF microscope image of the AgDW sample before coating with F8BT. Figure 3.1f shows a different region of the AgDW sample, after coating with an ultra-thin layer of F8BT. Figure 3.1h is a representative SEM image of the AgDW sample. It is apparent from these images that the AgDW samples have a very dense distribution of silver nanoparticles. The DF images show that the nanoparticles scatter strongly, even when coated with an ultra-thin layer of F8BT. There is a slightly greener color of the F8BT coated AgDW sample, which is expected, since F8BT is a green-emitting polymer. This indicates that the F8BT film coverage is relatively uniform.

After taking the DF microscope images, DF scattering spectra were obtained from the AgDW samples before coating with F8BT (Figure 3.2a). Since individual nanoparticles were not able to be isolated in the AgDW system, due to the increased density of nanoparticles, full vertical binning (FVB) mode of the spectrometer was used to collect the spectra. Then the samples were coated with an ultra-thin layer of F8BT, and spectra were again collected (but from different regions of the sample) (Figure 3.2c). A neat F8BT sample on glass was also prepared so that spectral corrections could be made, and DF scattering spectra were obtained from the neat F8BT sample (Figure 3.2b). The DF scattering spectra of the F8BT coated AgDW samples (Figure 3.2c) results in less intense emission of F8BT (as compared to the neat F8BT samples), which is due to the

AgDW sample absorbing more of the light, rather than scattering the light, as evidenced by the peak observed at about 420 nm.

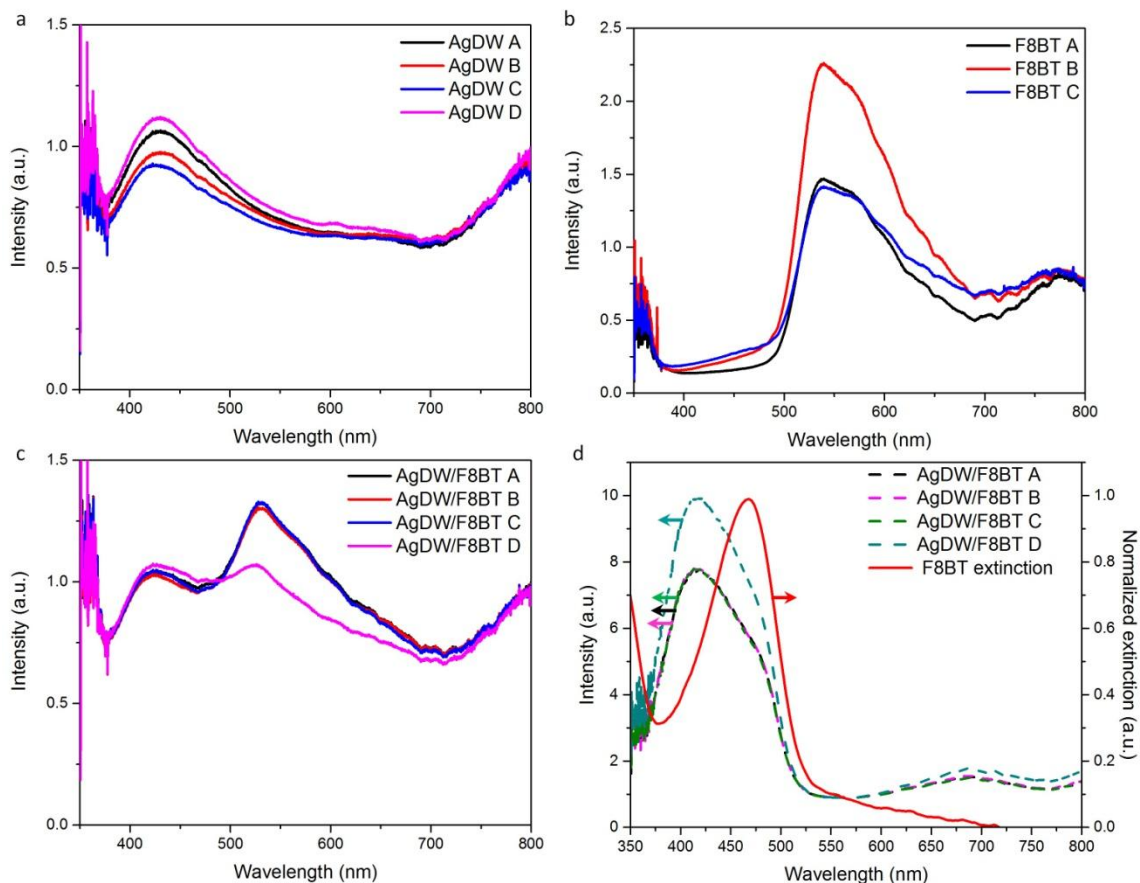


Figure 3.2. DF scattering spectra from AgDW samples and controls. (a) DF scattering spectra of four different regions of uncoated AgDW samples. (b) DF scattering spectra of three different regions of planar F8BT samples. (c) DF scattering spectra for four different regions of F8BT coated AgDW samples. (d) DF scattering spectra of F8BT coated AgDWs divided by the spectra of F8BT from a planar F8BT sample (dashed lines), compared to the F8BT extinction spectra (red).

Figure 3.2d shows the DF scattering spectra from for different regions of AgDW coated with an ultra-thin F8BT film divided by the DF scattering spectra from a neat F8BT film, compared to the absorption of F8BT. This division was performed in order to better elucidate the spectral shape changes due to plasmon-exciton coupling.

Interestingly, for the AgDW/F8BT composites enhancement was observed on the blue-edge of the F8BT absorption peaks wavelength, at about 400 nm. There is an additional shoulder that emerges from this peak, occurring at about 470 nm. These peaks indicate that there is some weak coupling occurring in this configuration. The lack of good spectral overlap of the AgDW scattering with F8BT absorption, and the high absorption losses in the AgDW film are reasons for the weak coupling in the AgDW/F8BT composite.

3.3.2. Single Nanoparticle Studies

Since the AgDW samples only showed weak plasmon-exciton coupling, samples using single, discrete, spherical AgNP were fabricated, in an effort to study a more ideal system, as well as improve the extent of plasmon-exciton coupling observed. As shown in Figure 3.1a the LSPR of 60 nm spherical AgNPs has much better spectral overlap with the absorption of F8BT, and, therefore, should result in better plasmon-exciton coupling. The LSPR of the AgNP can shift depending on the refractive index of the medium it is surrounded by; therefore, when coated with F8BT it is likely to redshift slightly, due to the change in refractive index, which could further improve the spectral overlap of these materials. This indicates that these two materials would be good candidates for plasmon-exciton coupling. DF microscope images were taken before and after coating with F8BT (Figure 3.1c and e) and show that individual AgNPs can be discerned. From these images it is apparent that not only are the same particles being analyzed (since the DF scattering is in the same spots before and after coating), but that when coated with F8BT, although it does alter the scattering color slightly (a more green scattering, which is the

characteristic emission color of F8BT), the AgNP scattering remains strong. SEM imaging (Figure 3.1g) further confirmed that the AgNPs are single and discrete. Samples of 60 nm AgNPs were prepared on glass substrates, as described in Section 3.5, Methods. The AgNP samples were mapped out so that spectra from individual AgNPs could be obtained, and the same particles were able to be relocated after they were coated with an ultra-thin layer of F8BT. Three arbitrary regions, called “A”, “B”, and “C” were chosen for their ease of relocating (to ensure that the same particles were being analyzed before and after coating with an ultra-thin layer of F8BT). Images of these three arbitrary regions are shown in Appendix 2, Figures A2.1, A2.2, and A2.3. DF microscope images and spectra of the AgNP samples were taken prior to coating, and then the AgNP samples were coated with an ultra-thin layer of F8BT (~ 3.75 nm - 5 nm in thickness), the same single AgNPs were relocated, and DF microscope images and spectra were retaken.

Figure 3.3 shows averaged DF scattering spectra for single AgNPs, before and after coating with an ultra-thin-film of F8BT (~ 3.75 - 5 nm), as well as the image spectra that were used to average the DF scattering spectra for the single AgNPs. Spectra of additional regions and AgNPs are shown in Appendix Figures A2.4, A2.5, and A2.6. The LSPR of the AgNPs shift (i.e., do not occur at the same wavelength for all of the individual AgNPs) when uncoated (see Fig. 3.3a), which might be due to variations in the AgNP size or shape. When coated with F8BT, the scattering is at about the same wavelength (see Fig. 3.3b), and is attributed to F8BT emission, since it is very similar in shape to the emission of neat F8BT (see Figure 3.1a for comparison) indicating that the F8BT emission dominates the scattering spectrum. The AgNP is clearly enhancing the

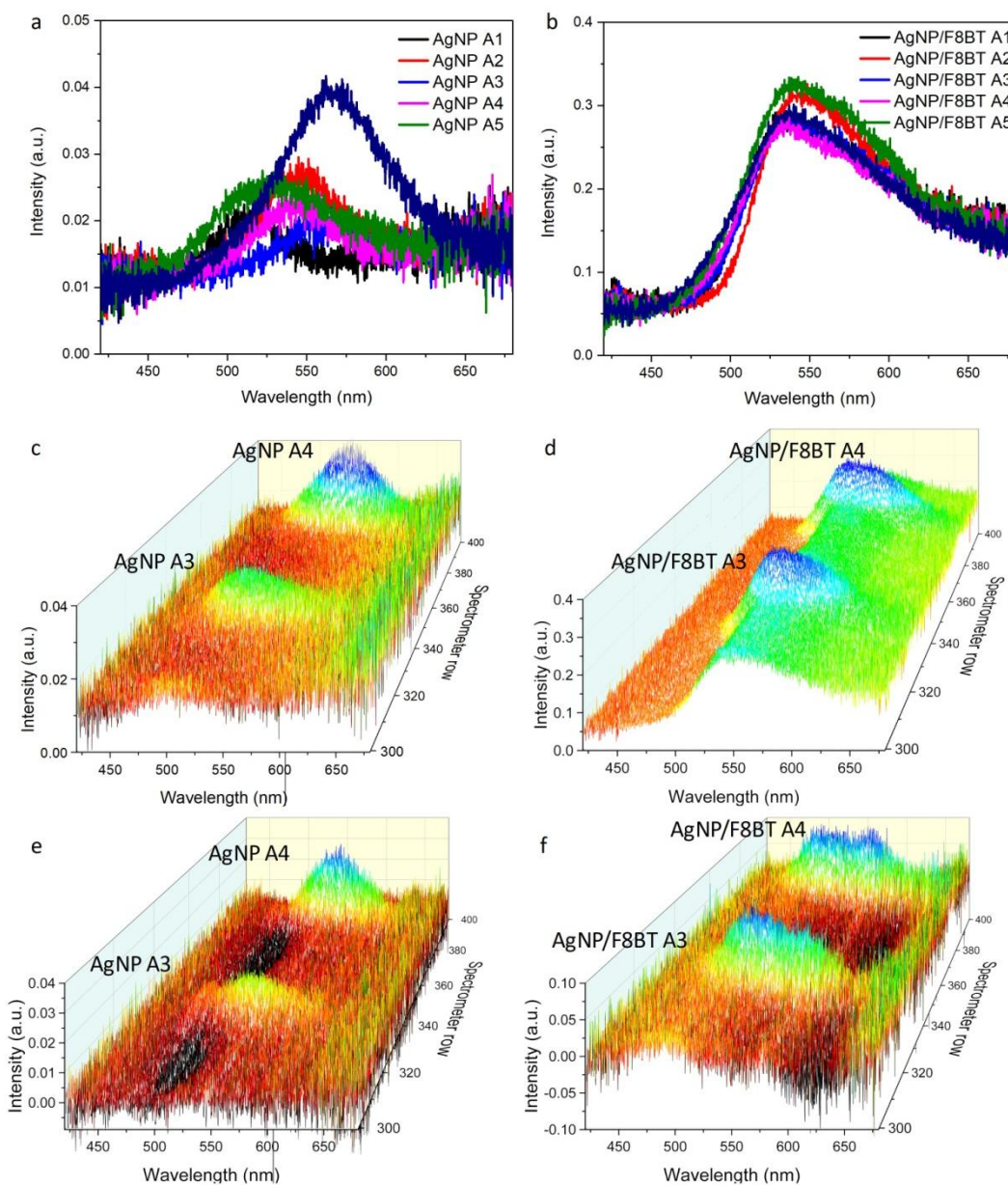


Figure 3.3. DF scattering spectra obtained from single AgNPs and single AgNPs coated with ultra-thin F8BT films. The AgNPs were supported by a glass substrate. (a,b) Averaged DF scattering spectra of five different single AgNPs; (a) before coating with F8BT; (b) after coating with F8BT. (c,d) DF image spectra of two of the AgNPs from (a and b); (c) uncoated AgNPs; (d) F8BT coated AgNPs. (e, f) DF image spectra of the AgNPs with the spectrum of a nearby region where no AgNP was present subtracted from the entire image spectra; (e) uncoated AgNPs; (f) F8BT coated AgNPs.

emission of the F8BT ultra-thin-film, as seen in the waterfall spectra, (Fig. 3.3d). At the rows where AgNPs were present (see Fig. 3.3c) the F8BT spectrum is enhanced.

To further analyze the effect that the AgNPs have on the emission of F8BT, difference spectra were analyzed, in order to better elucidate the enhancement due to the AgNP. First the DF spectrum of F8BT from a region of the sample without any AgNPs present was subtracted from the spectrum of AgNP/F8BT. This was done to further elucidate the amount of enhancement caused by the AgNP. To correct in a similar manner, the spectrum of a nearby region without any AgNPs (i.e., blank glass) was subtracted from the AgNP spectra before they were coated. The DF image spectra for two different single AgNPs, before and after coating, are shown in Figure 3.3e-f (spectra of additional regions and AgNPs are shown in Appendix Figures A2.7, A2.8, and A2.9). From the difference spectra it becomes clear that the enhancement is due to the AgNP, since it occurs at the same spot as the AgNP is located. Additionally, the spectral shape changes; the peak center is blue-shifted compared to the emission of F8BT, which is attributed to coupling between the plasmons and excitons.

The difference spectra better elucidate the enhancement caused by the AgNP; however, in the resulting difference spectra, some spectral shape changes were observed. If, instead of subtracting a nearby region of F8BT, the spectra are divided by the spectra of a nearby region of F8BT, we can better elucidate the spectral shape changes, and thus the extent of coupling that occurs in the plasmon-exciton system. Figure 3.4 shows the division spectra for both the uncoated AgNPs, as well as the same AgNPs after coating with an ultra-thin F8BT layer. In the uncoated AgNP case (Figure 3a, c, e), the division spectra still resembles the LSPR spectral shape, which is expected, since the uncoated

AgNPs should not experience any change in their scattering spectral shape. However, once coated with an ultra-thin F8BT layer, the plasmons and excitons can couple, resulting in enhanced emission as well as a spectral shape change. An intense peak is observed at about 500 nm, for all of the individual AgNPs analyzed, in the division spectrum.

To further analyze the division spectra, the spectrum (averaged from six image spectra which occur at the maximum scattering intensity) for each individual AgNP was compared to the absorption spectrum of F8BT, as well as the refractive index of F8BT (as reported by three groups) [97-99], as shown in Figure 3.5 (spectra for additional AgNPs are shown in Appendix Figure A2.10). When comparing the intense peak, observed at about 500 nm, to the optical constants of F8BT, two things become apparent. First, is that this peak consistently occurs at the absorption edge of the F8BT film, which is also the same wavelength as the LSPR of the AgNP. Therefore, this peak is attributed to plasmon-exciton coupling between the AgNP and the F8BT film, since this peak occurs at the same wavelength as the absorption edge of the F8BT film and also is at same wavelength as the edge of the LSPR of the AgNP. Due to the occurrence of this scattering peak at the wavelength of the absorption edge of the polymer, we are classifying these as instances of AIS, which is an intermediate regime of plasmon-exciton coupling [52]. The intensity of this AIS scattering varied from particle to particle, (for example, Figure 3.4a is from AgNP number A1, which has an intensity of about 1.5 arb. units, compared to Figure 3.4 c, which is from AgNP number C1 and has an intensity of about 2.5 arb. units). The variation in intensity of scattering, and thus variation in coupling, is likely due to slight variations in the uniformity of coverage of the AgNP due to the spin coating fabrication

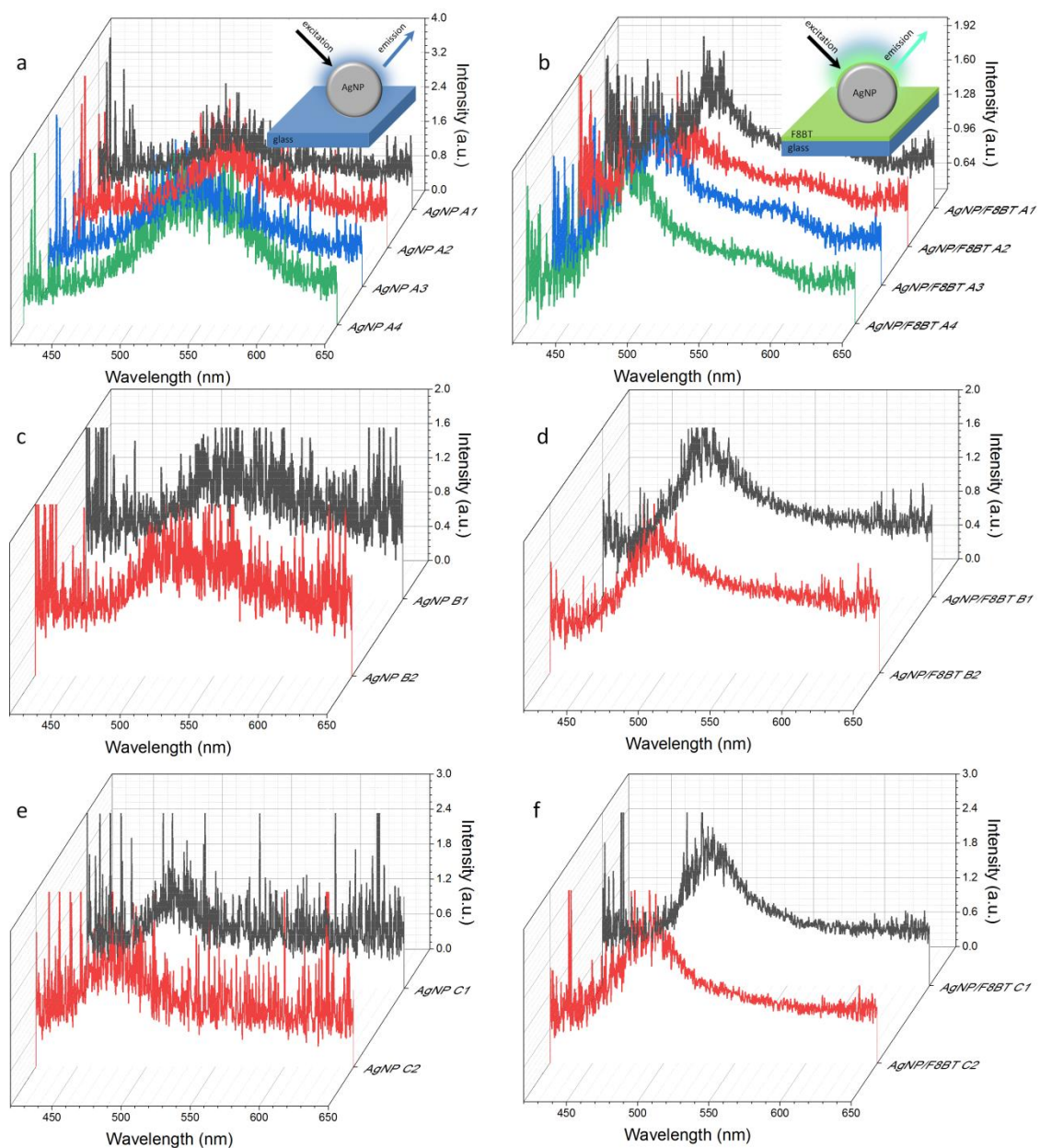


Figure 3.4. DF division spectra. First, each spectrum in the image spectra was divided by a spectrum of a nearby region of the sample, where no AgNP was present. Six spectra from the maximum emission from the AgNP were then averaged. (a,c,e) are the division spectra for the uncoated AgNPs from various regions of the sample. (b,d,f) are the division spectra for the same AgNPs after being coated with an ultra-thin F8BT film. Inset is a schematic demonstrating the enhancement that occurs due to the plasmon-exciton coupling; uncoated AgNPs only scatter at their LSPR, but when coupled, the emission wavelength shifts, as well as is enhanced, with a more intense, blue-green emission detected.

technique. A larger thickness of F8BT is deposited towards the base of the AgNP, with a thinner layer surrounding the top. This non-uniformity would contribute to varying degrees of AIS, since the likelihood of coupling increases with thicker films. It is likely that each AgNP is surrounded by slightly different amounts of F8BT film, and at ultra-thin-film thicknesses small differences in thickness might cause big differences in coupling intensity.

The second observation from this comparison is that the peak observed when dividing the DF spectra by the DF spectra of F8BT closely follows the trend of the wavelength-dependent refractive index for F8BT (as reported by several groups) [97-99]. This indicates that DF scattering spectra of plasmon-exciton coupled systems could be used as a way to qualitatively determine the refractive index of the exciton material. It would be interesting to study further systems to determine if this is true for all compositions, or only certain polymers.

The AgNP samples did prove to be a more ideal system to study the effect of plasmon-exciton coupling. The difference in the extent of plasmon-exciton coupling for AgDW/F8BT and discrete AgNP/F8BT samples could be due to a variety of factors: (1) increased interparticle coupling of AgDW could shift the location and wavelength of the electric field enhancement around the NPs; (2) the shape of the NP is hemispherical in AgDW and spherical for the discrete AgNPs; (3) the sizes of the NPs are expected to be different for discrete AgNPs and AgDW; (4) the shape, size, and density differences may lead to differences in the albedo of the NPs such that there are differences in the amount of absorption loss compared to scattering from the Ag. All of these factors can lead to

variations in the spatial and spectral overlap of the NP plasmonic modes and the F8BT coating, as well as in the strength of coupling between the two media.

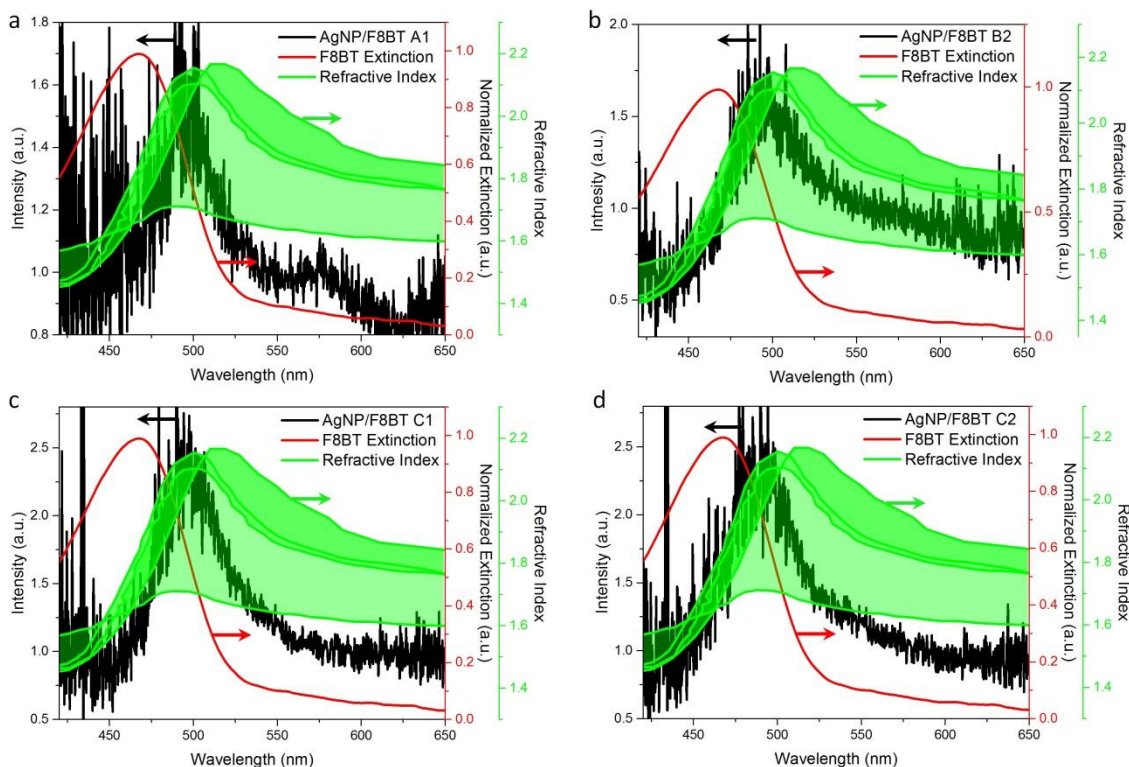


Figure 3.5. Averaged DF scattering spectra from F8BT coated AgNPs divided by the spectra of F8BT from a nearby region, compared to the F8BT extinction spectra (red line) and compared to the refractive index of F8BT (green line). (a) Spectra obtained from region A of the sample, AgNP number 1. (b) Spectra obtained from region B of the sample, AgNP number 2. (c-d) Spectra obtained from region C of the sample, 2 different AgNPs.

3.4 Conclusions

Silver nanoparticles surrounded by ultra-thin F8BT polymer films were investigated to determine if plasmon-exciton coupling could be observed in this system. F8BT was chosen such that its long wavelength absorption band spectrally overlaps with the surface plasmon resonance of the silver nanoparticles. This condition is expected to facilitate the observation of plasmon-exciton coupling in scattering spectra. By probing

single silver nanoparticles, both before and after coating with the ultra-thin F8BT layer as well as regions without any silver nanoparticles present, we clearly observe enhancement in the polymer's emission due to the silver nanoparticles. Furthermore, upon closer examination of the enhancement, it is observed that a pronounced, narrow peak occurs at about 500 nm. Since this occurs at the absorption edge of the polymer, we are attributing this to Absorption Induced Scattering, which is an occurrence of plasmon-exciton coupling in the intermediate coupling regime. To our knowledge this is the first report of a demonstration of intermediate plasmon-exciton coupling observed in conjugated polymer/silver nanoparticle composite films at the single particle level. Plasmon-exciton coupling was also observed in a silver nanoparticle/F8BT system fabricated by the dewetting method, although the coupling was not as strong as that observed in the single silver nanoparticle system.

3.5 Methods

3.5.1 Materials

All reagents were used as received without further purification. Dried, polyvinyl pyrrolidone (PVP)-coated AgNPs (60 nm diameter) were purchased from Nanocomposix Inc. Ethanol (190 proof) was purchased from Decon Labs. F8BT, chloroform, hydrogen peroxide (30 weight %, containing inhibitor), isopropanol, and sulfuric acid were purchased from Sigma Aldrich, Inc. Ammonium hydroxide, glass cover slides (18 mm x 18 mm; Fisherbrand), and Sparkleen 1 were purchased from Fisher Scientific. Silicon wafers were purchased from University Wafer.

3.5.2 Methods and Instrumentation

In a typical procedure used to fabricate the samples, first, a F8BT solution was prepared by dissolving 0.35 mg/mL of F8BT in chloroform. The F8BT solution was capped and sealed with Parafilm, then heated in a water bath for 15 min. at 45 °C with magnetic stirring set at 1000 rpm. Then, the F8BT solution was sonicated for 15 minutes. Finally, the F8BT solution was filtered using a 0.20 µm syringe filter. Meanwhile, a AgNP solution was prepared by dispersing 0.2 mg of dried AgNPs in 1 mL of ethanol by shaking gently, and, if necessary, sonicating for no more than 30 seconds at a time.

AgNPs were used as the plasmon source. F8BT was used as the exciton source. Each layer was spin coated on glass cover slides that were first scored to form “landmarks” in order to be able to relocate the AgNPs before and after coating with F8BT, and cleaned by first wiping the slides with a Kimwipe soaked with isopropanol. Next, the slides were sonicated in a 5 g/L Sparkleen bath for 30 min, then cleaned using the method reported by Stockton *et al.* [96], which involved immersion in a piranha bath, MilliQ water rinses, immersion in an ammonium hydroxide/hydrogen peroxide solution, additional MilliQ water rinses, and, finally, an ethanol rinse. Spin coating was performed utilizing a Laurell Technology Corporation WS 400 BZ-6NPP/LITE spin coater, with the following spin coating conditions: 40 seconds spin time, 20 µL drop size, 9 acceleration, 6000 rpm spin speed, dynamic spin coating. Deposition of the F8BT layer was done several hours after the AgNP deposition (since the sample was imaged to map out the position of the AgNPs).

Silver nanoparticle films fabricated by the dewetting method were also fabricated based off of the procedure reported by Shen *et al.* [100]: ~ 6-nm-thick Ag films were thermally evaporated on bare cover glass in a thermal evaporator (Angstrom Engineering 05846 Nexdep 206 Vacuum Deposition System) at an average rate of ~ 0.1 nm/s. The Ag films were transferred to a vacuum oven (Thermo Fisher Scientific Lindberg Blue M Vacuum Oven) immediately after thermal evaporation of Ag. The vacuum oven was pumped down and heated to 250 °C for 5 min. in order to dewet the Ag from the substrate to form nanoparticles. Afterwards, the samples were allowed to cool to room temperature, while still under vacuum.

SEM and DF optical microscopy imaging were used to verify that the AgNPs were discrete and far enough apart that single particles could be probed. SEM was performed using a Zeiss Sigma Field Emission SEM. DF imaging was performed using a Zeiss AxioVert.A1 inverted microscope with a short arc Xe lamp. Spectra were collected by coupling the microscope signal to an Andor Technology Shamrock SR303i-A imaging spectrometer. The spectra were collected for the AgNP samples with grating 1 (150 lines/mm) in image spectra mode over a wavelength range of 300-900 nm. The acquisition conditions were 10 s exposure, with 20 accumulations for each spectrum to attain acceptable signal to noise. All measurements were carried out at room temperature.

For the AgDW samples spectra were collected in full vertical binning (FVB) mode, with the same conditions as the image spectra (grating 1, wavelength range of 300-900 nm, 10 s exposure, 20 accumulations).

3.5.3 *Spectral Corrections*

To better interpret the spectral trends observed, several corrections were made to the raw spectra. First the background spectrum (spectrum of the room; to correct for stray light) was subtracted from all the raw spectra. Next, the background corrected spectra were normalized to the peak at 827 nm, which is a characteristic peak of the Xe lamp, and not expected to occur in any of the samples, to correct for fluctuations in lamp intensity. Finally, the spectra are divided by the spectrum of the lamp, to minimize the contributions of the lamp. Any additional spectral corrections (F8BT subtraction or division) are mentioned at the relevant points in the text.

Chapter 4. The Role of Polyol Molecular Weight in the One-Pot Polyol Synthesis of Silver Nanoparticles

4.1 Abstract

The polyol synthesis method is a popular approach for fabricating silver nanoparticles of various shapes and sizes. Yet the effect of varying the molecular weight of the polyol on the synthesis product is not well understood. Here, we analyze the effect of changing the polyol solvent, from ethylene glycol to poly(ethylene glycol) with different molecular weights, on the shape and size of silver nanoparticles. Using ethylene glycol, long silver nanowires are synthesized. Under the same conditions, poly(ethylene glycol) of any molecular weight yields shorter nanoparticles with different shapes. Additionally, the impacts that synthesis variables have differ with polyol molecular weight. Using ethylene glycol, chloride ions are required to obtain nanowires; the length of which can be shortened by adjusting the reaction time or the concentration of capping agent. Using poly(ethylene glycol), these synthesis variables have different outcomes: chloride ions do not affect the yield; neither does the concentration of the capping agent.

4.2 Introduction

The synthesis of silver nanoparticles is of great interest because silver's plasmonic abilities span the entire visible spectrum and can be varied depend on the shape and size of the silver nanoparticle (AgNP) [9]. Nanorod (NR) synthesis, with tunable aspect ratio, is of particular interest for plasmonic applications, since the NR's transverse and longitudinal modes exhibit two different localized surface plasmon resonances (LSPRs) [44, 45]. These dual resonances can then be utilized to overlap with different polymers or blends so that multiple emission wavelengths are accessible, which could lead to dual enhancement regimes, or stronger plasmon interactions. There is the

potential for the observation of both plasmon-exciton coupling, as well as plasmon amplification, if a nanorod with a transverse LSPR that spectrally overlaps with the absorption band of the polymer, and a longitudinal LSPR that spectrally overlaps with the emission band of the polymer is used (i.e. plasmon-exciton coupling and spasing observed in the same system). This could also result in improved efficiency, or stronger metal-molecule interactions, potentially even dual regimes of metal-molecule interactions (absorption enhancement and emission alignment).

There are many reported synthesis methods for the solution-based or “bottom-up” fabrication of AgNPs, which are discussed in the Introduction Chapter, Section 1.5. Each method is suitable for formation of a specific size or shape of NP. To tune the size or shape of the NP, typically, a different synthesis method or significant changes to the method are required. However, it has been claimed that the polyol method can enable tuning of the size and shape of the NPs by changing certain variables (such as temperature, or amount of capping agent) [57, 73-81, 84]. Besides this claimed easy tunability of the synthesis, the polyol method is touted as a greener, more environmentally-friendly method, since it incorporates more green chemistry principles (less harmful reagents, inherently safer chemistry, fewer reagents) than other methods [57, 73-81, 84-86]. For these reasons, we chose to focus on the polyol method, and to investigate the role that different molecular weight polyols play in the tunability of the synthesis of anisotropic AgNPs.

There are many polyol method reports that involve different solvents ranging from ethylene glycol (1,2-ethanediol) and its polymers (poly(ethylene glycol) (PEG) of various molecular weights) to various other diols (1,2-propanediol, 1,4-butanediol, and

1,5-pentanediol) which are closer in molecular mass to ethylene glycol (EG) [9, 57, 73-84, 101, 102]. Park *et al.* report that the viscosity effects the diffusion rate of the Ag atoms; with higher viscosity the diffusion rate is decreased [101]. Park *et al.* also report that the polyol method relies on several parameters: concentration of Ag precursor, reducing capacity of the polyol, and the medium's viscosity [101]. Although Park *et al.* has taken preliminary steps to investigate the effect of changing the solvent by using various diols [101], it would be prudent to investigate a wider range of viscosities and molecular weights. The solvent in the polyol method is particularly important since it plays a dual role in the formation of AgNPs, in that it acts not just as the solvent, but also as the reducing agent [77, 80, 84, 103, 104]. Abdel-Motaleb *et al.* reports that increasing the polymerization of the polyol, results in greater capping strength, meaning that the solvent is acting not just as the solvent and reducing agent, but also as the capping agent [104]. These reports by Park *et al.* and Abdel-Motaleb *et al.* indicate that the solvent is one of the key variables in the synthesis of different NP shapes when using the polyol method [101, 104].

Because of this, we hypothesize that this one variable, the solvent, plays a significant role in the tunability of the NPs. The reports from Park *et al.* and Abdel-Motaleb *et al.* further support our hypothesis that the solvent is likely a key variable for tuning the shape and size of the synthesized AgNPs [101, 104]. However, comparisons of polyol syntheses of AgNPs with different molecular weights of the polyols have not been previously reported. Here, we employ four different polyols; EG, poly(ethylene glycol) of a molecular weight 200 g/mol (PEG 200), poly(ethylene glycol) of a molecular weight 300 g/mol (PEG 300), and poly(ethylene glycol) of a molecular weight 600 g/mol (PEG

600), in order to compare the effect that the molecular weight of the polyol has on NP formation. After comparing the effect of molecular weight of the polyol, two polyols were focused on, to investigate the role that other synthesis conditions (temperature, time, and capping agent to metal ion source ratio) play in the polyol process.

4.3 Results and Discussion

In order to systematically analyze the polyol method many synthesis trials were performed, with different variables investigated in each trial. Table 4.1 summarizes the reaction parameters for each trial reported in this chapter. The investigations are broken into four subgroups, where specific variables were investigated in each of those subgroups. First, the effect of the solvent is investigated utilizing a procedure similar to that reported by Jiu *et al.* [79], which is an EG polyol method. The same procedure was followed in this work, the only difference being the polyol solvent used. The next subgroup was an in-depth investigation into the EG polyol method, to determine if other variables (besides the solvent) could result in tunability of the aspect ratio of anisotropic nanoparticles. Again the procedure for this subgroup was loosely based off of the method reported by Jiu *et al.* [79]. Third, an in-depth analysis of the PEG 300 solvent was performed, with similar variables investigated as in the EG solvent analysis. For this PEG 300 study, the procedure was altered, to better align with reports that use higher molecular weight polyols as the solvent, such as the report by Dong *et al.* [105]. The final subgroup investigated were other variables which were hypothesized to have an effect, such as not heating the solution, or mixing the solvents.

Table 4.1. Summary of the reaction conditions for the various Ag nanostructure synthesis trials.

<i>Trial / Polyol Solvent</i>	<i>Total Volume of Polyol (mL)</i>	<i>AgNO₃ conc. (mol/L)</i>	<i>PVP conc. (mol/L)</i>	<i>FeCl₃ conc. (mol/L)</i>	<i>Duration of addition (min.)</i>	<i>Total Reaction Time (h.)</i>	<i>Temp. (° C)</i>
EG	12.5	0.047	0.032	2.40 x 10 ⁻⁵	10	1.66	150
PEG 200	12.5	0.046	0.032	2.52 x 10 ⁻⁵	14	1.73	150
PEG 300	12.5	0.046	0.032	2.34 x 10 ⁻⁵	20	1.83	150
PEG 600	12.5	0.046	0.032	2.40 x 10 ⁻⁵	90	3	150
EG reaction time	12.5	0.046	0.031	2.40 x 10 ⁻⁵	8	n/a	150
EG no FeCl ₃	12	0.048	0.033	-	10	1.66	150
EG 3x PVP	12.5	0.030	0.130	2.40 x 10 ⁻⁵	10	1.66	150
EG 6x PVP	12.5	0.015	0.134	2.40 x 10 ⁻⁵	10	1.66	150
PEG 300 reaction time/temp	5	0.010 ²	0.196	-	-	8.5	70 - 175
PEG 300 FeCl ₃	6	0.085 ³	0.787	0.013	-	7	90
PEG 300 3x PVP	6	0.086 ⁴	0.407	-	-	7	90
PEG 300 6x PVP	6	0.086 ⁵	0.793	-	-	7	90
PEG 300 no heat	5.05	0.010 ⁶	0.196	-	-	0.08 - 0.33	20 - 30.
EG:PEG 200 50:50	6.5:6	0.047	0.031	2.40 x 10 ⁻⁵	10	1.66	150
EG:PEG 200 90:10	11.5:1	0.046	0.032	2.40 x 10 ⁻⁵	10	1.66	150

² Initial concentration was in water: 1.024 mol/L H₂O (0.009 g/50 µL H₂O)

³ Initial concentration was in water: 0.597 mol/L H₂O (0.101 g/1 mL H₂O)

⁴ Initial concentration was in water: 0.603 mol/L H₂O (0.102 g/1 mL H₂O)

⁵ Initial concentration was in water: 0.601 mol/L H₂O (0.102 g/1 mL H₂O)

⁶ Initial concentration was in water: 1.024 mol/L H₂O (0.009 g/50 µL H₂O)

4.3.1 Effect of Solvent

First, the effect that the solvent plays on AgNP growth was investigated. To accomplish this, the solvent was varied between four different polyol solvents, EG and three different molecular weights of PEG: PEG 200; PEG 300; and PEG 600. The method described in section 4.5.2 Methods, was followed; the only variable that was changed was the solvent. When the more viscous solvents (PEG 300 and PEG 600) were used the dropwise addition of silver nitrate/poly(vinyl pyrrolidone) (AgNO_3/PVP) solution took longer (between 45 min and 1.5 h), whereas the EG and PEG 200 took about 20 min – 30 min to add, but regardless of the time it took to add the AgNO_3/PVP solution, the reaction was heated and stirred for 1.5 h after the dropwise addition of the entire AgNO_3/PVP solution. After purification of the reaction products, samples were prepared for scanning electron microscope (SEM) imaging to determine the shapes and sizes of the NPs formed, as shown in Figure 4.1a-d. The EG samples showed predominantly long ($\sim 2 \mu\text{m}$), densely packed AgNWs (see Figure 4.1a), very similar to the images reported by Jiu *et al.* and Coskun *et al.* [79, 84]. However, when the samples were greatly magnified (Figure 4.1a, inset), NRs, nanocubes, nanotriangles, and nanospheres were observed, but to a lesser extent than the NWs. These NRs, nanocubes, nanotriangles, and nanospheres were of similar size to those that were formed with PEG, but had minimal aggregation. Seerat Aziz assisted with performing the syntheses using PEG shown in Fig 4.1b-d. When using PEG of any molecular weight, nanospheres were the predominant product; however, clustering of the nanospheres increased as the molecular weight, and viscosity, of the solvent increased (Figure 4.1b-d). Using PEG 200, NRs, nanotriangles, and nanocubes were formed to a lesser extent, and remained

discrete (Figure 4.1b). With PEG 300 and PEG 600, there were far fewer NRs, nanotriangles, and nanocubes compared to the PEG 200 synthesis. The observation of coalescence (which increased with increasing molecular weight of solvent) indicates that the capping agents did not play an effective role.

Figure 4.1 also shows photographs of the reaction products after 1.5 h of heating. All the solutions were opaque, regardless of the solvent used. When using EG (Figure 4.1e) the solution was grey. PEG 200 resulted in a brown solution (Figure 4.1f), PEG 300 resulted in a yellow solution (Figure 4.1g), and PEG 600 resulted in a lighter yellow solution (Figure 4.1h). The different colors of the reaction products indicate that there are different morphologies of the nanoparticles present, as was confirmed using SEM, since different morphologies scatter light in different ways, resulting in different observable colors.

The extinction spectra shown in Figure 4.1i indicate that there is a difference in the structures synthesized; however the extinction spectra alone do not clearly predict the shapes of the structures synthesized due to the broad distributions of NPs formed in each synthesis. Furthermore, the larger NPs contain multipolar LSPRs as well as dipolar resonances that contribute to the broad absorption in the extinction spectra. Table 4.2 summarizes the yields obtained, after purification, from each of these syntheses (i.e., corresponding to the SEM images in Figure 4.1a-d). In this paper, NPs are particles of any shape, with at least one dimension on the nanoscale (usually under ~ 300 nm in dimension). Nanospheres are spherical shaped particles, with a diameter under ~ 300 nm. NWs are longer NPs, with their width on the nanometer scale, but lengths of several micrometers. Anisotropic, cylindrical NPs with lengths less than $1 \mu\text{m}$ are defined as

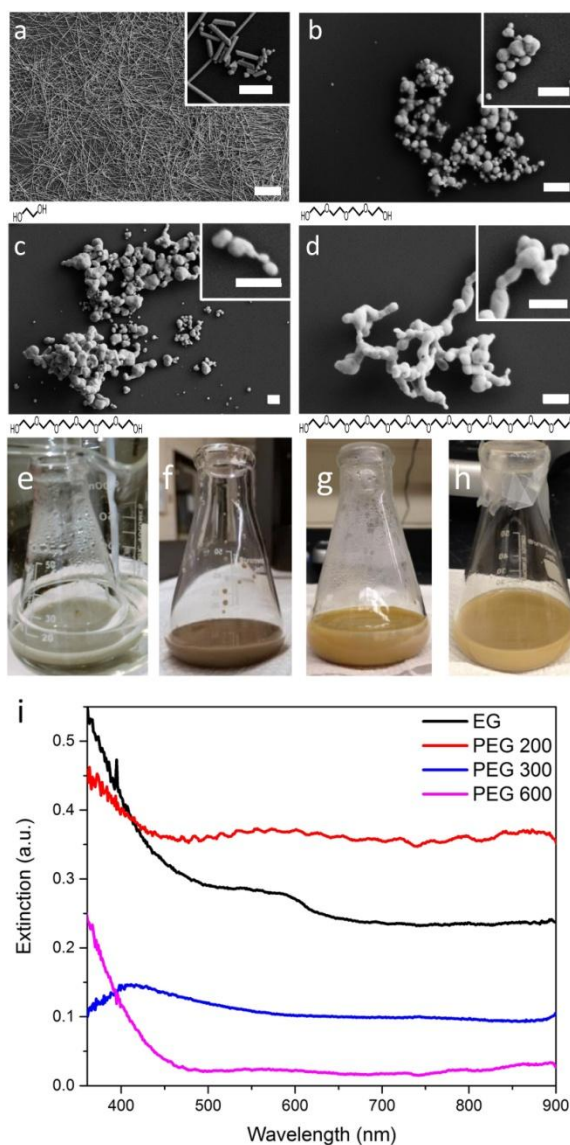


Figure 4.1. SEM images and photographs of the reaction product for each reaction with chemical structures of the solvent underneath. (a and e) Reaction using EG as the solvent. (b and f) Reaction using PEG 200 as the solvent. (c and g) Reaction using PEG 300 as the solvent. (d and h) Reaction using PEG 600 as the solvent. Insets of (a, b, c, and d) are magnified images of the reaction product. (i) UV-visible extinction spectra for the reaction products shown in (e-h); black line is EG, red line is PEG 200, blue line is PEG 300, and pink line is PEG 600. Scale bars: (a) is 10 μm ; (a inset and c) are 1 μm ; (b and d) are 500 nm; and (b inset, c inset, and d inset) are 200 nm.

NRs, and anisotropic, cylindrical NPs with lengths greater than or equal to 1 μm are defined as NWs in this paper. Nanohexagons are six sided NPs and nanotriangles are

three sided NPs, each with a height under ~ 300 nm. Other NPs are irregularly shaped NPs, or NPs that were regularly shaped but did not fit in the other categories (e.g. nanosquares) with a dimension under ~ 300 nm.

The EG synthesis resulted in a yield of ~ 33 % nanospheres, ~ 33 % anisotropic NRs and NWs, and ~ 33 % other shapes (nanotriangles, nanosquares, etc.). The 100 nm – 150 nm NPs (nanospheres, width of the NRs, width of the NWs, and some of the other NPs) are expected to exhibit a peak at ~ 400 nm UV-visible extinction spectrum [61, 106], as is present in Figure 4.1i. The longer NPs (length of the NRs and NWs, and larger other NPs) would contribute to longer extinction wavelengths, as is present with the shoulder in the spectrum in Figure 4.1i. Both the PEG 200 synthesis and the PEG 600 synthesis resulted in a yield of mainly nanospheres; however, there was a large distribution of sizes of those nanospheres, and the few other particles formed (NRs and other) were of a larger size range, in each case. Although the ~ 150 nm nanospheres are expected to exhibit an extinction peak around 400 nm, the other distribution of NPs may cause the shoulder observed in the extinction spectrum. The PEG 300 synthesis exhibited a narrower size distribution, which may be why the extinction spectrum exhibited a stronger peak at ~ 400 nm, and a less broad shoulder, extending only to ~ 550 nm. Some of the spectra have appreciable extinction values across the entire wavelength range, which suggests that the samples have appreciable scattering across the entire wavelength range, indicating that the samples are opaque, as observed in the reaction photographs (Figure 4.1e-h). Contradictory to what Park *et al.* reported, when using more viscous solvents the size of the nanoparticles generally did not change [101]. The PEG 300 synthesis did result in smaller nanoparticles; however, when using PEG 600, there was an

increase in nanoparticle size. Where Park *et al.* noticed a correlation between viscosity and particle size when using similar molecular weight diols [101], when using a wider range of molecular weight polyols, there was no correlation between viscosity and NP size.

Table 4.2. Summary of the yield of syntheses using different solvents.

Solvent	Shape	% Yield	Width (nm)	Length (nm)	Aspect Ratio
EG	Sphere	32.85	144 ± 66	-	-
	Rod	12.54	100 ± 50	516 ± 245	6 ± 4
	Wire	18.67	121 ± 59	2766 ± 2314	28 ± 30
	Other	35.94	191 ± 82	-	-
PEG 200	Sphere	96.15	158 ± 89	-	-
	Rod	0.26	266 ± 110	460 ± 265	2 ± 0.5
	Wire	0.00	-	-	-
	Other	3.59	163 ± 85	-	-
PEG 300	Sphere	80.79	69 ± 24	-	-
	Rod	14.47	67 ± 13	136 ± 34	2 ± 0.6
	Wire	0.00	-	-	-
	Other	5.13	84 ± 24	-	-
PEG 600	Sphere	98.78	211 ± 159	-	-
	Rod	0.54	125 ± 58	299 ± 46	3 ± 1
	Wire	0.00	-	-	-
	Other	0.68	365 ± 93	-	-

As reported by Abdel-Motaleb *et al.*, the increased molecular weight of PEG is expected to increase its ability to act as a capping or protecting agent [104]. This might explain why NWs were unable to be synthesized using any molecular weight of PEG under the same conditions. Having a larger percentage of capping agent with a weaker reducing agent in the solution should slow the growth of the NPs since there is a greater likelihood that the forming NPs come in contact with a capping agent (either PVP or PEG of higher molecular weight) than a source of Ag. The PVP capping agent is proposed to prevent the nanoparticle from growing along certain crystallographic directions [75-77, 79-81, 84, 107], but there have not been reports as to whether the PEG capping agent

would act in the same manner (capping certain crystallographic directions) or differently (capping all facets evenly). Since there are reports that the chain length of the polymer, in the case of PVP, changes which facet is capped [107], it is likely that PEG acts in a similar manner, although there are no such reports investigating this property. If PEG acts as a milder reducing agent, and a stronger capping agent with increased polymerization, it might explain why there is an increase of clustering with increasing molecular weight of the polyol, but more research would need to be done to verify this claim.

This change in the solvent's reducing and capping abilities indicates that more variables need to be changed when changing the solvent (e.g., temperature, time of the reaction, amount of chloride ions, molar ratio of PVP:AgNO₃) in order to obtain discrete nanoparticles, as further supported by the published reports using PEG, which all used different methods to obtain different results [38, 73, 77, 82]. Since none of the PEG trials resulted in significant quantities of anisotropic AgNPs, we focused on one PEG molecular weight for simplicity and compared it with EG. We chose to investigate PEG 300 and EG in particular, since the EG synthesis showed anisotropic growth but lacked controllability in the aspect ratio, and PEG 300's randomness of the clustering of nanoparticles limits the particle's usefulness for plasmonic applications; to be able to form more discrete particles would be extremely useful.

4.3.2 Solvent: Ethylene Glycol

The EG syntheses were carried out altering one variable at a time. Reaction time was investigated initially. To accomplish this, an aliquot of the reaction mixture was removed and purified immediately after all 6 mL of the AgNO₃/PVP solution was added.

After analyzing this sample (Figure 4.2a) it was found that the reaction product was similar in yield to the reaction that was heated for an additional 1.5 h (Figure 4.1a inset). This indicated that the NW growth occurs early in the reaction, while the AgNO_3/PVP solution is being added. Figure 4.2a shows the SEM image of the aliquot that was removed and purified. Figure 4.2e shows a photograph of the reaction immediately after the addition of the AgNO_3/PVP solution, which was a visibly greener and less opaque solution. This indicates that, for the EG synthesis, the reaction time does not play a key role in controlling the growth of NWs, beyond 30 min.

The next variable investigated was the effect of chloride ions, while keeping the other conditions the same. It has been reported that a chloride ion source is required for anisotropic growth; however those reports do not explain why this chloride ion source is required [79, 84]. Without a chloride ion source, no NWs were synthesized, as shown in Figure 4.2b. A photograph of the reaction product without the chloride ion source is shown in Figure 4.2f, showing a similar grey opaque solution to the reaction with chloride ions present. This indicates that a chloride ion source is, indeed, necessary for anisotropic AgNP growth, when using EG as the solvent; however, the color of the solution is less indicative of the reaction product. If one were to go by color alone, one would assume, incorrectly, that the mixture contained NWs. This highlights the importance of using multiple methods to verify the NP morphology.

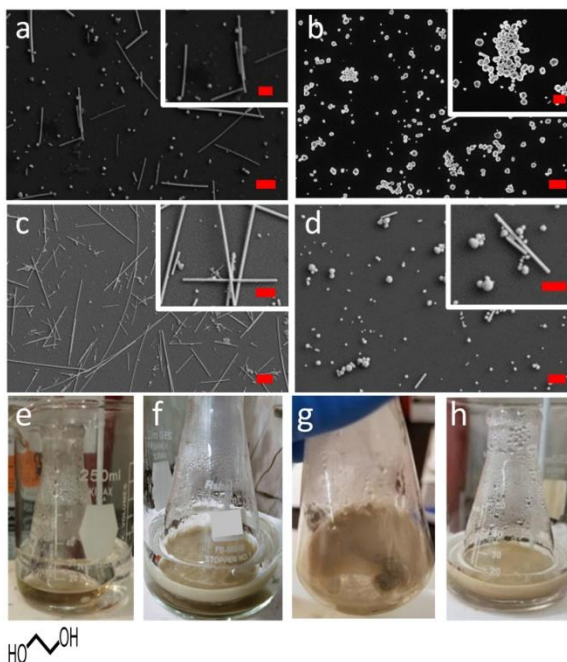


Figure 4.2. SEM images and reaction photographs of the reaction products for EG syntheses with one variable changed at a time with chemical structure of the solvent underneath. (a and e) EG synthesis that was purified immediately after the reagents were added. (b and f) EG synthesis without a source of chloride ions added. (c and g) EG synthesis with a PVP weight percent increased by a factor of three. (d and h) EG synthesis with a PVP weight percent increased by a factor of six. Insets of (a-d) are magnified images of the reaction products. Scale bars: (a, b, and c inset) are 1 μm ; (c) is 3 μm ; and (d, a inset, b inset, c inset, and d inset) is 500 nm.

The final variable that was investigated was the PVP weight percent. Using the initial synthesis conditions (with a chloride ion source) but increasing the PVP weight percent, first, by a factor of three, and, second, by a factor of six. When the PVP weight percent was increased by a factor of three (Figure 4.2c) the reaction product was similar to that obtained without altering any variables (Figure 4.1a); a SEM image is shown in Figure 4.2c, and a photograph of the reaction product is shown in Figure 4.2g. However, when the PVP weight percent was further increased to a factor of six greater than the starting weight percent, long NWs were no longer present in the reaction product, as

shown in the SEM image in Figure 4.2d (a photograph of the reaction product is shown in Figure 4.2h). The reaction product was composed largely of nanospheres and, to a lesser extent (~ 15 %), NRs. This indicates that increasing the amount of capping agent in the reaction will limit the elongation of the NWs, and, thus, provides some controllability in the anisotropic growth of the AgNPs.

Figure A3.1, in Appendix 3, shows the UV-visible extinction spectra for the purified reactions corresponding to Figure 4.2a-d. Due to the broad range of sizes of NPs in each of the EG syntheses broad extinction was observed for each synthesis. The trial without an FeCl₃ source exhibited a strong peak around 450 nm, which is attributed to the greater yield of shorter particles, and lack of NWs formed when not including an FeCl₃ source in the synthesis.

4.3.3 Solvent: Poly(Ethylene Glycol) 300

The reported methods for more viscous polyol solvents had very different procedures than the EG synthesis [73, 77, 79, 82-84]. To determine if discrete NPs could be synthesized using the more viscous, higher molecular weight polyol solvent, various syntheses using PEG 300 were investigated. The methods utilizing PEG reported in the literature had a wide range of reaction temperatures, so this was the first variable to be investigated. First, the reaction was heated in stages, starting at 50 °C, increasing to 75 °C and then to 100 °C. In addition to the change in temperature, the reaction proceeded for a longer period of time, 8 h. Also, the PVP:AgNO₃ ratio was varied from that which was used in the EG synthesis. All of these changes were made to better align with the procedures reported for PEG syntheses [73, 77, 82, 83].

The procedure for this heating-in-stages method is listed in Methods, Section 4.5.3.1. The silver particles synthesized using this method were different from the previous method (Figure 4.1c), in that discrete spheres were exclusively formed, as shown in the SEM image in Figure 4.3a. However, the reaction product had again turned a grey, opaque color, as shown in Figure 4.3e. When the time and temperature were both varied (Figure 4.3a), anisotropic NPs were not synthesized, but the clustering that was previously observed in the initial PEG 300 synthesis (Figure 4.1c) was also not observed. Since changing two variables resulted in an improvement in the NP synthesis, it was hypothesized that more variables would need to be altered at once in order to achieve discrete, anisotropic AgNPs.

The next variable investigated was the role of increasing the PVP weight percent. Besides the PVP weight percent increase (by a factor of three), the temperature was changed to 90 °C, for a longer time period, 7 h (a more detailed procedure is in Methods, Section 4.5.3.2). Seerat Aziz assisted in performing the syntheses shown in Figure 4.3 b-d. When the PVP weight percent was increased by a factor of about three to 0.41 M, the reaction product was mostly spheres; however, ~ 10 % of the product was NRs, as shown in Figure 4.3b. The reaction color was an opaque pink/grey, see Figure 4.3f. Next, the PVP weight percent was increased further, by a factor of about six greater than the starting concentration to 0.79 M, while keeping the other variables the same as the 0.41 M synthesis. This further increase in the PVP weight percent resulted in more NRs forming, ~ 15 % (see Figure 4.3c), which is a notable increase when compared to the original method that only resulted in spherical clusters; however, a yield of ~ 15 % NRs is by no means “high yield”. The reaction product was brown in color, see Figure 4.3g.

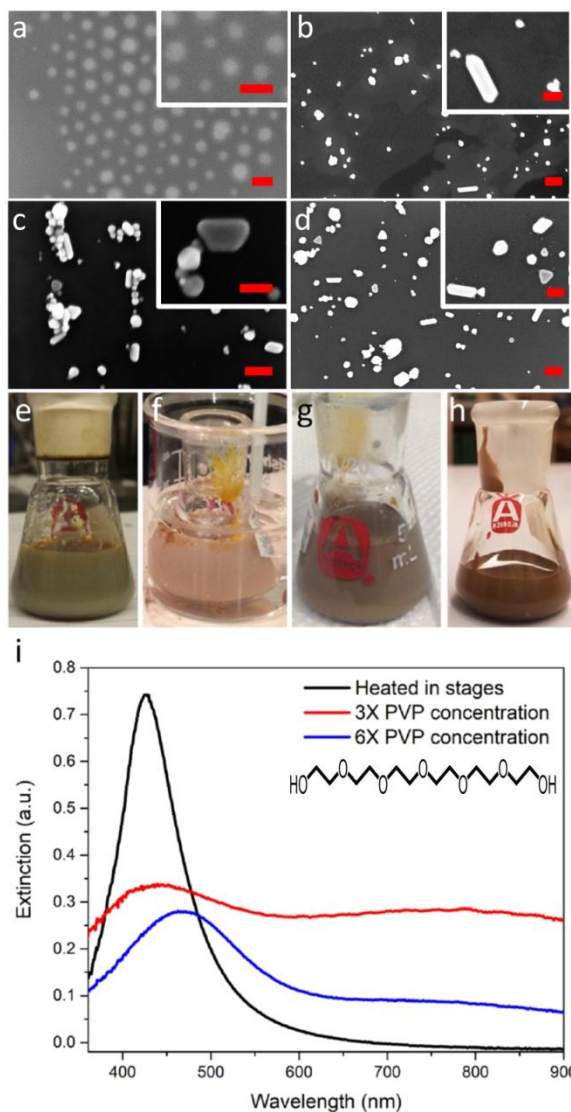


Figure 4.3. SEM images and photographs of the reaction products for PEG 300 syntheses with multiple variables altered between syntheses. (a and e) Heated in stages from 50 °C to 100 °C (0.1087 g PVP in 5 mL PEG 300, 0.0096 g AgNO₃ in 50 μL H₂O) reaction time 8 hr. (b and f) ~ 3:1 PVP:AgNO₃ ratio (0.3169 g PVP in 1 mL PEG 300, 0.1024 g AgNO₃ in 1 mL H₂O) heated at 90 °C for 7 h. (c and g) ~ 6:1 PVP:AgNO₃ ratio (0.6170 g PVP in 1 mL PEG 300, 0.1021 g AgNO₃ in 1 mL H₂O) heated at 90 °C for 7 h. (d and h) With chloride ions (6 × 10⁻⁴ M FeCl₃ · 6 H₂O, 0.16 g of AgNO₃ and 0.07 g of PVP dissolved in 10 mL of PEG 300) heated at 150 °C for 2 h. Insets of (a–d) are magnified images of the reaction products. (i) UV-visible extinction spectra for the purified products shown in (a–d), with chemical structure of the solvent used; the black line is from the synthesis that was heated in stages, the red line is from a synthesis with the PVP weight percent of 0.41 M (3x increase), and the blue line is the PVP weight percent of 0.79 M (6x increase). Scale bars: (a, a inset, c inset, and d inset) is 100 nm; (b inset, c, and d) is 200 nm; and (b) is 500 nm.

Thus far, all of the PEG 300 syntheses performed while investigating the effect of multiple variable changes were carried out without a chloride ion source, since most of the reported PEG methods did not include one [73, 77, 82, 83]. Indeed, both nanospheres and anisotropic NRs were formed without a chloride source present, but due to the low yields of NRs, it was hypothesized that a source of chloride ions would increase the yield of NRs, since literature reports that a chloride ion source was required for anisotropic growth.[79, 84] Since the trial with PVP weight percent of 0.79 M resulted in the most NRs without chloride ions present, this ratio was chosen for the trial with a chloride source. When the chloride source was added (a detailed procedure is in Methods, Section 4.5.3.3) the yield of NRs decreased, and the nanospheres formed larger diameter particles (Figure 4.3d). The reaction color was also different when a chloride source was added, appearing a brown opaque color (Figure 4.3h). This suggested that, unlike in the EG synthesis, a chloride ion source is not necessary, and might even be detrimental, for anisotropic NP formation when using PEG, which is contradictory to what has been reported to date [79, 84].

Figure 4.3i shows the UV-visible extinction spectra for the purified reactions corresponding to Figure 4.2a-c. Not shown is the UV-visible extinction spectrum for the reaction with a chloride ion source. The sample when heated in stages exhibited one strong peak at about 425 nm in the extinction spectrum, which corresponds to the discrete, uniform spheres that were confirmed using SEM. In both of the syntheses with increased PVP weight percent there was still a strong peak observed in the extinction spectra, present between 425 nm to 475 nm; however, there was increased broad

extinction from 600 nm to 900 nm, due to the broad range and size of the NPs synthesized.

When running the heating-in-stages PEG 300 synthesis, initially it was observed that the color of the reaction changed multiple times before the solution was heated. Since these multiple color changes indicate that the solutions were scattering light differently, indicating morphological changes, a reaction without any heating was investigated next. To accomplish this, AgNO_3 and PVP were added to PEG 300, and allowed to react at room temperature (no stirring). The flask was sealed with a stopper; however, the flask was not evacuated before sealing, meaning air (and oxygen) was still present. An aliquot was removed after 5 min, and purified immediately. Another aliquot was removed after 10 min, and purified immediately, and yet another at 20 min, and purified immediately. The purified reaction products are shown in Figure 4.4a-c. The reaction had undergone color changes, from orange to red-orange to red, as shown in Figure 4.4d-f. It is important to note that these solutions began opaque (Figure 4.4d) but turned clear as time proceeded (Figure 4.4f). The reasoning behind this is still not fully understood, but may be due to an increase in absorption cross-section and a concomitant decrease in the scattering cross-section of the nanoparticles as the reaction time progresses.

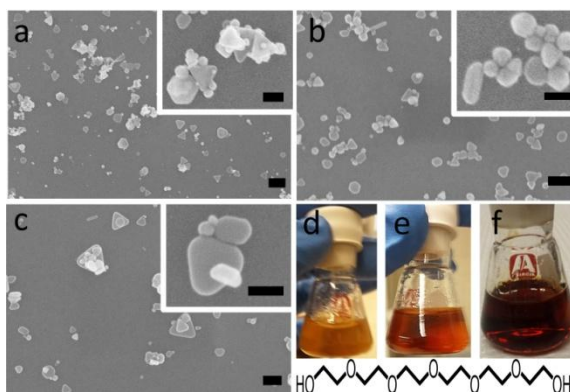


Figure 4.4. SEM images and photographs of the reaction products for PEG 300 syntheses carried out at room temperature, at certain times in the reaction; (a and d) after 5 minutes; (b and e) after 10 minutes; (c and f) after 20 minutes. Insets of (a, b, and c) are magnified images of the reaction products. Scale bars for (a) is 500 nm; (b, c, and a inset) are 200 nm; and (b inset and c inset) are 100 nm. The chemical structure of the solvent is included underneath the reaction photographs.

UV-visible extinction spectra are shown in Appendix Figure A3.2 for the reaction after various times had elapsed. The spectra for all three samples were similar broad peaks, this could be partially due to the samples being too optically dense and the spectrometer was saturated, or it could also partially indicate that there is a broad distribution of sizes of NPs, which was confirmed in the SEM images (Figure 4.4 a-c). Table 4.3 summarizes the yields obtained, after purification, from each of these syntheses (i.e., corresponding to the SEM images in Figure 4.4a-c). After 5 min had elapsed there was a high yield of small spheres (under 100 nm in width); however, about 30 % of the remaining NPs were large (greater than 150 nm in width) nanotriangles, nanohexagons, and other plate like NPs. After 10 min had elapsed the yield of nanospheres had decreased as did the average width of the nanospheres (under 50 nm). The yield of other shaped NPs had increased, and the yield of nanotriangles and nanohexagons remained about the same. Similarly to the nanospheres, the other nanoshapes formed were also

smaller in width (under 100 nm). After 20 min had elapsed the nanotriangle and nanohexagon yield remained about the same, as did the size, compared to the 10 min sample. The yield of NRs had increased slightly, as did the yield of nanospheres, but the size remained similar to the 10 min sample.

The average diameter of NP shapes decreased between 5 min and 10 min, but remained relatively constant between 10 and 20 min. It might be due to an initial clustering of seed particles, forming large NPs; however as time proceeds, the NPs form a smaller, more stable configuration. Alternatively it might be that, although there are still some larger nanoparticles present, there are a greater percentage of smaller NPs, which shifts the average diameter to a smaller value. The yield of the NP shapes had various different trends. The yield of some shapes, like the nanotriangles and nanohexagons, remained relatively constant regardless of reaction time. The yield of NRs slightly increased as the reaction time increased. The yield of nanospheres and other NPs exhibited the largest change, with nanospheres decreasing in yield as the reaction time increased, and other NPs increasing as time increased. Part of why there was the change in yield is that as one shape increases another must decrease, due to the fixed silver concentration. Why certain shapes remain relatively constant, while others change drastically, requires further investigation.

Table 4.3. Summary of the yield of syntheses using PEG 300 without heat.

<i>Reaction Time</i>	<i>Shape</i>	<i>% Yield</i>	<i>Width (nm)</i>	<i>Length (nm)</i>	<i>Aspect Ratio</i>
5 min	Triangle	20.95	185 ± 68	-	-
	Rod	1.50	62 ± 20	170 ± 32	2.9 ± 1.1
	Sphere	65.17	87 ± 37	-	-
	Hexagon	5.99	159 ± 68	-	-
	Other	6.39	158 ± 62	-	-
10 min	Triangle	20.30	83 ± 39	-	-
	Rod	1.64	48 ± 22	137 ± 52	3.1 ± 1.2
	Sphere	35.97	47 ± 18	-	-
	Hexagon	4.93	99 ± 60	-	-
	Other	37.16	76 ± 35	-	-
20 min	Triangle	23.36	88 ± 37	-	-
	Rod	7.79	41 ± 17	121 ± 47	3.4 ± 1.8
	Sphere	41.61	50 ± 20	-	-
	Hexagon	3.41	101 ± 35	-	-
	Other	23.84	84 ± 35	-	-

4.3.4 Mixed Solvents: Ethylene Glycol and Poly(Ethylene Glycol) 200

One final variable was investigated in an effort to better control the length of the nanowires formed. A mixture of two solvents, EG and PEG 200 of varying ratios was analyzed. The first ratio analyzed was a 50:50 mixture of EG:PEG 200. A detailed procedure is found in Methods, Section 4.5.3.4. A control synthesis of EG only was performed along with the mixed solvent trial to ensure that the results of the mixed ratio trial were valid, and not due to external factors that can effect NP synthesis (such as humidity, room temperature, degradation of reagents, etc.) Figure 4.5a shows SEM images from the EG control reaction. Figure 4.5c shows SEM images from the EG:PEG 200 reaction. Additionally, reaction photographs for the EG control reaction and the EG:PEG 200 reaction are shown in Figure 4.5b and d, respectively.

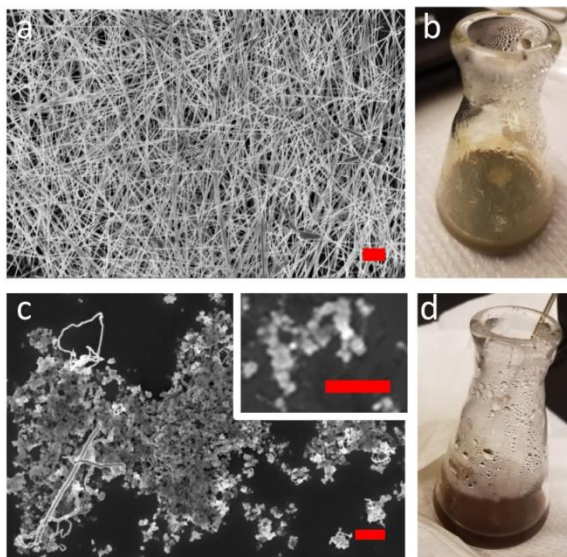


Figure 4.5. SEM images and photographs for the reaction product; (a, b) EG only reaction; (c, d) 50:50 EG:PEG 200 ratio reaction, with an inset of a magnified region. Scale bars for all SEM images are 1 μm .

The control reaction resulted in a large yield of NWs, which was expected for the EG synthesis. The 50:50 mixture of solvents EG:PEG 200 did produce some NWs; however, the majority of particles were spherical, and appear to be of similar diameters. There was some aggregation using the 50:50 ratio of solvents. Overall the mixed ratio of solvents does show some improvement over the PEG 200 only reaction. However, the tunability in size and shape of NPs is still not achievable, so, perhaps, a different ratio would provide greater tunability.

A 90:10 EG:PEG 200 reaction was also performed; however, the control in this experiment (EG only as the solvent) did not result in the usual NWs synthesis, instead forming a range of spherical NPs. Since the control reaction did not provide satisfactory results, external factors were likely at play, meaning that the 90:10 EG:PEG 200 reaction's results cannot be trusted as valid. Appendix A3.1 describes in detail the procedure for this 90:10 EG:PEG 200 reaction, and Appendix Figure A3.3 shows the

SEM images and reaction photographs for these reactions. An interesting observation during this reaction was that the color of the initial solution was a dark green/black color in appearance. This 90:10 EG:PEG 200 reaction should be repeated, with an EG only control to verify no external factors affect the reaction. If the initial color changes occur again, those should be analyzed in depth, since it is likely that there are morphological changes occurring early in the reaction, corresponding to the different ways that the different morphologies absorb and scatter light.

4.4 Conclusions

Here, we investigated the polyol method for silver nanoparticle synthesis utilizing different molecular weight solvents. We have demonstrated that the one-pot polyol process is a versatile method that can produce vastly different nanoparticles by changing a few synthesis parameters. Figure 4.6 summarizes reaction conditions and the role that the solvent plays in the morphology of the nanoparticles. When using ethylene glycol as the solvent, micrometer long nanowires were synthesized. When using poly(ethylene glycol) of any molecular weight, nanowires could not be synthesized. Instead, nanospheres were the dominant product, and the nanospheres that were synthesized exhibited increased coalescence with increasing molecular weight of the solvent. Additionally, we have identified other key variables that can be used to tune the morphology of the nanoparticles, specifically the ratio of PVP to AgNO_3 , and the reaction time and temperature. We also found that the chloride ion source is important for some polyol solvents, but not for others. The last variable that was studied was a mixed solvent reaction. Using a mixture of solvents did improve the yield of discrete

nanoparticles, when compared to the reaction using only the higher molecular weight solvent from the ratio. Additional ratios need to be investigated. This initial comparison between polyol synthesis methods using ethylene glycol and poly(ethylene glycol) demonstrates the important role of polyol molecular weight in determining the nanostructure shape and yield. More detailed studies are needed to fully understand the mechanism of the polyol method for silver nanoparticle synthesis when high molecular weight polyols are employed.

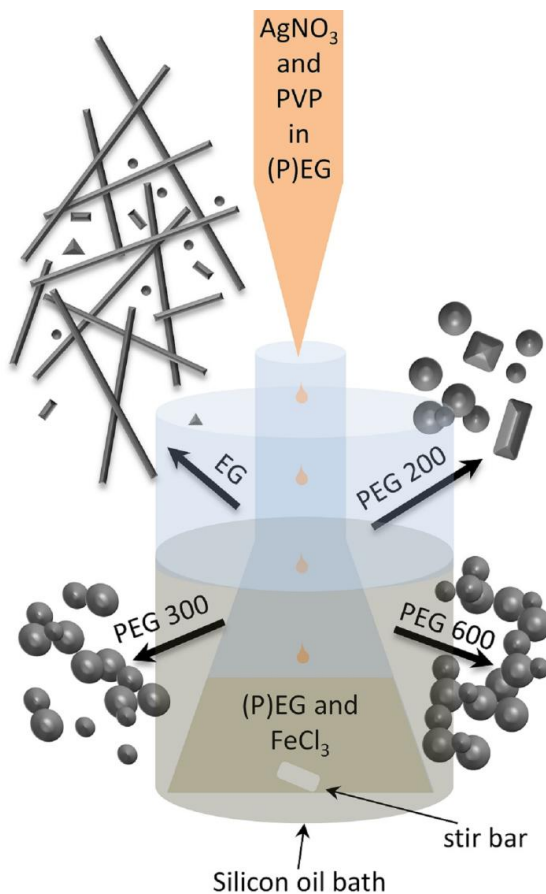


Figure 4.6. Schematic diagram summarizing synthesis setup, variables, and the corresponding silver nanoparticle products. Silver nitrate and polyvinylpyrrolidone were first dissolved in the polyol solvent, either EG, PEG 200, PEG 300, or PEG 600, and added dropwise to the flask from a burette, that contained the same polyol solvent as well as a source of chloride ions, in the form of iron chloride. The reaction was stirred the entire time. By varying the solvent the reaction product can be varied as shown by the arrows leading to the predominant reaction products for each solvent.

4.5 Materials and Methods

4.5.1 Materials

EG (anhydrous 99.8%), PEG 200, PEG 300, PEG 600 (bioUltra), AgNO₃ (ACS reagent >99.0%), PVP (average molecular weight of 40,000 g/mol), hydrogen peroxide solution (contains inhibitor 30 wt. % in H₂O), and sulfuric acid (ACS reagent grade) were

purchased from Sigma Aldrich. Iron chloride hexahydrate ($\text{FeCl}_3 \cdot 6\text{H}_2\text{O}$) (reagent grade), acetone (certified ACS), and ammonium hydroxide (certified ACS plus) were purchased from Fisher Scientific. 190 proof ethanol (meets United States Pharmacopeia specifications) was purchased from Decon Labs. All chemicals were used without further purification.

4.5.2 Methods

In a typical synthesis, first, an oil bath was preheated to 150 °C. Meanwhile, 6 mL of the solvent, (P)EG, 0.5 mL of a 6×10^{-4} M $\text{FeCl}_3 \cdot 6\text{H}_2\text{O}$ solution, and a Teflon-coated, 2 mm x 5 mm, micro stir bar were added to an Erlenmeyer flask. The flask was then placed in the preheated oil bath with stirring set to 1000 rpm, and heated for 30 min. to ensure even heating in the flask. Meanwhile, a stock solution of PVP (0.065 M) and AgNO_3 (0.096 M) combined together in the same polyol solvent being used (either PEG or EG) was prepared. After the 30 min of heating the flask, 6 mL of the AgNO_3 /PVP stock solution was added dropwise to the flask at a rate of ~ 0.3 mL/min, using a burette. After all 6 mL were added, the solution was heated and stirred for another 1.5 hours, after which the flask was removed from the oil bath, and the reaction product was purified by centrifugation as follows. Approximately 1 mL of the reaction product was removed from the Erlenmeyer flask, and placed in a 15 mL centrifuge tube and diluted with 4 mL of acetone and 4 mL of ethanol, shaken vigorously, then sonicated for about 20 s to disperse. The solution was then centrifuged (using a VWR clinical 50 centrifuge) at 1900 g's for 10 min. The supernatant was then removed and replaced with another 4 mL of acetone and 4 mL of ethanol, shaken and sonicated, and centrifuged again under the same

conditions. The supernatant was removed once more, and 2 mL of ethanol was added as a final solvent, shaken and sonicated as before to disperse. Modifications of the aforementioned synthesis were made as discussed below, in section 4.5.3 Modifications, to assess the impact of variables on the shape/size of the silver nanoparticles. The main variables investigated were: molecular weight of the polyol, temperature, and PVP:AgNO₃ ratio. The specific details of the modified syntheses are specified at the relevant point in the chapter (Sections 4.3.1, 4.3.2, 4.3.3). Samples were prepared for scanning electron microscopy (SEM) analysis (performed using a Zeiss Sigma Field Emission SEM) by drop depositing 20 μ L of the purified sample on silicon wafers that were cleaned by following the procedure reported by Stockton *et al.* [96]. A brief outline of the cleaning procedure is as follows: immersion in a sulfuric acid/hydrogen peroxide bath; three deionized water rinses; immersion in an ammonium hydroxide/hydrogen peroxide bath; followed by three deionized water rinses; and, finally, an ethanol rinse [96]. UV-visible extinction spectroscopy (performed using an Ocean Optics FHSA-TTL sample holder and SiPhotonics CCD array UV-visible spectrometer) was utilized to monitor the reaction products, with a quartz cuvette (1 cm path length) used as the holder.

4.5.3 Modifications to the Synthesis Procedure

4.5.3.1 PEG 300 Heating in Stages Procedure

This procedure was based off of the procedure reported by Liang *et al.* using PEG 300 instead of PEG 600, and scaled down from the reported procedure [77]. 0.11 g of poly(vinyl pyrrolidone) (PVP) was dissolved in 1 mL of deionized water (MilliQ, 18 Ω resistance). This PVP solution was then mixed with 5 mL of PEG 300. 0.017 g of

AgNO₃ was weighed and dissolved in 0.1 mL of deionized water (MilliQ, 18 Ω resistance). The AgNO₃ solution was added to the PVP/PEG300 solution. The combined solution was then placed in an oil bath, a Teflon coated micro stir bar was added to the solution, stirring was set at 1000 rpm. The hot plate was set heat to 50 °C for ~ 1 hr, with the temperature increasing from room temperature to 50 °C over ~ 15 min. After ~ 1 hr, the temperature was increased to 75 °C, and remained at 75 °C for 2 more hrs. Then the temperature was increased to 100 °C, and remained at 100 °C for 40 more minutes. The reaction product was then removed, and an aliquot was placed in a centrifuge tube. The sample was centrifuged at 10,000 g's for 20 min, and then at 15,000 g's for 20 min. The supernatant was removed and the precipitate was washed with 1 mL of acetone and 1 mL of ethanol, then sonicated for ~ 30 s to disperse. The sample was then centrifuged for 20 min at 15,000 g's. The supernatant was removed again, and the precipitate was washed with 2 mL of ethanol, only, and sonicated for 30 s to disperse. The solution was centrifuged for 20 min at 15,000 g's again. The supernatant was removed again, and the precipitate was washed with 2 mL of ethanol, and dispersed by sonication for 30 s.

4.5.3.2 PEG 300 Increased Molar Ratio of PVP:AgNO₃ Procedure

This procedure was based off of the report and following correspondence with Dong, *et al.* but using PEG 300 instead of PEG 600 [105]. First, 5 mL of PEG 300 was preheated at 90 °C for 30 min in an oil bath, a Teflon coated micro stir bar was added to the PEG 300, and stirring was set at 1200 rpm. A PVP solution was prepared by combining 0.32 g of PVP with 1 mL of PEG 300, for the three times increased PVP

weight percent trial, or 0.62 g of PVP with 1 mL of PEG 300 for the six times increased PVP weight percent trial. A AgNO_3 solution was prepared by combining 0.10 g of AgNO_3 with 1 mL of deionized water (MilliQ, 18 Ω resistance). The AgNO_3 solution was sonicated for 10 min to dissolve. The PEG/PVP solution was added rapidly to the preheated PEG 300. The AgNO_3 solution was added dropwise over a period of 10 min. The reaction was heated for 7 hr, after which 0.1 mL of the reaction product was extracted and diluted with 1.9 mL of ethanol, then sonicated for 10 min. The reaction product and diluted reaction product were placed in the refrigerator until the sample could be centrifuged. When the vial was removed from the refrigerator the vial was sonicated again for 20 min. The vial was then centrifuged for 15 min at 10,000 g's. The supernatant was removed, and another 1.9 mL of ethanol was added to wash the precipitate, and sonicated for 10 min. The sample was centrifuged again, for 15 min at 10,000 g's. The supernatant was removed, and another 1.9 mL of ethanol was added to wash the precipitate, and sonicated for 10 min.

4.5.3.3 PEG 300 with FeCl_3 Source Procedure

This procedure was again based off of the report and correspondence with Dong *et al.* [105]. A stock solution of 6×10^{-4} M $\text{FeCl}_3 \cdot 6\text{H}_2\text{O}$ in PEG 300 was prepared by dissolving 0.016 g of $\text{FeCl}_3 \cdot 6\text{H}_2\text{O}$ in 100 mL of PEG 300. A PVP solution was prepared by combining 0.62 g of PVP with 1 mL of PEG 300. A AgNO_3 solution was prepared by combining 0.10 g of AgNO_3 with 1 mL of deionized water (MilliQ, 18 Ω resistance). The AgNO_3 solution was sonicated for 10 min to dissolve. The PEG/PVP solution was added rapidly to the preheated PEG 300. The AgNO_3 solution was added dropwise over a period

of 10 min. The reaction was heated for 7 hr, after which 0.1 mL of the reaction product was extracted and diluted with 1.9 mL of ethanol, then sonicated for 10 min. The reaction product and diluted reaction product were placed in the refrigerator until the sample could be centrifuged. When the vial was removed from the refrigerator the vial was sonicated again for 20 min. The vial was then centrifuged for 15 min at 10,000 g's. The supernatant was removed, and another 1.9 mL of ethanol was added to wash the precipitate, and sonicated for 10 min. The sample was centrifuged again, for 15 min at 10,000 g's. The supernatant was removed, and another 1.9 mL of ethanol was added to wash the precipitate, and sonicated for 10 min.

4.5.3.4 50:50 EG:PEG 200 Ratio Procedure

The mixed EG:PEG 200 procedure closely follows the typical procedure described in the methods section 4.5.2, the main difference was the ratio of the solvent used.

First, an oil bath was preheated to 150 °C. Meanwhile, 3 mL of the EG, 3 mL of PEG 200, 0.5 mL of a 6×10^{-4} M $\text{FeCl}_3 \cdot 6\text{H}_2\text{O}$ in EG, and a Teflon-coated, 2 mm x 5 mm, micro stir bar were added to an Erlenmeyer flask. The flask was then placed in the preheated oil bath with stirring set to 1000 rpm, and heated for 30 min., to ensure even heating in the flask. Meanwhile, a stock solution of PVP (0.065 M) and AgNO_3 (0.096 M) combined together in a 50:50 mixture of the two solvents being used (EG and PEG 200) was prepared. After the 30 min of heating the flask, 6 mL of the AgNO_3 /PVP stock solution was added dropwise to the flask at a rate of ~ 0.3 mL/min, using a burette. After all 6 mL were added, the solution was heated and stirred for another 1.5 hours, after

which the flask was removed from the oil bath, and the reaction product was purified by centrifugation as follows. Approximately 1 mL of the reaction product was removed from the Erlenmeyer flask, and placed in a 15 mL centrifuge tube and diluted with 4 mL of acetone and 4 mL of ethanol, shaken vigorously, then sonicated for about 20 s to disperse. The solution was then centrifuged (using a VWR clinical 50 centrifuge) at 1900 g's for 10 min. The supernatant was then removed and replaced with another 4 mL of acetone and 4 mL of ethanol, shaken and sonicated, and centrifuged again under the same conditions. The supernatant was removed once more, and 2 mL of ethanol was added as a final solvent, shaken and sonicated as before to disperse.

Chapter 5. Summary, Conclusions, and Future Directions

5.1 Summary and Conclusions

The overall objective of this thesis was to better understand the interactions between surface plasmons from silver nanoparticles and ultra-thin polymeric films. Stimulated emission of surface plasmons when coated with an ultra-thin polymeric film was investigated in Chapter 2. Chapter 3 demonstrated that surface plasmons and excitons from the ultra-thin polymeric films/silver nanoparticle composites could couple, resulting in hybrid states forming, which enhanced the emission of the polymer. The synthesis of anisotropic silver nanoparticles was investigated in Chapter 4, in an effort to synthesize silver nanorods, which could be utilized for dual regime plasmon/polymer interactions (i.e. observing stimulated emission and plasmon-exciton coupling in the same system), or to improve the efficiency or coupling strength of the plasmon-polymer interactions..

Blue-emitting spasers utilizing 60-nm silver nanoparticles and ultra-thin (~ 30 nm – 70 nm) PFO films were demonstrated in Chapter 2. Stimulated emission at wavelengths between 444.8 nm – 449.4 nm, spectral collapse, non-linear emission peak intensity verses excitation energy density, and thresholds ranging from 2 mJ/cm^2 – 8 mJ/cm^2 was observed. All of these observations lead to the conclusion that lasing-spasing is occurring. This conclusion was further strengthened by the lack of observing these characteristics in the PFO films without nanoparticles, or in the silver nanoparticle layers without PFO films. The observation of lasing-spasing was limited to PFO films at least 30 nm thick, since below this thickness (which corresponds to half the diameter of the nanoparticle) there is a lack of physical coverage between the nanoparticle and polymer film, thus the interaction between surface plasmons and excitons is not optimized. The

threshold for lasing-spasing decreased with increasing film thickness, which further supports that the physical coverage is important for lasing-spasing. This was the first demonstration of blue emitting lasing-spasers, which is important to expand the active wavelength range of these devices. Furthermore, this was first demonstration with ultra-thin-films in an array configuration. The ultra-thin aspect would allow for further miniaturization of devices, expanding the potential applications for this emerging technology.

Chapter 3 investigated the coupling between plasmons and excitons in silver nanoparticle/ultra-thin F8BT polymer films, using two different configurations of silver nanoparticles. Enhancement in the polymer's emission was observed for both configurations, but was stronger for the single silver nanoparticle system. Since single nanoparticles were probed before and after coating with the ultra-thin polymer, and the enhancement was seen only at the areas where a single nanoparticle was, this enhancement is attributed to plasmon-exciton coupling. Further analysis demonstrated that the most pronounced enhancement of the dark field scattering spectra occurs at about 500 nm. This enhancement of the scattering spectra occurs at the absorption edge of the polymer, and thus the plasmon-exciton coupling is attributed to Absorption Induced Scattering, an intermediate regime of coupling.

The synthesis of silver nanoparticles using a green synthesis method, the polyol method, was demonstrated in Chapter 4. This method produced a range of nanoparticle shapes and sizes simply by changing one or two parameters. The synthesis of silver nanoparticles was very sensitive to the molecular weight of the polyol solvent. Micrometer long nanowires were obtained using ethylene glycol, while shorter spherical

nanoparticles, as well as other shapes (triangles, squares, hexagons) were obtained using poly(ethylene glycol). Additional variables beyond just the solvent were investigated. The variables that played a key role for one solvent, did not necessary aide in the synthesis of nanoparticles when using a different solvent (for example, a chloride ion source was necessary for ethylene glycol, but found to not have any effect for poly(ethylene glycol) 300). The reason that the solvent plays such a major role in the silver nanoparticle synthesis is that polyols act as both reducing agent and capping agent, the strength of which varies depending on molecular weight. This dual nature of the solvent might also be why changing other variables do not have similar effects.

In conclusion, this thesis sought to better understand the interactions between plasmons and excitons. Additionally, the constituent materials utilized were expanded, from the traditional gold and laser dye system to silver nanoparticles and conjugated polymers. This was done to both expand the emission wavelength range, as well as to theoretically improve the efficiency of the plasmonic materials. This thesis demonstrated a novel configuration of lasing-spasers, with the thinnest gain media layer, and bluest emission, for room temperature lasing-spasers. Previously, lasing-spaser and random laser demonstrations were only active below ~ 370 nm, or above ~ 470 nm, there was a lack of demonstrations in the blue region of the visible spectrum. Expanding the emission range of lasing-spasers is key for applying this emerging technology to different optics, spectroscopic, and biological applications. Additionally, this thesis demonstrated plasmon-exciton coupling in the intermediate regime at the single nanoparticle level for silver nanoparticle/ultra-thin polymer film composites. This, again, is a novel

configuration, and studies using such a thin exciton source had not previously been performed.

Finally, since silver nanoparticles play such an important role in the two novel demonstrations of this thesis, the synthesis of silver nanoparticles was investigated to determine if a more environmentally friendly synthesis method would result in a reproducible, high yield of anisotropic silver nanoparticles. Silver nanorods of tunable aspect ratio are important for improving the coupling strength and efficiency of the plasmon-polymer interactions, and could lead to dual regime applications. Since silver nanorods are unavailable for purchase commercially, a reproducible laboratory synthesis method must be used. An environmentally friendly method was desired since many of the applications for plasmonic nanoparticles (organic light emitting devices, organic solar cells, etc.) are based around sustainability, and greener methods and materials – it would be counterintuitive to use a non-environmentally friendly method for these applications. Further this investigation into the polyol method addressed key questions that are lacking in the literature. There were literature reports that involved utilizing different molecular weight polyols, however the procedures for these methods varied drastically, making it impossible to determine the effect that the solvent has on the synthesis, since it could have been a combination of variables which result in the change in nanoparticle shape or size. By systematically analyzing the effect of changing the solvent, as well as systematically analyzing additional variables, the effect of these isolated variables was determined, which had not been previously reported.

5.2 Future Directions

5.2.1 *Coherence and Polarization/Angle Dependence of Spasers*

Coherence, an important characteristic in lasers, is the ability emit monochromatic radiation and maintain a narrow, directional beam over large distances [108]. Although this is a key characteristic to proving that lasing is occurring, it is rarely reported or tested for in the current demonstrations of plasmonic nanolasers. Coherence measurements should be carried out for the array spasers that were demonstrated in Chapter 2, to verify that the spasers are truly a nanoscale laser. In order to test coherence of the array spasers, photoluminescence (PL) spectra should be obtained simultaneously in two orientations, normal to the film (which is how the PL spectra was obtained in Chapter 2), as well as from the edge of the film. The intensity of these spectra would need to be compared. Ideally, if the array spasers are coherent, the PL spectra would be intense normal to the surface, and limited (or none) PL spectra would be seen from the edge direction. However, as discussed in Chapter 2, collecting the edge emission could result in photonic modes and light trapping, as well as random lasing effects. Due to the potential for alternative modes of emission being observed from the edge of the sample, if there is intense PL spectra emitted from the edge of the sample further experiments would need to be performed to determine whether it is from light trapping or random lasing, or if the spasers are not coherent. A second order correlation function ($g^{(2)}$) should also be obtained to quantify the coherence [109]. This would be done using a PL lifetime setup, with a beam splitter sending the emission of the spasers to two photon multiplier tubes. The photon pair time intervals are then used to determine the $g^{(2)}$ correlation [109].

5.2.2 *Polyol Synthesis*

In Chapter 4 silver nanoparticles of many shapes and sizes were synthesized. The effect of changing the solvent, but using the same procedure was studied. This resulted in a reproducible synthesis of nanowires when using ethylene glycol as the solvent, but when switching to a higher molecular weight solvent, aggregation was observed. Because of the aggregation the effect of additional variables were studied. This led to some interesting results, such as the initial synthesis of various shapes using poly(ethylene glycol) 300 without heating (Chapter 4, Figure 4.4), as well as the synthesis with varying ratios of ethylene glycol:poly(ethylene glycol) 200 as the mixed solvent (Chapter 4, Figure 4.5 and Appendix 3, Figure A3.4). Further investigations should be performed, similar to the in depth study of poly(ethylene glycol) 300, to determine if similar results occur with poly(ethylene glycol) 600 or poly(ethylene glycol) 200. Additionally, the mixed solvent synthesis appears to be promising, so therefore, additional ratios mixed solvents should be analyzed. Some additional variables should also be investigated, such as the source of silver, the effect of seeding the reaction, and other sources of chloride ions, since these variables have been identified as important by some authors [57, 63, 110].

Additionally, alternative purification methods should be investigated. We did vary the centrifugation speed, (from 1900 g's to 19000 g's); however, this did not result in better separation. It might be useful to continue investigating other spin speeds in order to better separate the particles, and obtain higher yields of the desired silver nanorods by separation. Alternative separation techniques should also be investigated such as gradient separation techniques, or polymer encapsulation. Improvements to the separation could

result in better selectivity of which shape and size nanoparticle is obtained, and thus improve the yield of nanoparticles obtained.

5.2.3 *Life Cycle Assessment*

Part of why the polyol method was appealing as a synthesis method is that it is often touted as a greener synthesis method. However, there have been few reports that verify and quantify how much more environmentally friendly this method is. Performing a life cycle assessment of the polyol method, and comparing it to an alternative method, such as a sodium borohydride synthesis, would be prudent. A preliminary life cycle assessment was completed, and is shown in Appendix A4.1; however, a more complete life cycle assessment should be completed. This life cycle assessment was carried out with the assistance of Priyanka Dilip, Jessica Kuleshov, Kian Vilhauer, and Christopher Yoo, all of whom were students in the New Jersey - Governor's School of Engineering & Technology (NJ-GSET) program.

5.2.4 *Alternative Exciton Sources*

Chapter 3 demonstrated that plasmon-exciton coupling is observable at the single nanoparticle level using F8BT as the exciton source. Additional sources of both the exciton, and the plasmon should be investigated, to determine if the coupling strength changes when the constituents change. Some potential configurations to investigate would be CdS/ZnS core-shell quantum dots as the exciton source with 60 nm silver nanoparticles, since these materials have good spectral overlap between the absorption of the quantum dots and surface plasmon resonance of the 60 nm silver nanoparticles, and

the narrow emission of the quantum dots should theoretically provide for better coupling. Another potential configuration would be with PFO and 40 nm silver nanoparticles, again due to the good spectral overlap of the materials.

5.2.5 *Single Particle Spasers*

In Chapter 2 array spasers were investigated due to limitations in the experimental setup, at that time single particles were unable to be probed. However, as demonstrated in Chapter 3, the experimental setup was redesigned, so that single nanoparticles were able to be probed. Due to this advancement in the experimental setup, it would be interesting to investigate if a single nanoparticle can behave as a spaser. In order to fabricate the single nanoparticle spaser samples, the density of silver nanoparticles would need to be decreased, so that individual nanoparticles can be identified using the microscope setup. Additionally this less dense sample should eliminate the possibility of interparticle coupling. Analyzing single nanoparticle spasers would also help to validate, or nullify, some of the hypotheses about the array spasers, such as that interparticle coupling contributing to the quality factor. Preliminary investigations into this single nanoparticle spasers is described in Appendix A4.2.

Appendix

A.1. Appendix to Chapter 2

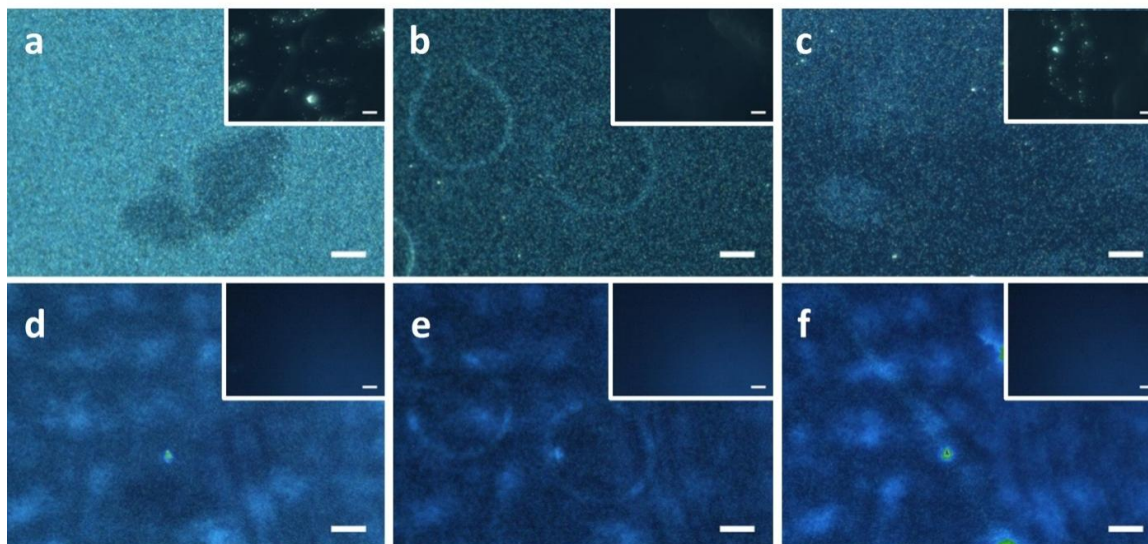


Figure A1.1. Optical images of AgNP density as well as coverage of PFO polymer film. (a-c) DF image of AgNPs with varying PFO film thicknesses of 50 nm, 47 nm and 30 nm, respectively. Insets are of neat PFO films with the corresponding thicknesses. (d-f) PL images, illuminated by a continuous-wave 405 nm laser diode, of AgNPs with varying PFO film thicknesses of 50 nm, 47 nm and 30 nm, respectively. Insets are of neat PFO films with the corresponding thickness. Scale bars are 10 μm .

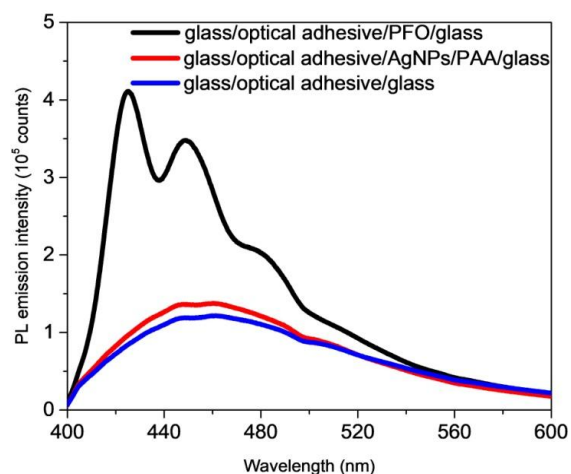


Figure A1.2. PL spectrum of glass/optical adhesive/glass compared to glass/optical adhesive/AgNPs/PAA/glass spectrum, as well as glass/optical adhesive/PFO/glass spectrum.

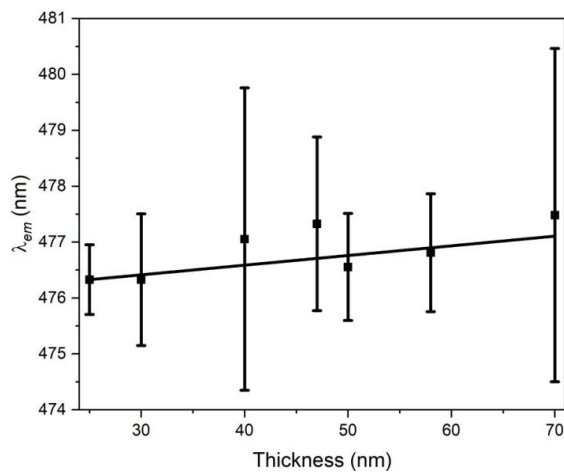


Figure A1.3. Trend of λ_{em} (0-2) versus t_{PFO} . 0-2 peak λ_{em} for PFO/AgNPs samples versus t_{PFO} , the λ_{em} was averaged for at least ten different spectra, at different regions of the sample, leading to potentially different AgNP local densities which cause the larger error in the data, and at a range of excitation energies, for each t_{PFO} . A linear trendline was fit to the data. Repetition rate ranged from 104-205 Hz.

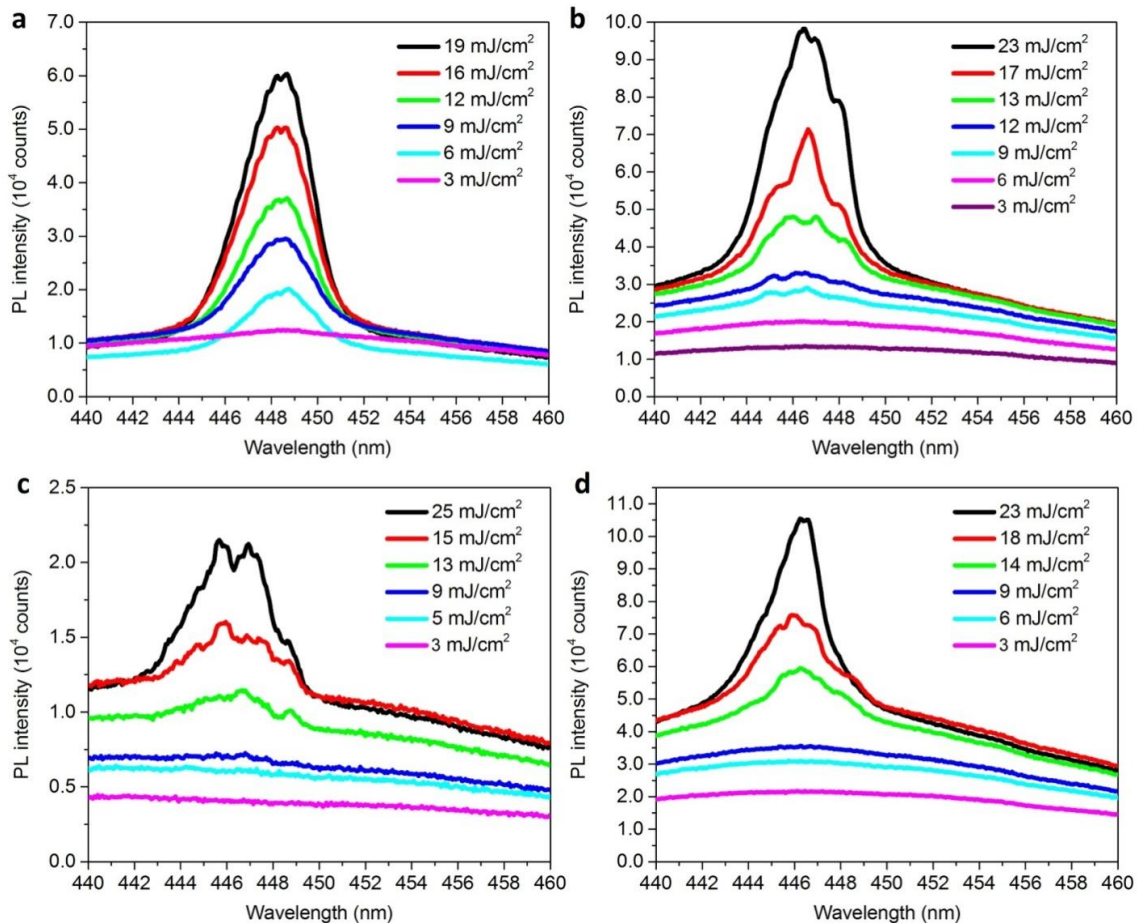


Figure A1.4. Variations observed in PL emission spectra for samples of varying PFO thickness and with an AgNP density of 24 ± 3 NPs/ μm^2 (i.e., glass/epoxy/PFO/AgNPs/PAA/glass). (a) 58 nm PFO (b) 50 nm PFO (c) 40 nm PFO (d) 30 nm PFO.

A1.1. Dependence of Stimulated Emission Spectra on the Region of the Sample Probed and on the Emission Area Collected

Since, the same sample could exhibit one or the other emission behaviors depending on measurement conditions, a systematic investigation of the measurement conditions was conducted whereby both the region of the sample being probed, as well as the emission area being collected by the spectrometer were investigated (Figure A1.5).

The excitation laser spot size on the sample remained constant at ~ 0.28 mm in diameter resulting in an emission area with similar diameter. When the sample was probed near the edge, multimode stimulated emission was observed, along with a slight variation in the PFO emission spectra, specifically the 0-1 emission peak blueshifted to ~ 440 nm and a shoulder formed at ~ 447 nm, (Figure A1.5), likely due to substrate waveguiding or scattering at the sample edge.[28, 30, 91] When the center of the sample was probed either single mode or multimode behavior was observed, depending on the emission area collected by the spectrometer. When almost all of the emission area was collected, multimode behavior was observed. When only the center of the emission area was collected by the spectrometer, single mode behavior was detected, whereas multimode behavior was observed when the edge of the emission area was analyzed.

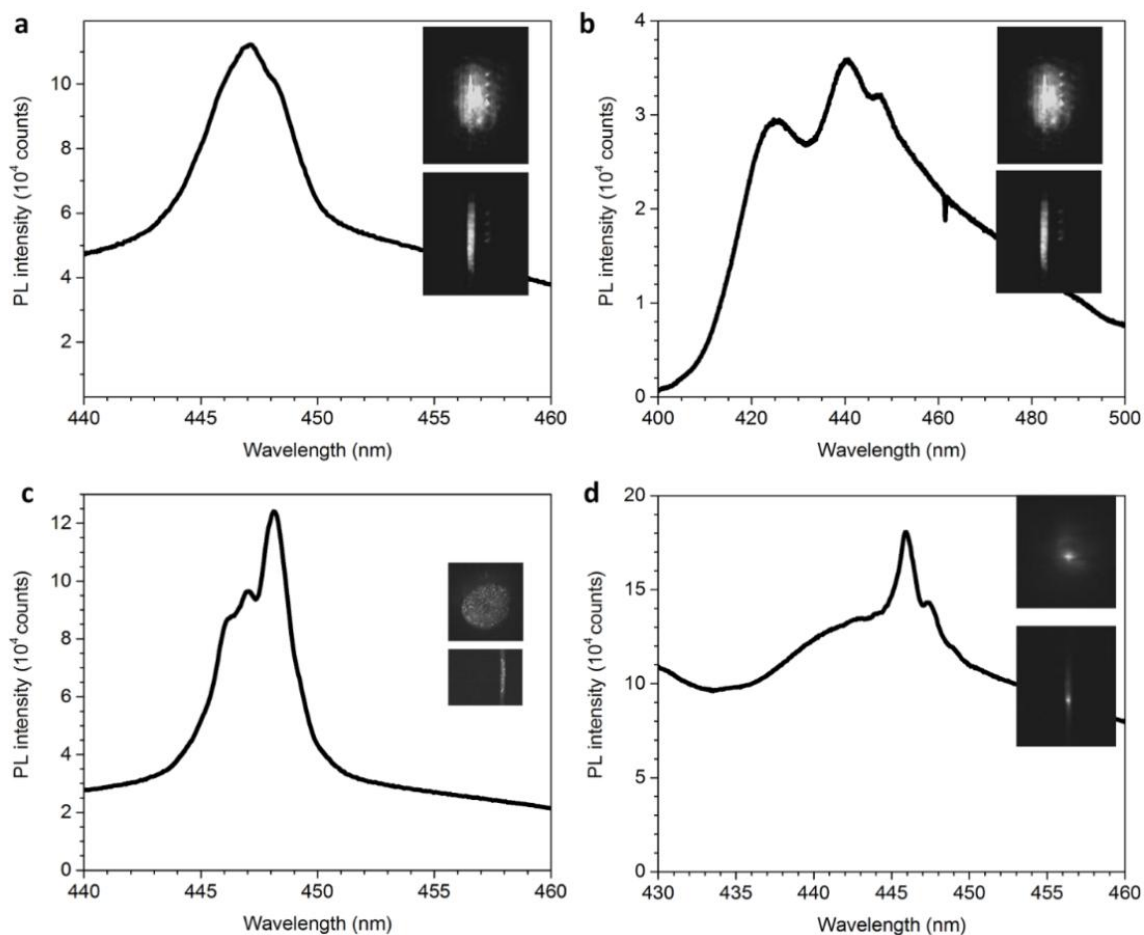


Figure A1.5. Emission spot dependence of PL spectra. (a) Defocused emission spot on imaging spectrometer, slit in the center of the emission spot, sample probed near the center. (b) Defocused emission spot on imaging spectrometer, slit in the center of the emission spot, sample probed near the edge. (c) Defocused emission spot on imaging spectrometer, slit in the edge of the emission spot, sample probed near the center. (d) Finely-focused emission spot on imaging spectrometer, slit in the center of the emission spot, sample probed near the center. Note that for all PL spectra, the actual laser excitation spot size and, correspondingly, the expected PL emission spot size at the sample was fixed at ~ 0.28 mm in diameter.

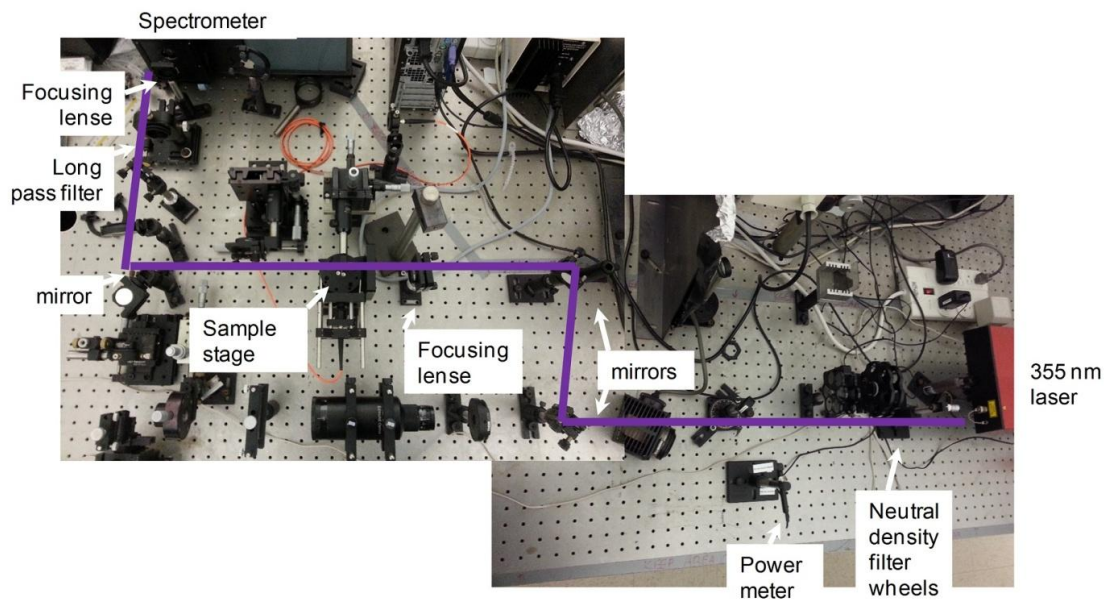


Figure A1.6. Diagram of PL spectroscopy setup.

A2 Appendix to Chapter 3

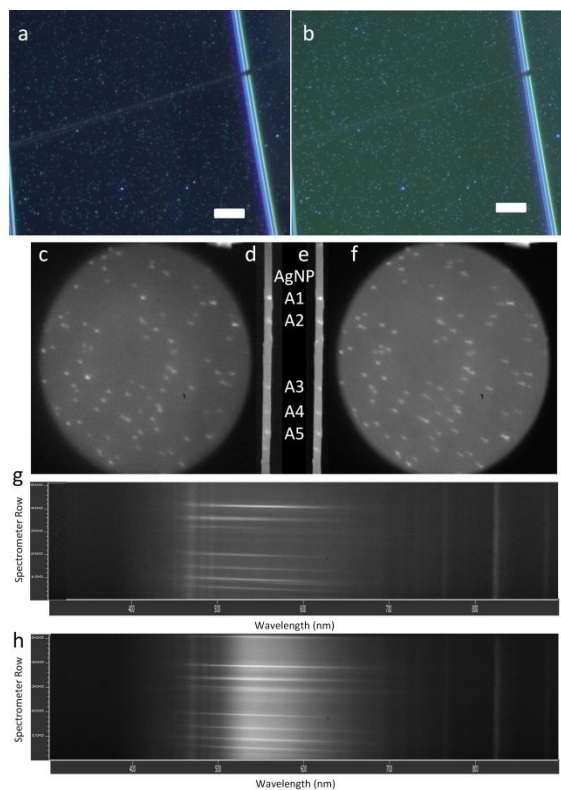


Figure A2.1. Images taken of region A of the AgNP sample before and after coating with an ultra-thin layer of F8BT. (a-b) DF microscope images of AgNPs before coating (a) and after coating (b) with F8BT. (c-f) Real-space spectrometer images of AgNPs before coating (c, d) and after coating (e, f) with F8BT. (d-e) are when the spectrometer slit was closed, in order to isolate individual AgNPs. The designations of the AgNP positions are indicated between images d and e. (g-h) Spectrometer image spectra obtained for the AgNPs before coating (g) and after coating (h) with F8BT.

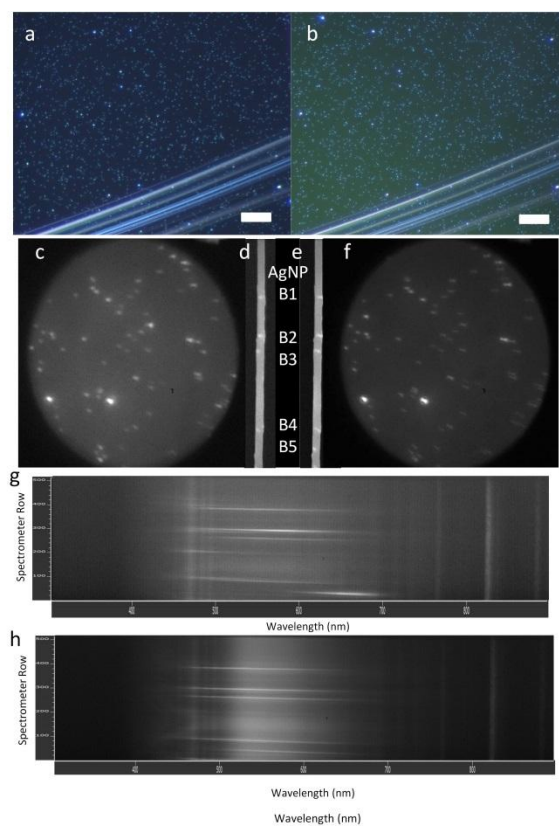


Figure A2.2. Images taken of region B of the AgNP sample before and after coating with an ultra-thin layer of F8BT. (a-b) DF microscope images of AgNPs before coating (a) and after coating (b) with F8BT. (c-f) Real-space spectrometer images of AgNPs before coating (c, d) and after coating (e, f) with F8BT. (d-e) are when the spectrometer slit was closed, in order to isolate individual AgNPs. The designations of the AgNP positions are indicated between images d and e. (g-h) Spectrometer image spectra obtained for the AgNPs before coating (g) and after coating (h) with F8BT.

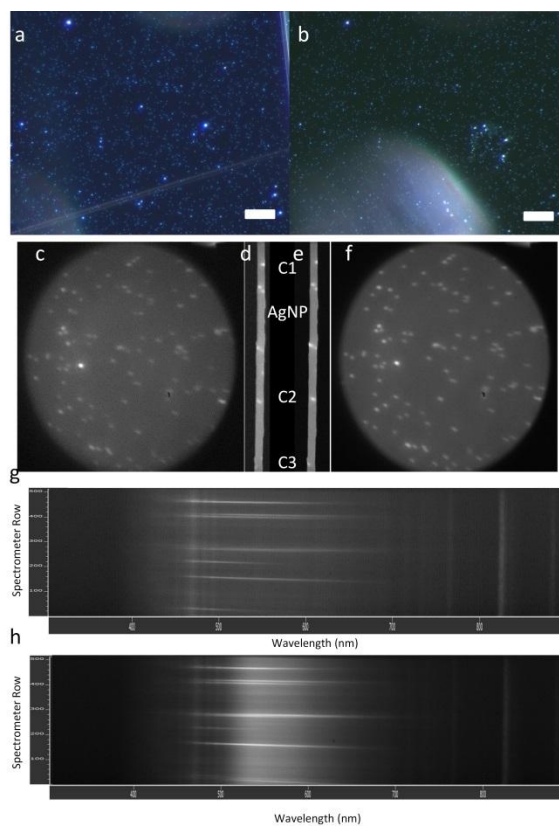


Figure A2.3. Images taken of region C of the AgNP sample before and after coating with an ultra-thin layer of F8BT. (a-b) DF microscope images of AgNPs before coating (a) and after coating (b) with F8BT. (c-f) Real-space spectrometer images of AgNPs before coating (c, d) and after coating (e, f) with F8BT. (d-e) are when the spectrometer slit was closed, in order to isolate individual AgNPs. The designations of the AgNP positions are indicated between images d and e. (g-h) Spectrometer image spectra obtained for the AgNPs before coating (g) and after coating (h) with F8BT.

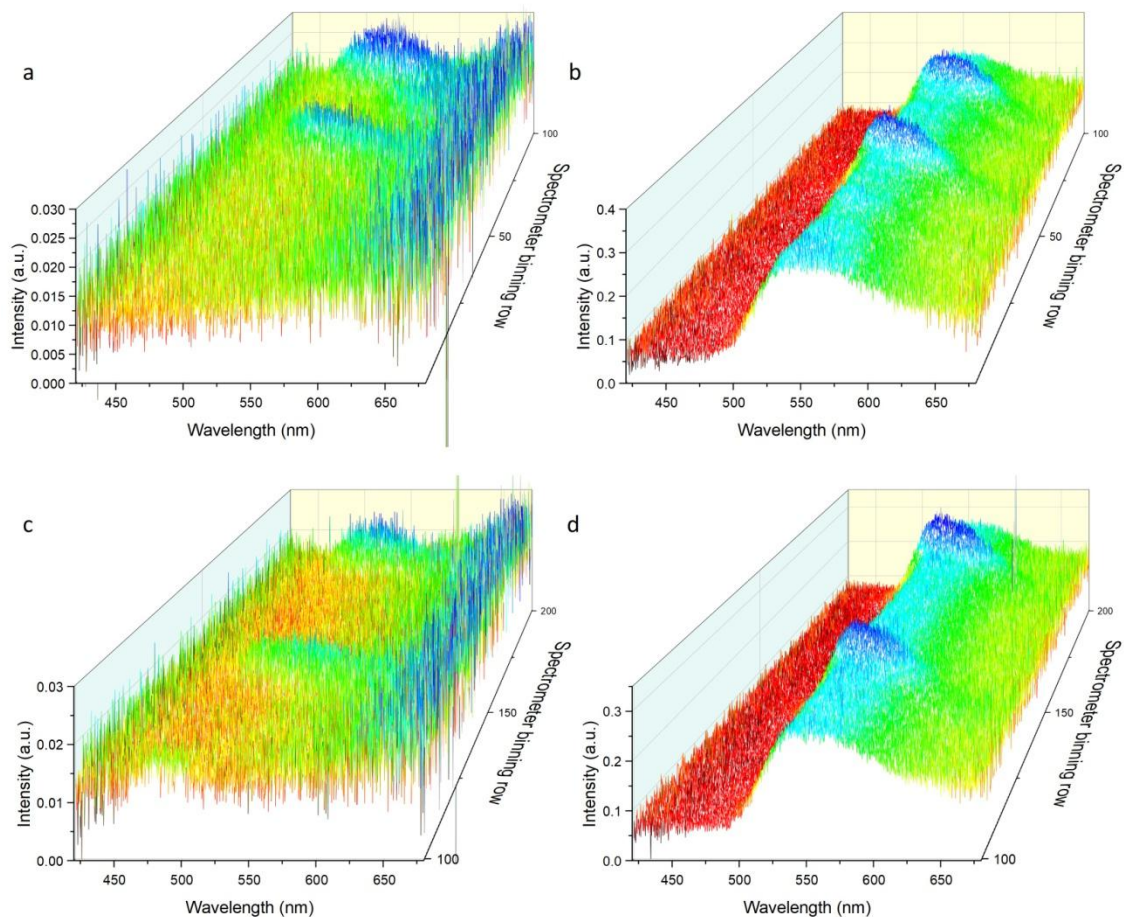


Figure A2.4. DF scattering spectra obtained from single AgNPs and single AgNPs coated with ultra-thin F8BT films corresponding to region A of the sample. (a) DF image spectra of the uncoated AgNPs. (b) DF image spectra of the F8BT coated AgNPs corresponding to particles from (a). (c) DF image spectra of the uncoated AgNPs. (d) DF image spectra of the F8BT coated AgNPs corresponding to particles from (c).

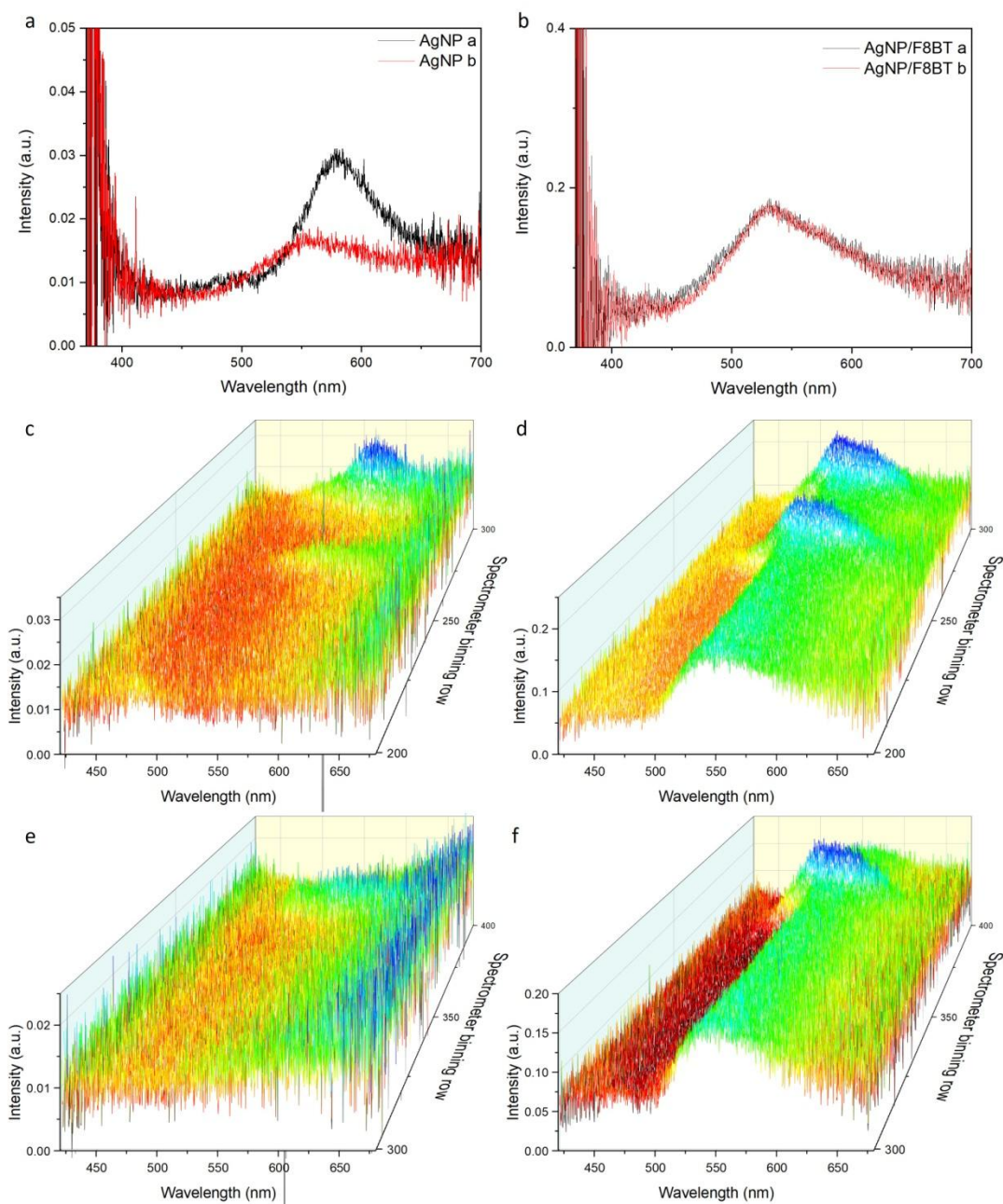


Figure A2.5. DF scattering spectra obtained from single AgNPs and single AgNPs coated with ultra-thin F8BT films corresponding to region B of the sample. (a) averaged DF scattering spectra of single AgNPs before coating. (b) Averaged DF scattering spectra of the same single AgNPs after coating with F8BT. (c) DF image spectra of the uncoated AgNPs. (d) DF image spectra of the F8BT coated AgNPs corresponding to particles from (c). (e) DF image spectra of the uncoated AgNPs (f) DF image spectra of the F8BT coated AgNPs corresponding to particles from (e).

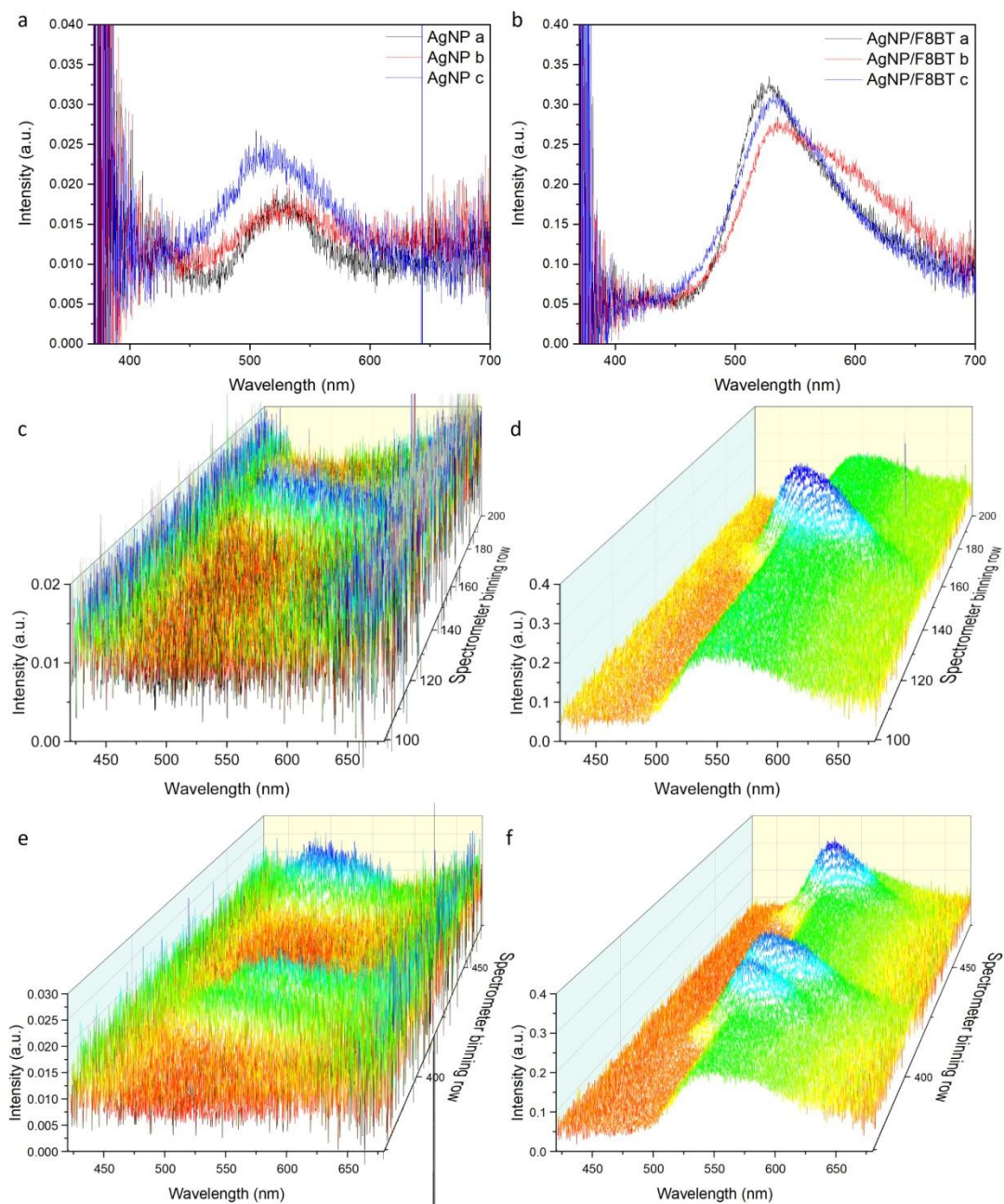


Figure A2.6. DF scattering spectra obtained from single AgNPs and single AgNPs coated with ultra-thin F8BT films corresponding to region C of the sample. (a) averaged DF scattering spectra of single AgNPs before coating. (b) Averaged DF scattering spectra of the same single AgNPs after coating with F8BT. (c) DF image spectra of the uncoated AgNPs. (d) DF image spectra of the F8BT coated AgNPs corresponding to particles from (c). (e) DF image spectra of the uncoated AgNPs (f) DF image spectra of the F8BT coated AgNPs corresponding to particles from (e).

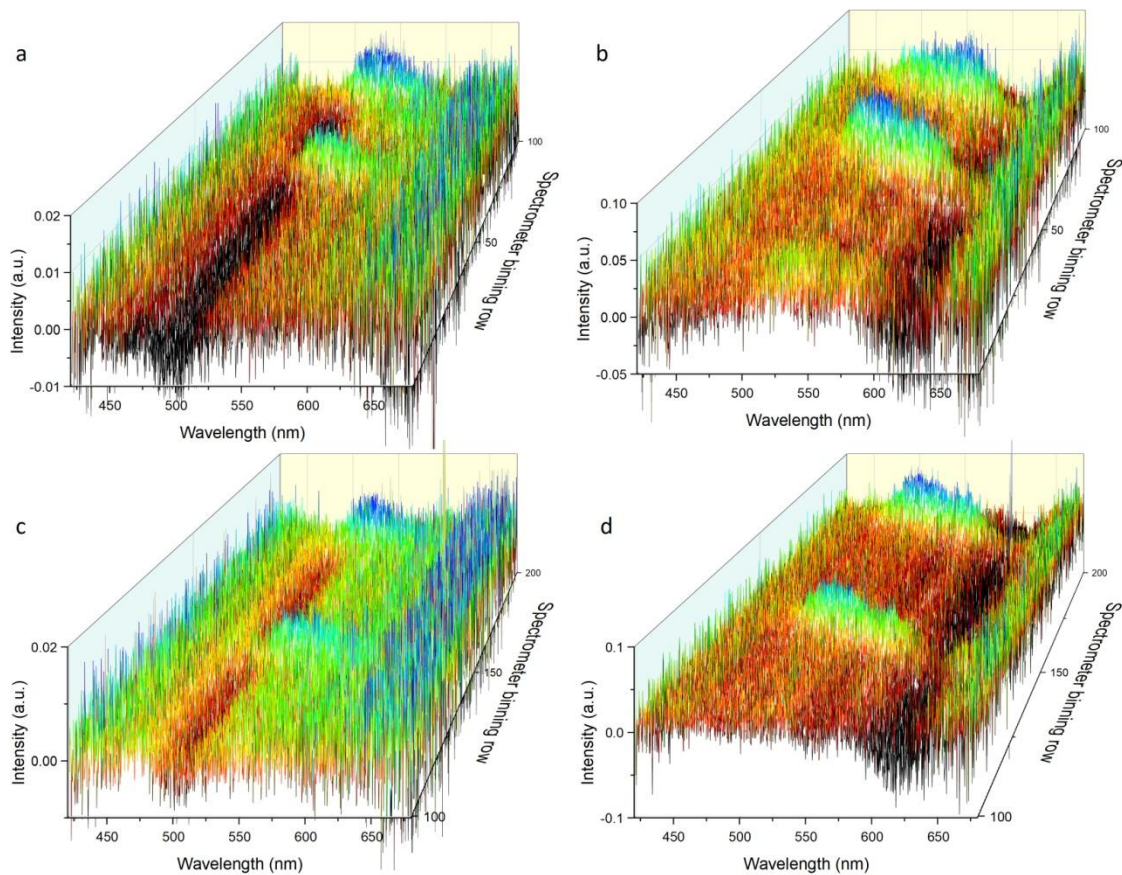


Figure A2.7. DF scattering spectra obtained from single AgNPs and single AgNPs coated with ultra-thin F8BT films corresponding to region A of the sample. (a, c) DF image spectra of the uncoated AgNPs, with the spectrum of a nearby area without a NP subtracted from all the spectra. (b, d) DF image spectra of the F8BT coated AgNPs, with the spectrum of a nearby area without a NP subtracted from all the spectra.

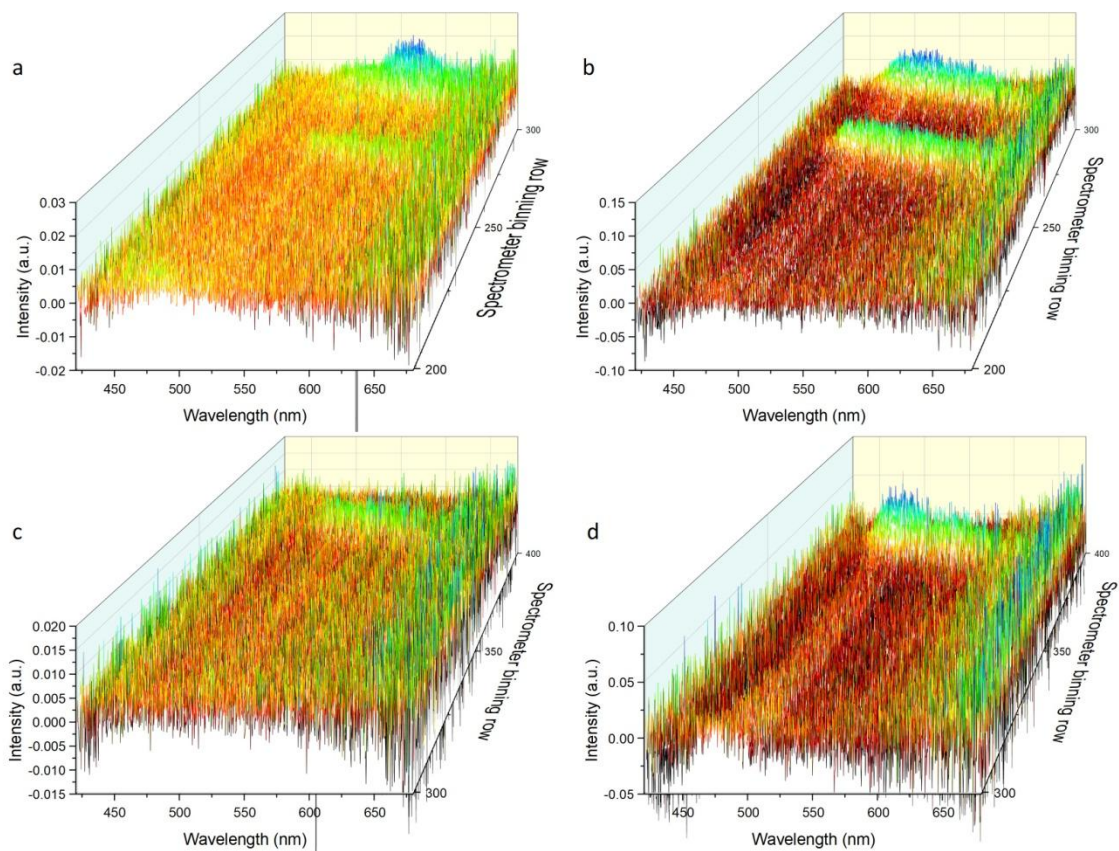


Figure A2.8. DF scattering spectra obtained from single AgNPs and single AgNPs coated with ultra-thin F8BT films corresponding to region B of the sample. (a, c) DF image spectra of the uncoated AgNPs, with the spectrum of a nearby area without a NP subtracted from all the spectra. (b, d) DF image spectra of the F8BT coated AgNPs, with the spectrum of a nearby area without a NP subtracted from all the spectra.

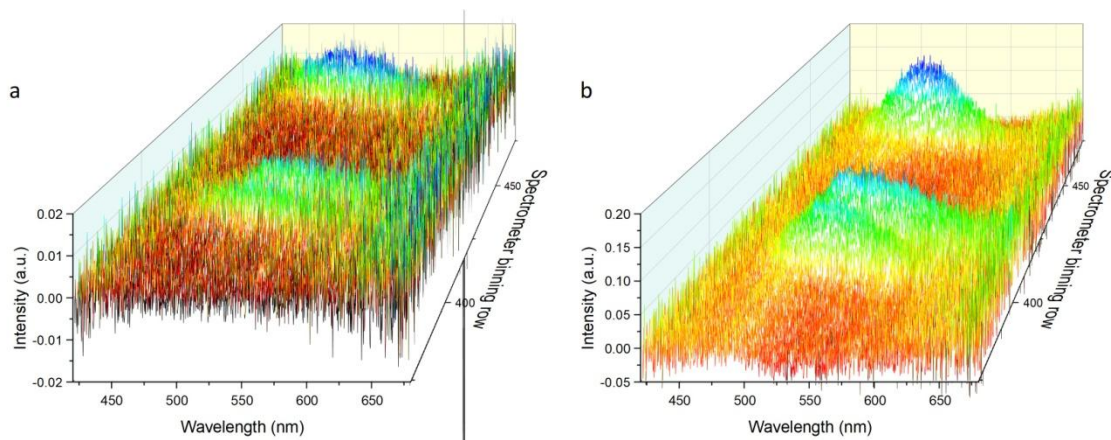


Figure A2.9. DF scattering spectra obtained from single AgNPs and single AgNPs coated with ultra-thin F8BT films corresponding to region C of the sample. (a) DF image spectra of the uncoated AgNPs, with the spectrum of a nearby area without a NP subtracted from all the spectra. (b) DF image spectra of the F8BT coated AgNPs, with the spectrum of a nearby area without a NP subtracted from all the spectra.

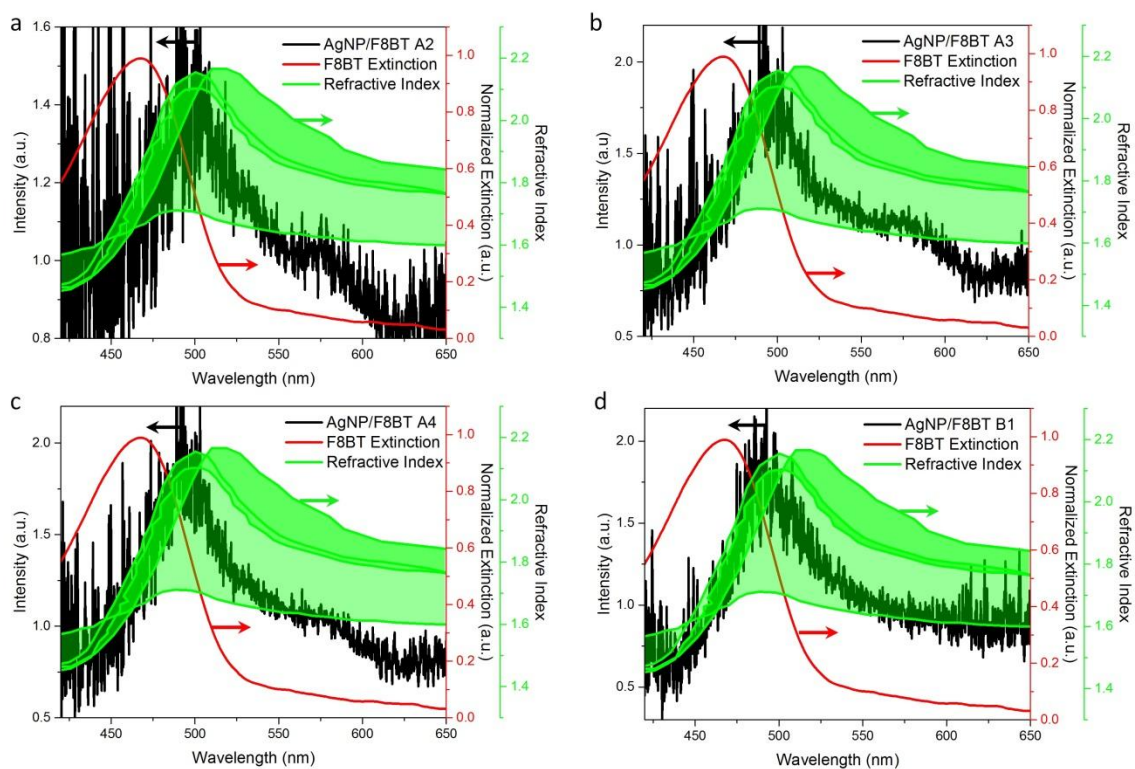


Figure A2.10. Averaged DF scattering spectra from F8BT coated AgNPs divided by the spectra of F8BT from a nearby region, compared to the F8BT extinction spectra (red line) and compared to the refractive index of F8BT (green line). (a-c) Spectra obtained from region A of the sample, AgNP number 2-4. (d) Spectra obtained from region B of the sample, AgNP number 1.

A3 Appendix to Chapter 4

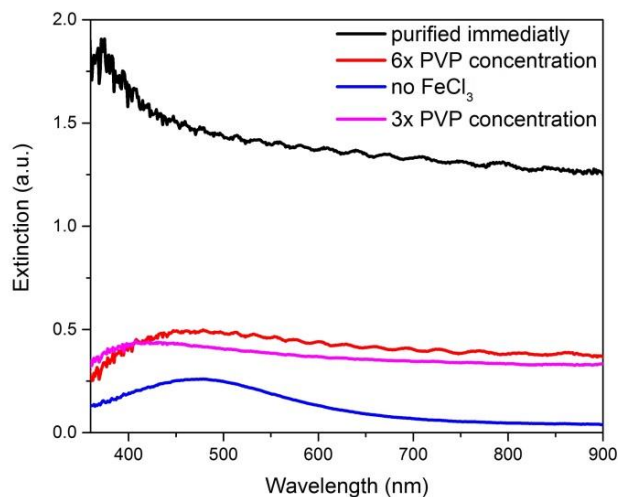


Figure A3.1. UV visible extinction spectra for the purified product shown in Figure 2a-d (in the main text). Black line is the sample purified immediately after the reagents were added, red line is the PVP weight percent increased by a factor of 6, blue line is the synthesis without an FeCl₃ source, and the pink line is the PVP weight percent increased by a factor of 3.

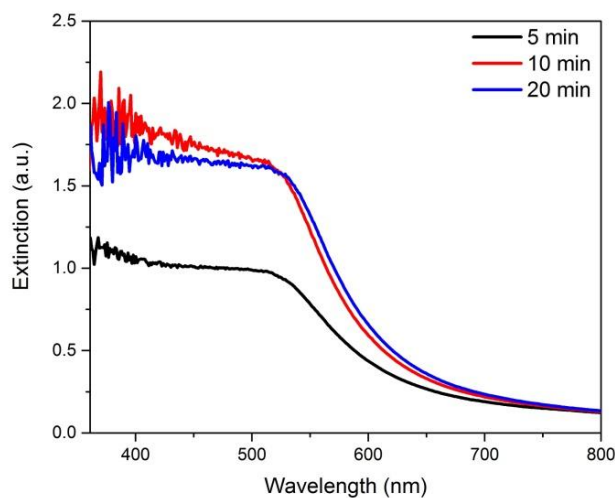


Figure A3.2. UV visible extinction spectra for the purified products shown in Figure 4a-c (in the main text). The black line is the sample after 5 min, the red line is the sample after 10 min, and the blue line is the sample after 20 min.

A3.1 90:10 EG:PEG 200 Ratio Procedure

The mixed EG:PEG 200 procedure closely follows the typical procedure described in the methods section, the main difference was the ratio of the solvent used.

First, an oil bath was preheated to 150 °C. Meanwhile, 5 mL of the EG, 0.5 mL of PEG200, 0.5 mL of a 6×10^{-4} M $\text{FeCl}_3 \cdot 6\text{H}_2\text{O}$ in EG, and a micro, Teflon-coated, 2 mm x 5 mm, micro stir bar were added to an Erlenmeyer flask. The flask was then placed in the preheated oil bath with stirring set to 1000 rpm, to ensure even heating in the flask. Then, the solution was heated for 30 min. Meanwhile, a stock solution of PVP (0.065 M) and AgNO_3 (0.096 M) combined together in a 90:10 mixture of the two solvents being used (EG and PEG 200) was prepared. After the 30 min of heating the flask, 6 mL of the AgNO_3 /PVP stock solution was added dropwise to the flask at a rate of ~ 0.3 mL/min, using a burette. After all 6 mL were added, the solution was heated and stirred for another 1.5 hours, after which the flask was removed from the oil bath, and the reaction product was purified by centrifugation as follows. Approximately 1 mL of the reaction product was removed from the Erlenmeyer flask, and placed in a 15 mL centrifuge tube and diluted with 4 mL of acetone and 4 mL of ethanol, shaken vigorously, then sonicated for about 20 s to disperse. The solution was then centrifuged (using a VWR clinical 50 centrifuge) at 1900 g's for 10 min. The supernatant was then removed and replaced with another 4 mL of acetone and 4 mL of ethanol, shaken and sonicated, and centrifuged again under the same conditions. The supernatant was removed once more, and 2 mL of ethanol was added as a final solvent, shaken and sonicated as before to disperse. Modifications of the aforementioned synthesis were made to assess the impact of variables on the shape/size of the silver nanoparticles.

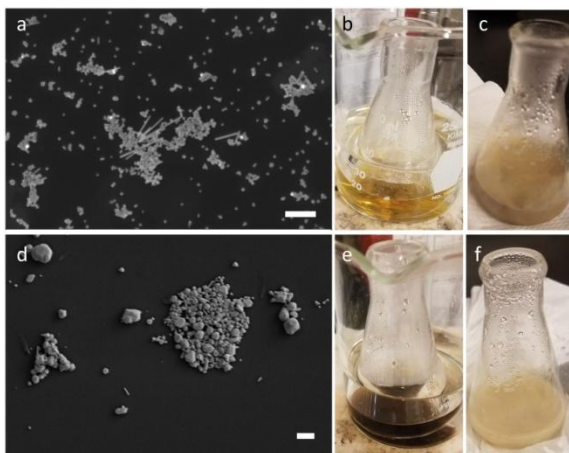


Figure A3.3. SEM and photographs of the reaction products for the EG control reaction as well as the 90:10 EG:PEG 200 reaction. (a, b, c) EG control reaction product; (d, e, f) 90:10 EG:PEG 200 reaction product; (b, e) early in the reaction, while heating. (c, f) reaction product after heating. Scale bars are 1 μm .

A4 Appendix to Chapter 5

A4.1 Life Cycle Assessment of Polyol and Sodium Borohydride Methods

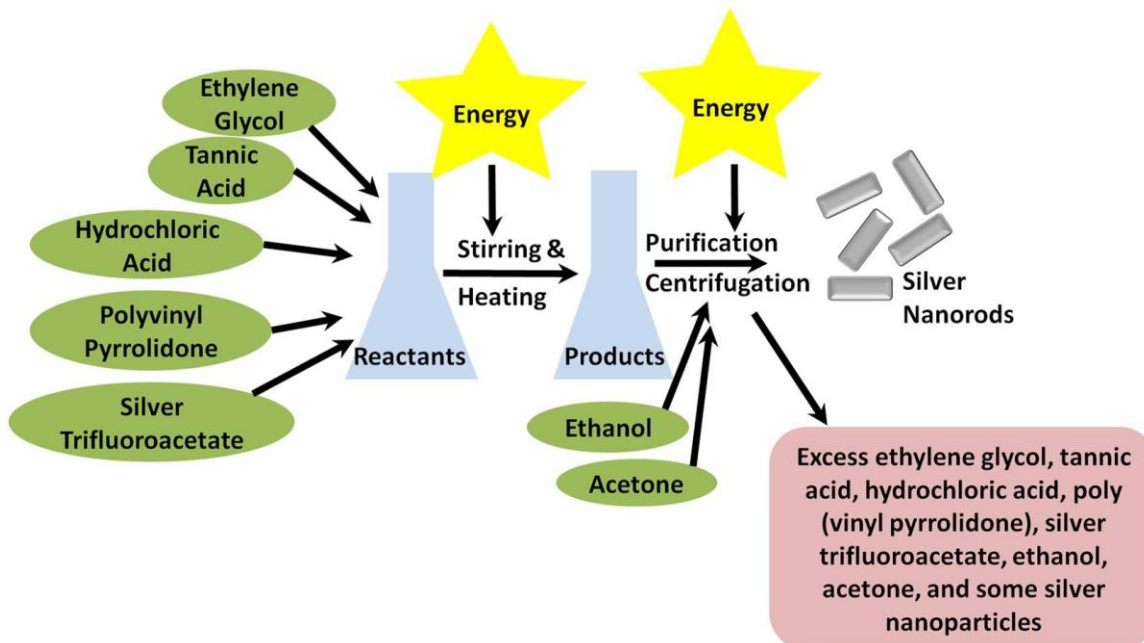


Figure A4.1.1 Schematic of the polyol process analyzed for a life cycle assessment. Green circles are reagents input into the reaction. Yellow stars are energy inputs. Pink box represents reagents produced/unused.

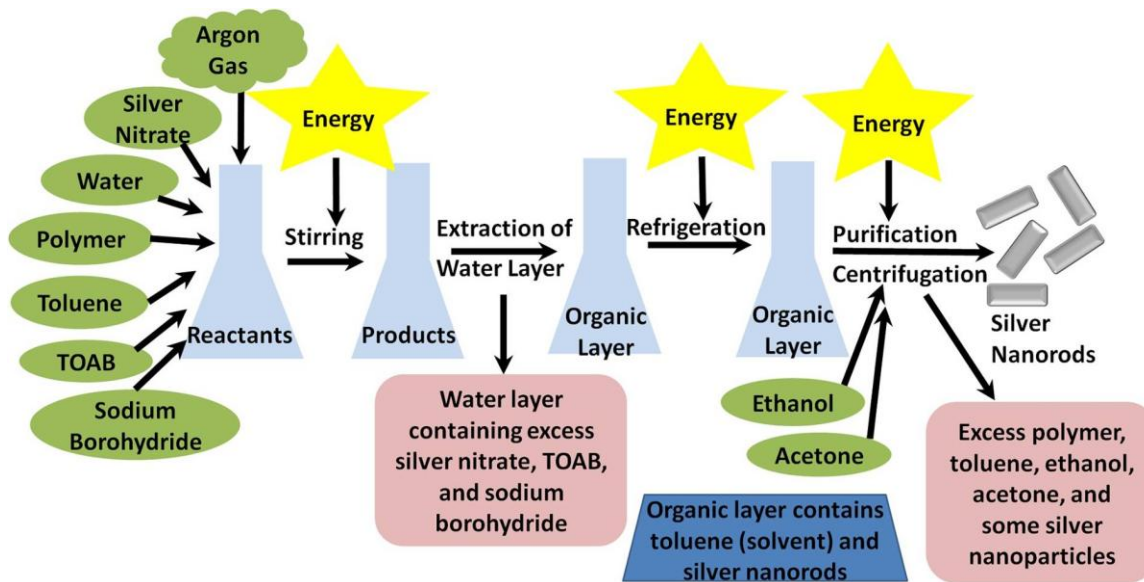


Figure A4.1.2. Schematic of the sodium borohydride process analyzed for a life cycle assessment. Green circles are reagents input into the reaction. Yellow stars are energy inputs. Pink box represents reagents produced/unused.

The life cycle assessment focusing of the production phase (from reagents to product) was performed comparing two published procedures, the polyol method reported by Pattarroyo *et al.* [110] and the sodium borohydride method reported by Fratoddi *et al.* [111]. These two procedures were chosen to compare because, although they use vastly different reagents and methods, they both claim to produce the same product – anisotropic silver nanorods. Table A4.1 shows the reagents used by each method. Figure A4.3 shows graphs that quantify the data from the preliminary life cycle assessment that was carried out. Solubility (Figure A4.3a) was chosen as the parameter to analyze the environmental impact of the methods since if the reagents or product are soluble in water, it could lead to pollution of waterways. The solubility values (grams per 100 mL) in 25 °C water were found using Material Safety Data Sheets. Next the amount of each reagent used in the synthesis was accounted for, and the minimum volume of water needed to dissolve was added up for all the reagents used in each synthesis method. Human health impacts (Figure A4.3b) were quantified by using standard NFPA diamond ratings for each reagent. Each of the four NFPA category scores were added for each chemical used, and then the total for all the chemicals were averaged. A cost comparison (Figure A4.3c) was performed by adding the monetary cost per gram of each reagent used. To determine the energy required (Figure A4.3d) for each method, calculations of the energy required to produce 1 gram of silver nanoparticles using each synthesis method was quantified by estimating the amount of electricity which was required for heating, stirring, etc. for each method.

The sodium borohydride method consistently had higher values for each metric used to quantify the life cycle assessment. For all metrics except solubility, a lower value

is a positive result. For solubility it is debatable what is the best result, since it depends on the disposal techniques implemented in the production facility. Based on this preliminary life cycle assessment the polyol method is indeed a greener method, at least for this phase of its life cycle. However a more complete assessment should be performed.

Table A4.1.1. Reagents and their role for each method analyzed.

<i>Reagent's Role</i>	<i>Polyol Method</i>	<i>Sodium Borohydride Method</i> [111] [110]
Solvent	ethylene glycol	water
Reducing Agent	ethylene glycol	sodium borohydride
Source of Silver	silver trifluoroacetate	silver nitrate
Capping Agent	poly(vinyl pyrrolidone)	polymer (lab synthesized)
Co-Reducing Agent	tannic acid	tetraoctylammonium bromide in toluene
Chloride Ion Source	hydrochloric acid	n/a
Other Chemicals	n/a	degassed with argon gas for 15 min.
Reaction Time	~2 hours	~ 13 hours
Reaction Temperature	150 °C	room temperature

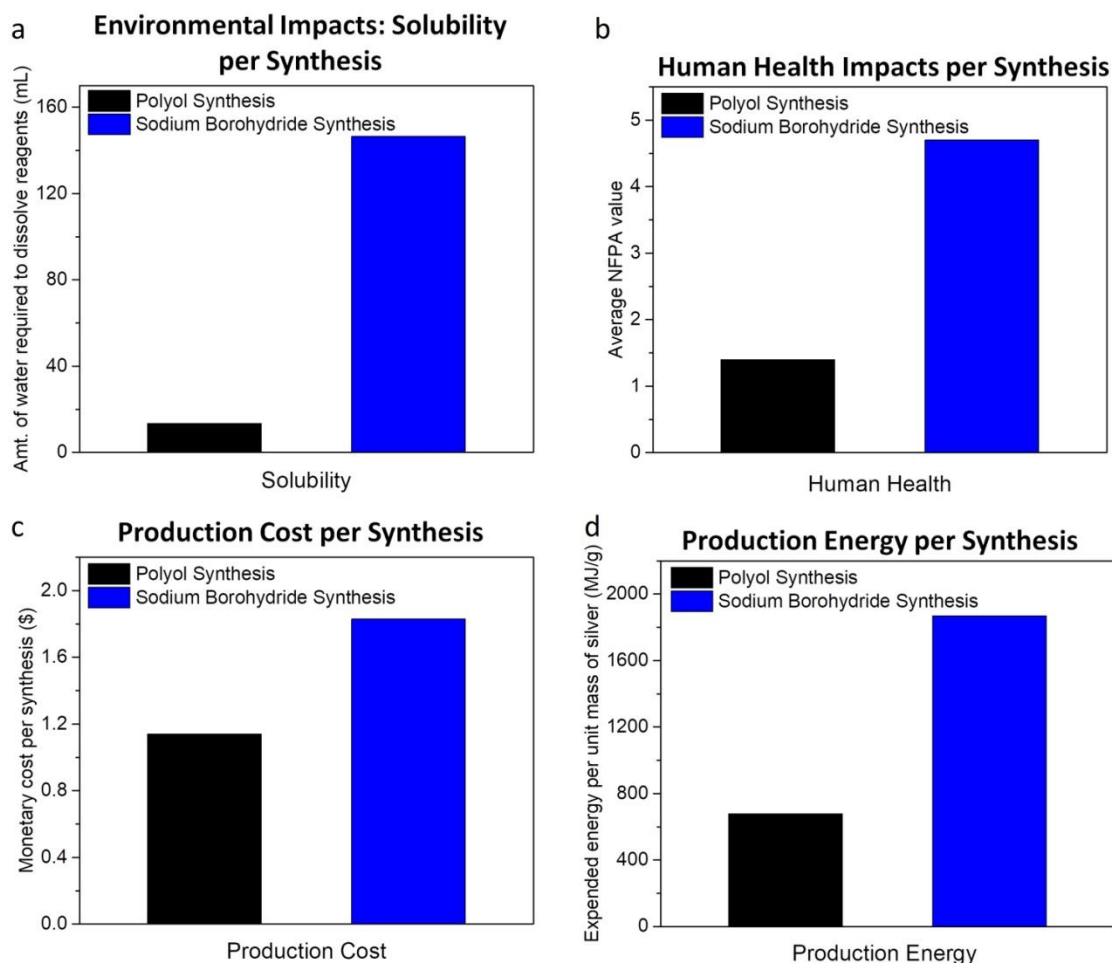


Figure A4.1.3. Graphs of the data from the preliminary life cycle assessment comparing polyol and sodium borohydride methods for silver nanoparticle synthesis. (a) Quantification of the environmental impact of the synthesis based on solubility of the synthesis reagents. (b) Quantification of human health impacts for each synthesis. (c) Quantification of the production cost of each synthesis. (d) Quantification of the energy required for each synthesis.

A4.2 Single Particle Spasers

Preliminary PL spectroscopic measurements were performed for AgNP/PFO samples. Figure A4.2.1a shows a schematic of the sample setup. It is similar to the sample fabrication demonstrated in Chapter 2, except the PAA layer was removed to obtain less dense AgNPs. Also the glass/optical adhesive cover was removed to make microscope imaging (and finding and isolating single AgNPs) easier. Figure A4.2.1b

shows the spectrometer image with slit closed. Clearly three AgNPs are isolated in this image. The power dependent PL spectra obtained from these three AgNPs is shown in Figure A4.2.1c. Stimulated emission is observed, however due to instrument issues the power readings for these measurements, and the complete range of laser powers were unable to be obtained. Again due to instrument issues, spectra from the PFO film control sample was unable to be obtained. These measurements should be repeated, to verify that this result is due to the AgNPs. Additionally measurements at the single NP level should be carried out, as opposed to these at the three NP level.

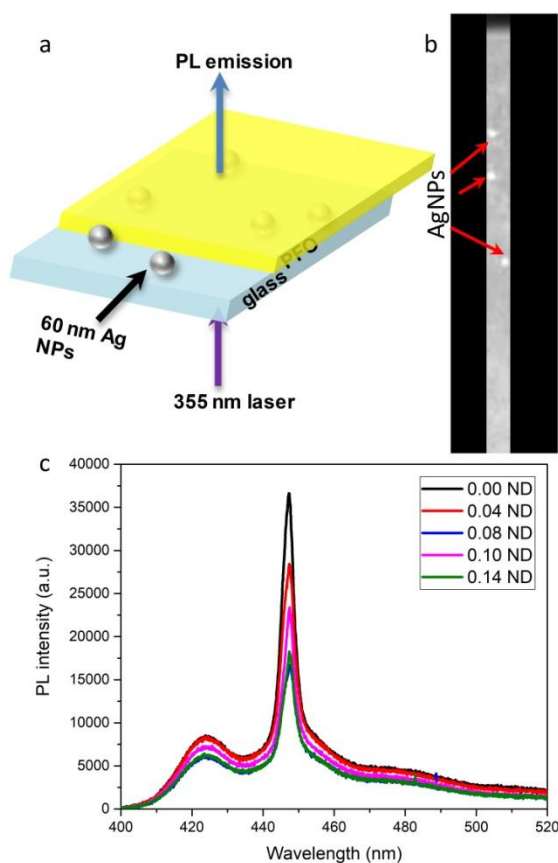


Figure A4.2.1. Schematic, spectrometer image, and PL spectra for few AgNP/PFO samples. (a) schematic of the AgNP/PFO films. (b) Spectrometer image, with the slit closed showing that three individual AgNPs were isolated. (c) PL spectra obtained from the three AgNPs for a range of neutral density filters, which effectively vary the power of the laser exciting the sample.

Bibliography

1. Lozano, G., et al., *Metallic nanostructures for efficient LED lighting*. Light: Science & Applications, 2016. **5**: p. e16080.
2. Okamoto, K., et al., *Plasmonics toward high-efficiency LEDs from the visible to the deep-UV region*. SPIE OPTO. Vol. 10124. 2017: SPIE.
3. Ferrari, L., et al., *Design and Analysis of Blue InGaN/GaN Plasmonic LED for High-Speed, High-Efficiency Optical Communications*. ACS Photonics, 2018. **5**(9): p. 3557-3564.
4. Ferry, V.E., et al., *Plasmonic Nanostructure Design for Efficient Light Coupling into Solar Cells*. Nano Letters, 2008. **8**(12): p. 4391-4397.
5. Ferry, V.E., et al., *Light trapping in ultrathin plasmonic solar cells*. Optics Express, 2010. **18**(S2): p. A237-A245.
6. Nakayama, K., K. Tanabe, and H.A. Atwater, *Plasmonic nanoparticle enhanced light absorption in GaAs solar cells*. Applied Physics Letters, 2008. **93**(12): p. 121904.
7. Antosiewicz, T.J., S.P. Apell, and T. Shegai, *Plasmon-Exciton Interactions in a Core-Shell Geometry: From Enhanced Absorption to Strong Coupling*. ACS Photonics, 2014. **1**(5): p. 454-463.
8. Zengin, G., et al., *Evaluating Conditions for Strong Coupling between Nanoparticle Plasmons and Organic Dyes Using Scattering and Absorption Spectroscopy*. The Journal of Physical Chemistry C, 2016. **120**(37): p. 20588-20596.
9. Rycenga, M., et al., *Controlling the synthesis and assembly of silver nanostructures for plasmonic applications*. Chem Rev, 2011. **111**(6): p. 3669-712.
10. Chikkaraddy, R., et al., *Single-molecule strong coupling at room temperature in plasmonic nanocavities*. Nature, 2016. **535**: p. 127.
11. Kang, E.S.H., et al., *Strong Plasmon-Exciton Coupling with Directional Absorption Features in Optically Thin Hybrid Nanohole Metasurfaces*. ACS Photonics, 2018. **5**(10): p. 4046-4055.
12. Noginov, M.A., et al., *Demonstration of a spaser-based nanolaser*. Nature, 2009. **460**(7259): p. 1110-2.
13. Meng, X., et al., *Wavelength-tunable spasing in the visible*. Nano Lett, 2013. **13**(9): p. 4106-12.
14. Galanzha, E., et al., *Spaser as a biological probe*. Vol. 8. 2017.
15. Stamplecoskie, K.G., M. Grenier, and J.C. Scaiano, *Self-assembled dipole nanolasers*. J Am Chem Soc, 2014. **136**(8): p. 2956-9.
16. Wu, C.Y., et al., *Plasmonic green nanolaser based on a metal-oxide-semiconductor structure*. Nano Lett, 2011. **11**(10): p. 4256-60.
17. Oulton, R.F., et al., *Plasmon lasers at deep subwavelength scale*. Nature, 2009. **461**(7264): p. 629-32.
18. Lu, Y.J., et al., *Plasmonic nanolaser using epitaxially grown silver film*. Science, 2012. **337**(6093): p. 450-3.
19. Zhang, Q., et al., *A room temperature low-threshold ultraviolet plasmonic nanolaser*. Nat Commun, 2014. **5**: p. 4953.
20. Zhou, H., et al., *Ordered, uniform-sized ZnO nanolaser arrays*. Applied Physics Letters, 2007. **91**(18): p. 181112.
21. Suh, J.Y., et al., *Plasmonic Bowtie Nanolaser Arrays*. Nano Letters, 2012. **12**(11): p. 5769-5774.

22. Popov, O., A. Zilbershtein, and D. Davidov, *Random lasing from dye-gold nanoparticles in polymer films: Enhanced gain at the surface-plasmon-resonance wavelength*. Applied Physics Letters, 2006. **89**(19): p. 191116.
23. Dominguez, C.T., et al., *Dependence of random laser emission on silver nanoparticle density in PMMA films containing rhodamine 6G*. Journal of the Optical Society of America B, 2011. **28**(5): p. 1118-1123.
24. Noginov, M.A., et al., *Enhancement of surface plasmons in an Ag aggregate by optical gain in a dielectric medium*. Opt Lett, 2006. **31**(20): p. 3022-4.
25. Zhai, T., et al., *Red-green-blue plasmonic random laser*. Opt Express, 2017. **25**(3): p. 2100-2106.
26. Zhai, T., et al., *Ultra-thin plasmonic random lasers*. Opt Express, 2016. **24**(1): p. 437-42.
27. Heydari, E., et al., *Nanoplasmonically-engineered random lasing in organic semiconductor thin films*. Nanoscale Horizons, 2017. **2**(5): p. 261-266.
28. Meng, X., et al., *Random lasers with coherent feedback from highly transparent polymer films embedded with silver nanoparticles*. Applied Physics Letters, 2008. **92**(20): p. 201112.
29. Yadav, A., et al., *Tunable random lasing behavior in plasmonic nanostructures*. Nano Converg, 2017. **4**(1): p. 1.
30. Kitur, J., et al., *Dependence of the random laser behavior on the concentrations of dye and scatterers*. Journal of Optics, 2010. **12**(2): p. 024009.
31. Lawandy, N.M., *Localized surface plasmon singularities in amplifying media*. Applied Physics Letters, 2004. **85**(21): p. 5040-5042.
32. Arnold, N., C. Hrelescu, and T.A. Klar, *Minimal spaser threshold within electrodynamic framework: Shape, size and modes*. Ann Phys, 2016. **528**(3-4): p. 295-306.
33. Ma, R.-M., et al., *Plasmon lasers: coherent light source at molecular scales*. Laser & Photonics Reviews, 2013. **7**(1): p. 1-21.
34. Grandidier, J., et al., *Gain-assisted propagation in a plasmonic waveguide at telecom wavelength*. Nano Lett, 2009. **9**(8): p. 2935-9.
35. Nezhad, M.P., K. Tetz, and Y. Fainman, *Gain assisted propagation of surface plasmon polaritons on planar metallic waveguides*. Optics Express, 2004. **12**(17): p. 4072-4079.
36. Virgili, T., et al., *An ultrafast spectroscopy study of stimulated emission in poly(9,9-dioctylfluorene) films and microcavities*. Applied Physics Letters, 1999. **74**(19): p. 2767-2769.
37. Albrecht, G., et al., *Comprehensive Study of Plasmonic Materials in the Visible and Near-Infrared: Linear, Refractory, and Nonlinear Optical Properties*. ACS Photonics, 2018. **5**(3): p. 1058-1067.
38. Murray, W.A. and W.L. Barnes, *Plasmonic Materials*. Advanced Materials, 2007. **19**(22): p. 3771-3782.
39. O'Carroll, D.M., et al., *Metal-Polymer-Metal Split-Dipole Nanoantennas*. Advanced Materials, 2012. **24**(23): p. OP136-OP142.
40. O'Carroll, D.M., C.E. Hofmann, and H.A. Atwater, *Conjugated Polymer/Metal Nanowire Heterostructure Plasmonic Antennas*. Advanced Materials, 2010. **22**(11): p. 1223-1227.
41. Bergman, D.J. and M.I. Stockman, *Surface plasmon amplification by stimulated emission of radiation: quantum generation of coherent surface plasmons in nanosystems*. Phys Rev Lett, 2003. **90**(2): p. 027402.
42. Stockman, M.I., *Spasers explained*. Nature Photonics, 2008. **2**: p. 327.
43. Jayasekara, C., et al., *MoS2 spaser*. Journal of Applied Physics, 2016. **119**(13): p. 133101.

44. Sherry, L.J., et al., *Localized surface plasmon resonance spectroscopy of single silver nanocubes*. *Nano Lett*, 2005. **5**(10): p. 2034-8.
45. van der Zande, B.M.I., et al., *Colloidal Dispersions of Gold Rods: Synthesis and Optical Properties*. *Langmuir*, 2000. **16**(2): p. 451-458.
46. McGehee, M.D. and A.J. Heeger, *Semiconducting (Conjugated) Polymers as Materials for Solid-State Lasers*. *Advanced Materials*, 2000. **12**(22): p. 1655-1668.
47. Rivaton, A., et al., *Photostability of organic materials used in polymer solar cells*. *Polymer International*, 2014. **63**(8): p. 1335-1345.
48. Kang, Y. and T.A. Taton, *Core/Shell gold nanoparticles by self-assembly and crosslinking of micellar, block-copolymer shells*. *Angew Chem Int Ed Engl*, 2005. **44**(3): p. 409-12.
49. E, X.-T.-F., et al., *Shape evolution in Brust-Schiffrin synthesis of Au nanoparticles*. Vol. 118. 2014. 196-199.
50. Lai, C.H., et al., *Homogeneous, surfactant-free gold nanoparticles encapsulated by polythiophene analogues*. *Chem Commun (Camb)*, 2009(15): p. 1996-8.
51. Sun, Y. and Y. Xia, *Gold and silver nanoparticles: a class of chromophores with colors tunable in the range from 400 to 750 nm*. *Analyst*, 2003. **128**(6): p. 686-91.
52. Petoukhoff, C.E. and D.M. O'Carroll, *Absorption-induced scattering and surface plasmon out-coupling from absorber-coated plasmonic metasurfaces*. *Nature Communications*, 2015. **6**: p. 7899.
53. Gu, P., D.J.S. Birch, and Y. Chen, *Dye-doped polystyrene-coated gold nanorods: towards wavelength tuneable SPASER*. *Methods Appl Fluoresc*, 2014. **2**(2): p. 024004.
54. Oulton, R.F., et al., *A hybrid plasmonic waveguide for subwavelength confinement and long-range propagation*. *Nature Photonics*, 2008. **2**: p. 496.
55. Garcia-Vidal, F.J. and E. Moreno, *Applied physics: Lasers go nano*. *Nature*, 2009. **461**(7264): p. 604-5.
56. Hill, M.T., *Nanophotonics: lasers go beyond diffraction limit*. *Nat Nanotechnol*, 2009. **4**(11): p. 706-7.
57. Wang, C., et al., *Probing the seeded protocol for high-concentration preparation of silver nanowires*. *Nano Research*, 2016. **9**(5): p. 1532-1542.
58. Sánchez-Cortés, S., et al., *Morphological Study of Silver Colloids Employed in Surface-Enhanced Raman Spectroscopy: Activation when Exciting in Visible and Near-Infrared Regions*. *Journal of Colloid and Interface Science*, 1995. **175**(2): p. 358-368.
59. Nickel, U., et al., *A Silver Colloid Produced by Reduction with Hydrazine as Support for Highly Sensitive Surface-Enhanced Raman Spectroscopy*. *Langmuir*, 2000. **16**(23): p. 9087-9091.
60. Munro, C.H., et al., *Characterization of the Surface of a Citrate-Reduced Colloid Optimized for Use as a Substrate for Surface-Enhanced Resonance Raman Scattering*. *Langmuir*, 1995. **11**(10): p. 3712-3720.
61. Jana, N.R., L. Gearheart, and C.J. Murphy, *Wet chemical synthesis of silver nanorods and nanowires of controllable aspect ratio*. *Chemical Communications*, 2001(7): p. 617-618.
62. Zhang, J., M.R. Langille, and C.A. Mirkin, *Synthesis of silver nanorods by low energy excitation of spherical plasmonic seeds*. *Nano Lett*, 2011. **11**(6): p. 2495-8.
63. Zhang, Q., et al., *Seed-mediated synthesis of Ag nanocubes with controllable edge lengths in the range of 30-200 nm and comparison of their optical properties*. *J Am Chem Soc*, 2010. **132**(32): p. 11372-8.
64. Zhang, Q., et al., *Synthesis of Ag nanobars in the presence of single-crystal seeds and a bromide compound, and their surface-enhanced Raman scattering (SERS) properties*. *Langmuir*, 2012. **28**(24): p. 9047-54.

65. Aslan, K., et al., *Fast and slow deposition of silver nanorods on planar surfaces: application to metal-enhanced fluorescence*. J Phys Chem B, 2005. **109**(8): p. 3157-62.
66. Huang, T. and X.H. Nancy Xu, *Synthesis and Characterization of Tunable Rainbow Colored Colloidal Silver Nanoparticles Using Single-Nanoparticle Plasmonic Microscopy and Spectroscopy*. J Mater Chem, 2010. **20**(44): p. 9867-9876.
67. Tang, B., et al., *Shape evolution of silver nanoplates through heating and photoinduction*. ACS Appl Mater Interfaces, 2013. **5**(3): p. 646-53.
68. Van Hyning, D.L., W.G. Klemperer, and C.F. Zukoski, *Silver Nanoparticle Formation: Predictions and Verification of the Aggregative Growth Model*. Langmuir, 2001. **17**(11): p. 3128-3135.
69. Mulfinger, L., et al., *Synthesis and Study of Silver Nanoparticles*. Journal of Chemical Education, 2007. **84**(2): p. 322.
70. Nadagouda, M.N., T.F. Speth, and R.S. Varma, *Microwave-assisted green synthesis of silver nanostructures*. Acc Chem Res, 2011. **44**(7): p. 469-78.
71. Patel, K., et al., *Synthesis of nanosized silver colloids by microwave dielectric heating*. Journal of Chemical Sciences, 2005. **117**(1): p. 53-60.
72. Yu, D., et al., *Gamma-radiation synthesis, characterization and nonlinear optical properties of highly stable colloidal silver nanoparticles in suspensions*. Vol. 23. 2004. 50-55.
73. Liang, H., et al., *High-yield uniform synthesis and microstructure-determination of rice-shaped silver nanocrystals*. J Am Chem Soc, 2009. **131**(17): p. 6068-9.
74. Wiley, B.J., et al., *Synthesis and optical properties of silver nanobars and nanorice*. Nano Lett, 2007. **7**(4): p. 1032-6.
75. Wiley, B., Y. Sun, and Y. Xia, *Synthesis of silver nanostructures with controlled shapes and properties*. Acc Chem Res, 2007. **40**(10): p. 1067-76.
76. Kim, D., S. Jeong, and J. Moon, *Synthesis of silver nanoparticles using the polyol process and the influence of precursor injection*. Nanotechnology, 2006. **17**(16): p. 4019-24.
77. Liang, H., et al., *Silver Nanorice Structures: Oriented Attachment-Dominated Growth, High Environmental Sensitivity, and Real-Space Visualization of Multipolar Resonances*. Vol. 24. 2012. 2339-2346.
78. Sun, Y., et al., *Uniform Silver Nanowires Synthesis by Reducing AgNO₃ with Ethylene Glycol in the Presence of Seeds and Poly(Vinyl Pyrrolidone)*. Chemistry of Materials, 2002. **14**(11): p. 4736-4745.
79. Jiu, J., et al., *Preparation of Ag nanorods with high yield by polyol process*. Vol. 114. 2009. 333-338.
80. Chen, C., et al., *Study on the growth mechanism of silver nanorods in the nanowire-seeding polyol process*. Vol. 107. 2008. 13-17.
81. Gao, Y., et al., *Growth mechanism of silver nanowires synthesized by polyvinylpyrrolidone-assisted polyol reduction*. Journal of Physics D: Applied Physics, 2005. **38**(7): p. 1061-1067.
82. Nadagouda, M.N. and R.S. Varma, *Microwave-Assisted Shape-Controlled Bulk Synthesis of Ag and Fe Nanorods in Poly(ethylene glycol) Solutions*. Crystal Growth & Design, 2008. **8**(1): p. 291-295.
83. Popa, M., et al., *Stable silver colloidal dispersion using short chain polyethylene glycol*. Vol. 303. 2007. 184-190.
84. Coskun, S., B. Aksoy, and H.E. Unalan, *Polyol Synthesis of Silver Nanowires: An Extensive Parametric Study*. Crystal Growth & Design, 2011. **11**(11): p. 4963-4969.

85. Pourzahedi, L. and M.J. Eckelman, *Comparative life cycle assessment of silver nanoparticle synthesis routes*. Environmental Science: Nano, 2015. **2**(4): p. 361-369.
86. Cinelli, M., et al., *A green chemistry-based classification model for the synthesis of silver nanoparticles*. Green Chemistry, 2015. **17**(5): p. 2825-2839.
87. Zhang, L., et al., *Ultra-strong surface plasmon amplification characteristic of a spaser based on gold-silver core-shell nanorods*. Optics Communications, 2015. **338**: p. 313-321.
88. Wiersma, D.S., *Optics: light reined in*. Nature, 2008. **452**(7190): p. 942-4.
89. Su, K.H., et al., *Interparticle Coupling Effects on Plasmon Resonances of Nanogold Particles*. Nano Letters, 2003. **3**(8): p. 1087-1090.
90. Takahashi, H. and H. Naito, *Influence of nanometer-size interface roughness on light transmission in polyfluorene waveguides studied by amplified spontaneous emission measurements*. Current Applied Physics, 2006. **6**(5): p. 882-886.
91. Frolov, S.V., et al., *Stimulated emission in high-gain organic media*. Physical Review B, 1999. **59**(8): p. R5284-R5287.
92. Yu, S.F., et al., *Random laser action in ZnO nanorod arrays embedded in ZnO epilayers*. Applied Physics Letters, 2004. **84**(17): p. 3241-3243.
93. Wang, Z., et al., *Nanolasers Enabled by Metallic Nanoparticles: From Spasers to Random Lasers*. Laser & Photonics Reviews, 2017. **11**(6): p. 1700212.
94. Choi, H., et al., *Versatile surface plasmon resonance of carbon-dot-supported silver nanoparticles in polymer optoelectronic devices*. Nature Photonics, 2013. **7**: p. 732.
95. Luk'yanchuk, B., et al., *The Fano resonance in plasmonic nanostructures and metamaterials*. Nat Mater, 2010. **9**(9): p. 707-15.
96. Stockton, W.B. and M.F. Rubner, *Molecular-Level Processing of Conjugated Polymers. 4. Layer-by-Layer Manipulation of Polyaniline via Hydrogen-Bonding Interactions*. Macromolecules, 1997. **30**(9): p. 2717-2725.
97. Campoy-Quiles, M., et al., *Ellipsometric Characterization of the Optical Constants of Polyfluorene Gain Media*. Advanced Functional Materials, 2005. **15**(6): p. 925-933.
98. Ramsdale, C.M. and N.C. Greenham, *The optical constants of emitter and electrode materials in polymer light-emitting diodes*. Journal of Physics D: Applied Physics, 2003. **36**(4): p. L29-L34.
99. Winfield, J.M., C.L. Donley, and J.-S. Kim, *Anisotropic optical constants of electroluminescent conjugated polymer thin films determined by variable-angle spectroscopic ellipsometry*. Journal of Applied Physics, 2007. **102**(6): p. 063505.
100. Shen, Z., K. Zhu, and D.M. O'Carroll, *Aperiodic Porous Metasurface-Mediated Organic Semiconductor Fluorescence*. ACS Photonics, 2018. **5**(4): p. 1215-1227.
101. Park, K.H., S.H. Im, and O.O. Park, *The size control of silver nanocrystals with different polyols and its application to low-reflection coating materials*. Nanotechnology, 2011. **22**(4): p. 045602.
102. Luo, C., et al., *The role of poly(ethylene glycol) in the formation of silver nanoparticles*. J Colloid Interface Sci, 2005. **288**(2): p. 444-8.
103. Skrabalak, S.E., et al., *On the polyol synthesis of silver nanostructures: glycolaldehyde as a reducing agent*. Nano Lett, 2008. **8**(7): p. 2077-81.
104. Abdel-Motaleb, M.E.K., M. F.; Taher, M. A.; Gahlan, A. A.; Hamed, A. M., *Influence of Nanosilver Synthesis Conditions on it Architecture*. Proceedings of Basic and Applied Sciences, 2013. **1**(1): p. 402-408.
105. Dong, B., et al., *Local surface plasmon resonance of single silver nanorice particles in the near-infrared*. Vol. 181. 2014. 791-795.

106. Paramelle, D., et al., *A rapid method to estimate the concentration of citrate capped silver nanoparticles from UV-visible light spectra*. *Analyst*, 2014. **139**(19): p. 4855-4861.
107. Tsuji, M., et al., *Effects of chain length of polyvinylpyrrolidone for the synthesis of silver nanostructures by a microwave-polyol method*. *Materials Letters*, 2006. **60**(6): p. 834-838.
108. Redding, B., M.A. Choma, and H. Cao, *Spatial coherence of random laser emission*. *Optics Letters*, 2011. **36**(17): p. 3404-3406.
109. Huang, C.-H., Y.-H. Wen, and Y.-W. Liu, *Measuring the second order correlation function and the coherence time using random phase modulation*. *Optics Express*, 2016. **24**(4): p. 4278-4288.
110. Patarroyo, J., et al., *One-pot polyol synthesis of highly monodisperse short green silver nanorods*. *Chem Commun (Camb)*, 2016. **52**(73): p. 10960-3.
111. Fratoddi, I., et al., *Core shell hybrids based on noble metal nanoparticles and conjugated polymers: synthesis and characterization*. *Nanoscale research letters*, 2011. **6**(1): p. 98-98.